Università degli Studi di Napoli Federico II

Dottorato di Ricerca in
Ingegneria Strutturale, Geotecnica e Rischio Sismico

THESIS FOR THE DEGREE OF DOCTOR OF PHILOSOPHY

Earthquake and tsunami multi-hazard risk analysis of a petrochemical plant

by
ANTONIO VITALE

Advisor: Prof. Iunio Iervolino

Co-advisors: Dr. Georgios Baltzopoulos
Dr. Pasquale Cito

SCUOLA POLITECNICA E DELLE SCIENZE DI BASE
DIPARTIMENTO D STRUTTURE PER L'INGEGNERIA E L'ARCHITETTURA

Napoli marzo ’24

Mancano pochi minuti al click di un bottone, che in qualche modo mette un punto ad un percorso durato ben quattro lunghi anni e penso: “Ma come ho fatto ad arrivare fino alla fine?”. Caparbietà, costanza, coraggio, oppure è stata solo totale incoscienza.

Volevo vivere un’esperienza unica, e così è stato. Mi sono goduto ogni momento, ho sfruttato a pieno qualunque occasione si presentasse. Ho voluto lavorare e confrontarmi con chiunque per apprendere il sapere da ognuno. Sono stato circondato da professori, professionisti, colleghi che mi ha continuamente riempito di stimoli e di sfide. Per questo è doveroso ringraziare.

Inizio con il mio mentore, il Professore Iunio Iervolino. Uomo sempre onesto e sincero. Ha saputo ascoltarmi, ha saputo assecondarmi, ha saputo darmi fiducia. La sua passione per la ricerca e la didattica è stata contagiosa.

Ringrazio il mio maestro, il Dr. Georgios Baltzopoulos, che è stata la prima persona a credere in me quando nessuno ci credeva. Uomo di poche parole che ha segnato l’inizio della mia carriera dicendomi che se si ha un sogno bisogna inseguirlo. La sua conoscenza smisurata dell’ingegneria mi lascia ogni volta senza parole. È stato a suo modo guida, curando nei minimi dettagli il lavoro di questi anni di tesi. È grazie ai continui confronti e ai suoi incessanti insegnamenti che sono riuscito a risolvere problemi irrisolvibili.

Ringrazio l’amico, nonché secondo maestro, il Dr. Pasquale Cito. Colui che c’è sempre stato. Mi ha incoraggiato a fare sempre meglio, a non arrendermi mai. Mi ha insegnato che per riuscire non bisogna per forza essere duri, ma che lavorare con il sorriso è una strada valida.

Ringrazio il Professore Gaetano Della Corte. Nonostante il suo ruolo, è stato umile e paziente nello spiegarmi anche i concetti più semplici, senza mai dare nulla per scontato.

Non posso che esservi riconoscente di avermi fatto crescere sia come professionista che come uomo.

Non dimentico i miei compagni di viaggio, Antonio, Adriana, Roberto, Gaetano, Mabel e Francesco che mi hanno migliorato. Non dimentico il gruppo di amici che mi ha sempre sostenuto. Non dimentico le mie radici: mia nonna; e la mia linfa vitale: la mia famiglia, mia mamma, mio padre, i miei fratelli senza i quali non sarei nulla.

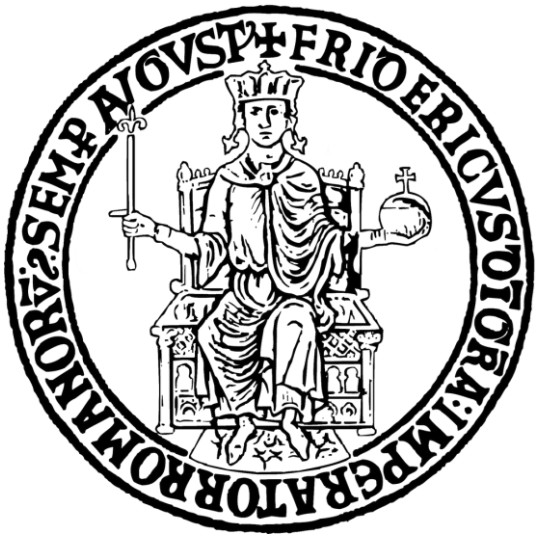
FRIDERICVS DEI GRA ROMANORVM IMPERATOR SEMPER AVGVST

Earthquake and Tsunami multi-hazard risk analysis of a petrochemical plant

Ph.D. Thesis presented

for the fulfilment of the Degree of Doctor of Philosophy

in Ingegneria Strutturale, Geotecnica e Rischio Sismico

by

ANTONIO VITALE

March 2024

Approved as to style and content by

_____

Prof. Iunio Iervolino, Advisor

_____

Dr. Georgios Baltzopoulos, Co-advisor

_____

Dr. Pasquale Cito, Co-advisor

Università degli Studi di Napoli Federico II

Ph.D. Program in Ingegneria Strutturale, Geotecnica e Rischio Sismico

XXXV cycle - Chairman: Prof. Iunio Iervolino

www.dist.unina.it/dottorati-di-ricerca/dottorati

Candidate's declaration

I hereby declare that this thesis submitted to obtain the academic degree of Philosophiæ Doctor (Ph.D.) in Ingegneria Strutturale, Geotecnica e Rischio Sismico is my own unaided work, that have not used other than the sources indicated, and that all direct and indirect sources are acknowledged as references.

Parts of this dissertation have been published in international journals and/or conference proceedings (see list of the author's publications at the end of the thesis).

Napoli, March 11, 2024

_____

Antonio Vitale

Abstract

One of the main triggering causes of industrial accidents is associated with the occurrence of natural events, like earthquakes, floods, tsunamis, hurricanes, or lightning storms. These phenomena can lead to structural damage to the industrial facilities causing the release of hazardous substances contained within them, initiating a chain of unpredictable cascading effects, potentially involving pool fire, blasts, or dispersion of toxic cloud. The study of the effects of the impact of natural phenomena on industrial facilities is the evaluation of the NaTech risk assessment. The term NaTech has been coined to describe such natural-hazard-triggered technological accidents.

The thesis presents a multi-hazard NaTech risk assessment for a petrochemical plant of an anchored storage tank farm exposed to earthquakes and tsunamis. This hypothetical waterfront liquefied petroleum gas tank farm is situated at a coastal Italian site supposed as case study.

Advanced probabilistic seismic hazard analysis and tsunami fragility functions for anchored storage tanks are developed, in this thesis, to contribute to a risk assessment that is not always easy to carry out. These two contributions are added to existing literature about probabilistic tsunami hazard analysis and seismic fragility curves, in order to integrate the hazard and vulnerability results for seismic and tsunami action and to provide the rates of the tank failure, where failure is intended as structural damage able to cause release of contents.

The results of the work of the thesis can be used to perform loss and consequence analysis looking at a wider context of multi-risk that takes into consideration the interaction between two natural phenomena.

Keywords: NaTech, risk, earthquake, tsunami, storage tank.

Sintesi in lingua italiana

Una delle principali cause scatenanti di incidenti industriali è associata all'occorrenza di eventi naturali, come terremoti, inondazioni, tsunami, uragani o tempeste di fulmini. Questi fenomeni possono causare danni strutturali agli impianti industriali, con conseguente rilascio di sostanze pericolose contenute al loro interno e l'inizio di una catena di effetti a cascata imprevedibili, che possono innescare incendi, esplosioni o dispersione di nubi tossiche. Lo studio degli effetti dell'impatto dei fenomeni naturali sugli impianti industriali è l'analisi del rischio NaTech. Il termine NaTech è stato coniato per descrivere tali incidenti tecnologici innescati da eventi naturali.

La tesi presenta una valutazione multi-hazard del rischio NaTech per un impianto petrolchimico, costituito da un parco di serbatoi di stoccaggio ancorati, esposto a terremoti e tsunami. Questo ipotetico impianto di serbatoi di gas liquefatto di petrolio situato sulla costa italiana è stato preso come caso studio.

In questa tesi, sono state sviluppate avanzate analisi probabilistiche di pericolosità sismica e funzioni di fragilità tsunami per serbatoi ancorati, per contribuire a una valutazione del rischio che non è sempre facile da eseguire. Questi due contributi si aggiungono a studi di letteratura esistente di analisi probabilistiche di pericolosità tsunami e curve di fragilità sismica, al fine di integrare i risultati di pericolosità e di vulnerabilità per sisma e tsunami per ricavare il tasso di fallimento dei serbatoi, dove per fallimento si intende il danno strutturale in grado di causare il rilascio dei contenuti.

I risultati del lavoro di tesi possono essere utilizzati per eseguire analisi delle perdite e delle conseguenze guardando a un contesto più ampio di multi-rischio che tiene conto dell'interazione tra due fenomeni naturali.

Parole chiavi: NaTech, risk, earthquake, tsunami, storage tank.

Contents

Acknowledgements

The author's work has been carried out in the framework of the PRIN 2017 (Progetti di Rilevante Interesse Nazionale) project "**Multi-risk assessment of the interactions among natural hazards and technological scenarios involving the release of hazardous substances - codice: 2017CEYPS8 CUP: E64I19000800005**".

I would like to express my gratitude to the scientific committee, Prof. Raffaele Landolfo and Prof. Gaetano Festa, for the careful and scrupulous evaluation of my PhD journey.

I would like to express my gratitude to the reviewers of this thesis, Prof. Katsuichiro Goda (Western University, Canada), Dr. Raffaele De Risi (University of Bristol), and Dr. Kostantinos Bakalis (University of Birmingham) for their valuable comments that helped me to improve the quality of my thesis.

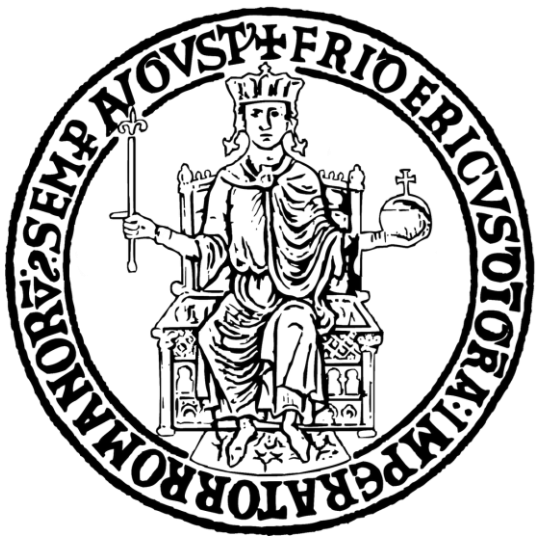
AVGVST FRIDERICVS DEI GRA IMPERATOR ROMANORVM SEMP

List of Acronyms

C	Capacity parameter
cdf	Cumulative density function
CS	Crustal Seismicity
D	Demand parameter
FEM	Finite Element Model
GMPE	Ground Motion Prediction Equation
IS	Interface subduction Seismicity
NaTech	Natural Technological accident
pdf	Probability density function
PGA	Peak Ground Acceleration
PSHA	Probabilistic Seismic Hazard Analysis
PTHA	Probabilistic Tsunami Hazard Analysis
QRA	Quantitative Risk Assessment
RV	Random Variable
UHS	Uniform Hazard Spectrum

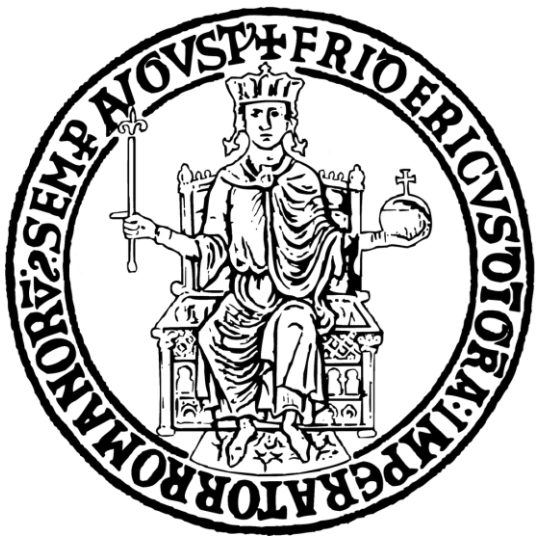
AVGVST FRIDERICVS DEI GRA IMPERATOR ROMANORVM SEMP

List of Figures

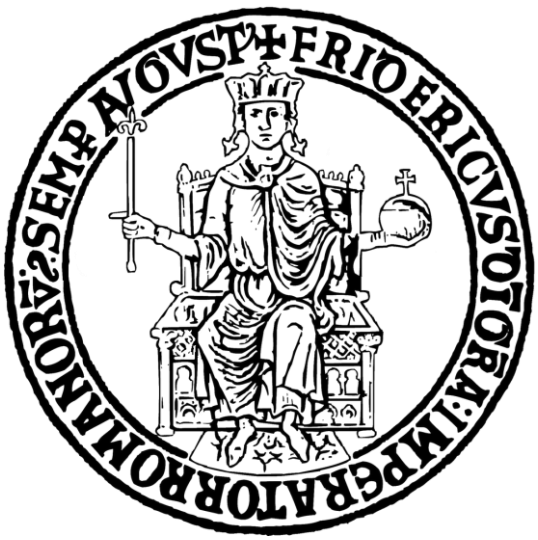
FRIDERICVS DEI GRA ROMANORVM IMPERATOR AVGVST SEMP

List of Tables

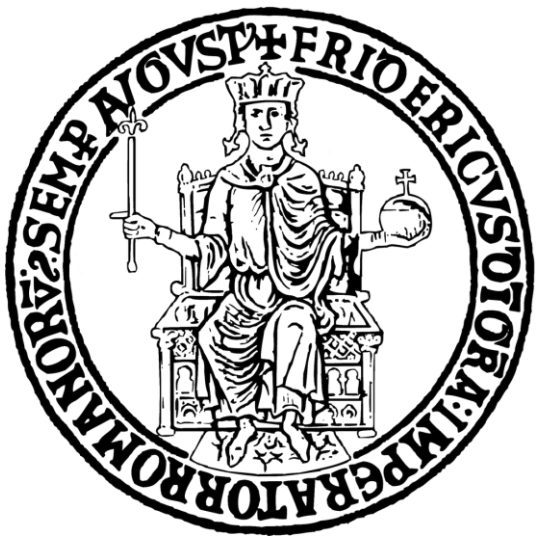
AVGVST FRIDERICVS DEI GRA IMPERATOR ROMANORVM SEMP

List of Symbols

$h_{f,max}$	Maximum height of the liquid content
h_f	Height of the liquid content
$h_{w,max}$	Maximum tsunami height of the time-history
h_w	Tsunami height
$\Phi_{(0.5)}$	Percentage of the submersion of the storage tank with the 50% of probability of failure
A_s	Nominal cross-sectional area of the anchor bolt
C_d	Hydrodynamic coefficient
F_T	Tensile force of anchor bolt
L_B	Bolt elongation length
M_w	Moment magnitude
$N_{u,C}$	Tensile concrete cone breakout strength
P_f	Hydrostatic pressure of the liquid content
P_{wd}	Tsunami hydrodynamic pressure
P_{ws}	Tsunami hydrostatic pressure
Q_f	Self-weight of the liquid content
R_{hyp}	Distance of the site from the hypocentre
R_{JB}	Joyner-Boore distance
R_{rup}	The closest distance of the site from the rupture
$\overline{U}$	Matrix of the of ID combinations of not failed storage tanks
V_{s30}	Shear velocity wave

$V_{u,s}$ Shear anchor strength

Z_{bot} Bottom part of the rupture surface

Z_{tor} Upper part of the rupture surface

d_B Diameter of the anchor bolt

f_{ck} Characteristic compressive cylinder strength of concrete

f_{ub} Ultimate tensile steel strength

i_B Spacing between anchors

mf_{max} Maximum momentum flux of the time-history

n_B Number of the anchor bolt

t_{ap} Thickness of the annular base plate

t_{bp} Thickness of the base plate

t_w Thickness of the shell wall

$\tilde{v}$ Flow velocity in correspondence of the maximum tsunami height

$v_{w,max}$ Maximum flow velocity of the time-history

v_w Flow velocity

w_{ap} Width of the annular base plate

α_c Coefficient that considers the uncertainty between the tested and designed tensile concrete breakout strength

α_v Coefficient that considered the uncertainty between the tested and designed shear strength of the anchor bolt

α_θ Coefficient that considers the geometrical imperfections and the fabrication quality

ρ_f Density of the liquid content

ρ_w Density of the sea water

$\sigma_{\theta,C}$	Compressive circumferential buckling stress threshold
$\sigma_{\theta,cr}$	Compressive circumferential critical buckling stress
$\sigma_{\theta,max}$	Peak average compressive circumferential stress of the shell wall
σ_{θ}	Compressive circumferential stress of shell wall
Φ	Percentage of the submersion of the storage tank
Ψ	Percentage of the filling level
A	Rupture area
BF	Buffer zone
D	Diameter of the storage tank
F	Failure
FM	Model for assessing the probability to observe a given focal mechanism
H	Height of the storage tank
L	Length along the strike
Mf	Momentum flux
R	Radius of the storage tank
RM	Model for assessing the occurrence of the earthquakes inside a given tectonic region
Reg	Tectonic region
S	Archimede's force
$Sa(T)$	Spectral acceleration
T	Period of vibration of the structure
Tr	Return period
U	Matrix of the of ID combinations of failed storage tanks

W	Length along the dip
ZM	Model for assessing the probability to observe seismic events inside a seismic zone of a given tectonic region
dip	Dip angle
im	Intensity measure
$rake$	Rake angle
$strike$	Strike angle
$zone$	Seismic zone
$\boldsymbol{\Theta}$	Focal mechanism vector

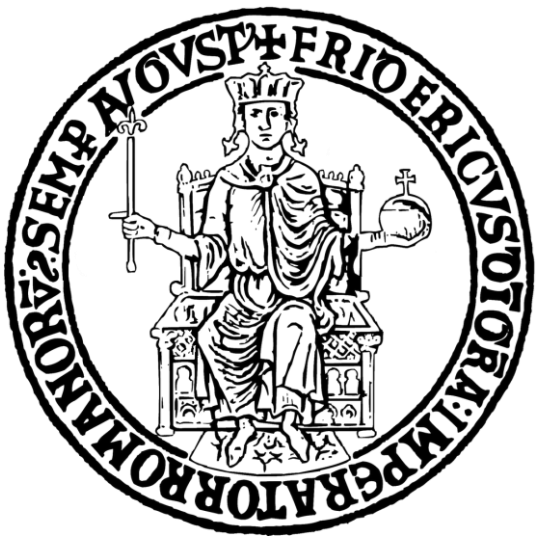
FRIDERICVS DEI GRA ROMANORVM IMPERATOR AVGVST SEMP

Introduction

True happiness lies in
completing the work using your brain
and your abilities.

_____

Soichiro Honda

The work of this thesis is focused on developing computational tools that can find application in **Q**uantitative **R**isk **A**ssessment (*QRA*) for industrial plants. The objective of *QRA* is to evaluate the likelihood and severity of potential natural hazards that could cause an industrial accident with harm to people, industrial facilities, or the environment. Thus, *QRA* is linked with NaTech risk assessment, which is the main focus of the thesis. The acronym NaTech stands for **Tech**nological accident due to **Na**tural event; following a natural event, like earthquake-induced ground shaking, flood, tsunami, hurricane or lightning storm, an industrial unit could experience a technological accident in the form of structural damage or a detachment of pipelines. Such technological accidents can lead to a release of contents that can become the triggering cause of a potential industrial accident. In fact, release of contents could be the main cause of a blast, pool fire, or dispersion of toxic clouds, with the possibility to cause further technological accidents to other industrial units, thus provoking a series of unpredictable cascading effects.

NaTech risk assessment has the aim to quantify the risk by defining the probability that a natural event could be cause of a technological accident that leads to the loss of contents of the industrial unit. These results can then be included in *QRA* to evaluate the probability of various consequences and the potential impact of those consequences. Risk assessment typically combines methodologies from different disciplines to obtain a probabilistic description of potential future losses. In this specific case, the interdisciplinary nature of the approach includes the geophysical aspect of earthquake recurrence and the evaluation of hazard at the site of interest, structural engineering for the study of the behaviour of the

facilities subjected to the consequences of the natural events and chemical engineering for the evaluation of the consequence analysis.

This thesis elaborates a NaTech risk analysis for a hypothetical petrochemical plant comprised of anchored atmospheric storage tanks focusing mainly on the first two components of the risk: the hazard and the vulnerability. Under this point of view, the thesis is organized in two branches, carrying out the hazard and vulnerability analysis for two natural events that could be cause of technological accidents to storage tanks, which are: the earthquakes and the tsunamis. This study was conceived in a multi-hazard context in which the tsunamis are triggered by the same seismic sources that cause ground shaking at the site of interest. Regarding earthquakes, probabilistic seismic hazard analysis is performed for a site subjected to the ground shaking coming from crustal and subduction events. This analysis is based on the classical approach of the hazard integral, with particular focus on the source model of crustal earthquakes represented by a finite fault geometry, accounting for the uncertainties linked to the orientation and the mechanism of the faults around the site of interest. The seismic vulnerability of the storage tanks, on the other hand, has been widely studied in the literature and for this reason the existing fragility models are used as reference to this risk assessment. On the other hand, regarding the tsunami part of the multi-hazard approach, probabilistic tsunami hazard analysis was developed in literature for the site in which the petrochemical plant is assumed to be located and adopted for this risk assessment. One of the main original contributions of this thesis is the evaluation of the tsunami vulnerability of anchored atmospheric storage tanks. The development of this fragility analysis takes into account uncertainties on both the action and resistance sides. More specifically, the structural response of tanks under tsunami action is the result of interaction of different potential damage modes that could lead to content release. Such structural damage can be triggered by different aspects of the tsunami loads, such as hydrostatic and hydrodynamic or buoyant forces, that scale differently with possible tsunami intensity measures, such as wave height, velocity or flux energy. For this reason, the study of the vulnerability cannot be separated from the study of the hazard at the site of interest, as one may be required to investigate the correlation between the different tsunami intensity measures observed during inundation scenarios. On the resistance side,

uncertainties, on the fabrication process of the shell wall and the tension and shear resistance of anchorage system, are taken into consideration.

The development of these interdisciplinary concepts was possible thanks to the collaboration both with the geophysics experts, though the group of Istituto Nazionale di Geofisica e Vulcanologia (INGV) with Prof. Jacopo Selva and Manuela Volpe; and the research group of chemical engineering under the guidance of Professors Valerio Cozzani and Ernesto Salzano of Alma Mater Studiorum – University of Bologna.

The contents of the thesis are organized in the following four chapters, which are summarized below.

Chapter 1 presents seismic and tsunami hazard analysis for the site hosting the case-study plant. The first section describes the seismic sources that trigger both ground shaking and tsunami around the site. The second section presents the results from the probabilistic seismic hazard analysis. The third section shows the available probabilistic tsunami hazard analysis results from literature. The fourth section uses the tsunami hazard results to derive conditional tsunami hazard models which, in turn, are helpful to the development of tsunami vulnerability analysis.

Chapter 2 develops tsunami vulnerability analysis, deriving fragility functions for anchored atmospheric storage tanks with floating roof. The first section describes the methodology to obtain the fragility functions, while the finite element model adopted the structural analysis is presented in the second section. The third section shows the results of structural analysis and describes the parametric model used to represent the fragility functions.

Chapter 3 introduces a series of case studies for the evaluation of NaTech risk assessment, which are developed starting from the results presented in the previous chapters. The first section summarizes the methodology of risk assessment. The second section shows the results of case studies. The third section shows an example of cascading effects with the contemporary failure of multiple tanks and introduces a framework to perform a multi-risk losses analysis.

Chapter 4 summarizes the main findings obtained in the thesis work.

Lastly, the Appendix contains a more detailed account of the design of the archetype anchored tanks, using European and American standards.

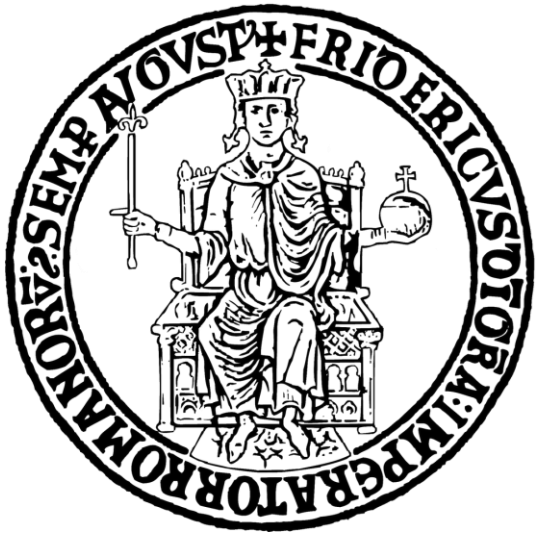
AVGVST FRIDERICVS DEI GRA IMPERATOR ROMANORVM SEMP

Chapter 1

Probabilistic seismic and tsunami hazard analysis: application for a petrochemical plant

I am a slow walker, but I never walk back.

Abraham Lincoln

Multi-hazard risk analysis considers systems that can be threatened by more than one natural hazard, such as coastal infrastructure in seismically active regions, that can be subjected to both earthquakes and tsunamis. Past works on this topic have examined multi-hazard modelling for earthquakes and tsunamis assuming different connotations [1]. Examples are De Risi and Goda [2] that developed a multi-hazard methodology for evaluating seismic and tsunami hazards simultaneously, and Maeda et al. [3] that provided methods for carrying out seismic- and tsunami-wave propagation simulations to model cascading hazards. More often than not, in multi-hazard analyses, single hazards are considered separately, even though the natural processes can be linked rather than independent [4–6] and hazard interactions may produce effects that are not captured with single-hazard analysis. Furthermore, several authors adopt differing approaches to multi-hazard analysis, under the labels of cascading hazards [7], hazard interaction [8] or compound hazard [9]. In other words, multi-hazard analysis is used for

the risk assessment considering the simultaneous or sequential occurrence of multiple hazards at the site of interest. Rather than analysing each hazard individually, multi-hazard analysis should ideally take into account the interactions and combined effects of various natural events. This approach allows a more accurate assessment of risk management and mitigation. The hazard analysis quantifies how much a site of interest (e.g., construction site) is threatened by a natural phenomenon, evaluating, with probabilistic approaches, the rate of events whose intensity exceeds a certain threshold. Measures of the intensity of a natural event are physical quantities that characterizes the event itself. For instance, one (widely known) ground motion intensity measure is the peak ground acceleration (*PGA*), or the wave height or velocity for tsunamis. The use of probabilistic approaches leads to evaluating the right compromise between the accuracy and precision of the hazard results and the practical feasibility [10]. A natural event has an intrinsic aleatory nature, considering that it is unknown when and where happens, with which intensity and from which scenario is triggered. An accurate modelling of the phenomenon can, for this reason, require computational problems.

In this chapter, probabilistic tsunami and seismic hazard analysis are developed for a site located near the Thyrrenean coast of Sicily, where a hypothetical petrochemical plant is assumed. In this thesis, the concept of multi-hazard is more akin to, previously mentioned, cascading hazard, because the case is investigated where ground shaking and tsunamis may be triggered by the same seismic events.

The tsunamis are natural events that have a lower occurrence than to other natural events [11], but are phenomena that may lead to massive damage, with large economic losses especially to the building located near the coast, but also losses of human life. Tsunami does not happen alone but is always triggered by another natural event. Historical tsunami database of NOAA 2016 [12] shows that most of tsunami events are triggered by seismic events; while other sources of tsunami waves can be volcanic eruptions, submarine landslides, atmospheric disturbances, or asteroid impacts. Marine earthquakes can cause sudden deformations of the seafloor with subsequent displacement of the water column above. During the earthquake (coseismic period), the vertical displacement of the water column gives rise to a tsunami, which is directly linked to the vertical

displacement of the sea floor. In some cases, also the horizontal displacement component can contribute to the tsunami generation, in particular, this is true for the subduction zones [11]. Large earthquake magnitudes generally produce large coseismic deformations that trigger large tsunamis. Examples of historical devastating tsunami triggered by earthquakes are Sanriku (Japan) 1896 with moment magnitude (M_w) equal to $M_w = 8.3$, and Sumatra (Indonesia) 2004 with $M_w = 9.1$. These two earthquakes caused 27122 and 227899 victims respectively. The events at Southern Chile 1960 ($M_w = 9.5$) and Tohoku (Japan) 2011 ($M_w = 9.1$), instead, caused thousands of destroyed buildings, with the Tohoku earthquake also providing damage at nuclear power plant of Fukushima. Historical catalogue shows that significant tsunami events are particularly expected in active subduction zones while are less likely to occur in crustal seismogenic regions as the Mediterranean Sea [2]. In this area, in the last one hundred years, there were observed one hundred tsunami events and sixty-four of these were triggered by a seismic event (see tsunami database [12]).

Results from the probabilistic seismic hazard analysis (*PSHA*) are the hazard curves or the hazard maps, among others. The hazard curves show the rates of earthquakes causing exceedance of selected intensity measure thresholds. The hazard maps collect the intensity measure values that, at each site (among some of interest) taken individually, have the same exceedance rate. For what will be discussed in this chapter, conditional tsunami hazard has to be mentioned too. Conditional hazard can be used to build, at one site, the distribution of an intensity measure, conditional to a specific value of another intensity measure at the same (or even different; [13,14]) site. From the seismic hazard site, the *PSHA* [15] is developed using simplifications that make the hazard assessment realistically feasible, for example, adopting empirical ground motion prediction equations (*GMPE*) instead of an explicit numerical simulation. In other cases, however, these simplifications can lead to inaccurate hazard estimates and the aleatory uncertainty of the phenomenon is considered by running Monte Carlo simulations.

On the other hand, tsunami hazard analysis relying on probabilistic approach was object of discussion of numerous past studies. Geist et al. (2006) [16] explain that there are several issues pertaining to the evaluation of tsunami hazard. First, there is a recognized difficulty in

developing attenuation relationships based on empirical data, because historical records are available only for particular locations. The identification of a well-defined area where to evaluate the hazard is also tackling, because seismic sources that may trigger relevant tsunami can be located at distances several times far from the site of interest. Lastly, tsunami measurements are limited. In lack of empirical data, several authors, as Sørensen et al. (2012) [17] proposed a probabilistic tsunami hazard analysis (*PTHA*) based on the simulation of earthquake catalogues that trigger tsunamis. For each event in the catalogue, the hazard is evaluated as combination of the effects of all tsunami propagation scenarios at the site of interest. Similarly to *PSHA*, tsunami hazard assessment relies on the knowledge of source parameters, recurrence rates and their uncertainties. The most straightforward approach is that of Ward (2002) [18] that highlights the substantial difference between *PTHA* and *PSHA* regarding the characterization of intensity measures in an event with specific features. More specifically, within *PTHA*, the displacement of the water column is evaluated at the source, first and then the propagation up to coastal site is determined by means of numerical simulations. In the case of *PSHA*, the ground shaking at site of interest is probabilistically characterized, via *GMPEs*, conditional on the features of the earthquake, such as magnitude and site-source distance, to say the least.

The object of this chapter is to carry out a multi-hazard analysis, combining *PSHA* and *PTHA* results, for the site of Milazzo in north-Sicily, found on the Thyrrenean coast. This site is taken as a case study because Lorito et al. (2015) [10], before, and Selva et al. (2016) [19], then, formulate an explicit numerical model based on the development of an event tree that quantifies the aleatory and epistemic uncertainties of seismic sources in this area taken as case study. In more detail, the *PSHA* is carried out considering the source model of Selva et al. (2016) [19]; while for *PTHA*, the available literature hazard results from Volpe et al. (2019) [20] are used as a basis to develop conditional hazard models that will be adopted to derive tsunami fragility curves, discussed in Chapter 2. Thus, this chapter is structured as follows: first paragraph describes the seismic sources used within *PSHA* and *PTHA*; in the second paragraph, *PSHA* is discussed in detail, while the *PTHA* is briefly recalled in third paragraph;

section four introduces conditional hazard and illustrates the correlation models used within such an analysis.

1.1 Seismic sources and ground motion prediction equation for subduction faults

This section deals with the characterization of the seismic sources of the Mediterranean area, based on the model of Selva et al. (2016) [19], which is used in the hazard analysis presented in the following of the chapter. As mentioned above, this model is shared by *PSHA* and *PTHA*. In fact, this study considerers only tsunamis triggered by earthquakes, and it is assumed that earthquakes and tsunamis occur from the same seismic sources, which are faults. The system of faults in the Mediterranean Area consists of crustal faults and two subduction faults, Calabrian and Hellenic Arc. The tsunamis can be triggered by both seismicity classes. The source models of both classes are defined by grids. The crustal source model is based on a regular grid that covers the whole Mediterranean Area, while the subduction source model on a grid that covers only the part of the subduction considered seismically active. The crustal domain is shown in Figure 1.1 and is characterized by cells of 25 km x 25 km of area, and their centres are the epicentres of crustal earthquakes. The system of faults in the Mediterranean Area is the result of the interaction of tectonic movements of African, Eurasian, and Aegean plates. In more detail, African oceanic crust pushes beneath the continental crust of European Plate forming the subduction fault of Calabrian Arc, and beneath the Aegean Plate giving rise to Hellenic Arc. This general understanding allowed Selva et al. (2016) [19] to divide the whole Mediterranean Area in homogenous tectonic regions, thus identifying zones where the faults have likely the same behaviour in terms of orientation and movement. The boundaries of tectonic regions are shown in Figure 1.1 and are based on geological and tectonic information stemming from various maps and databases, including the Geological Map of Europe [21], CRUST 1.0 [22] and EPCRUST [23].

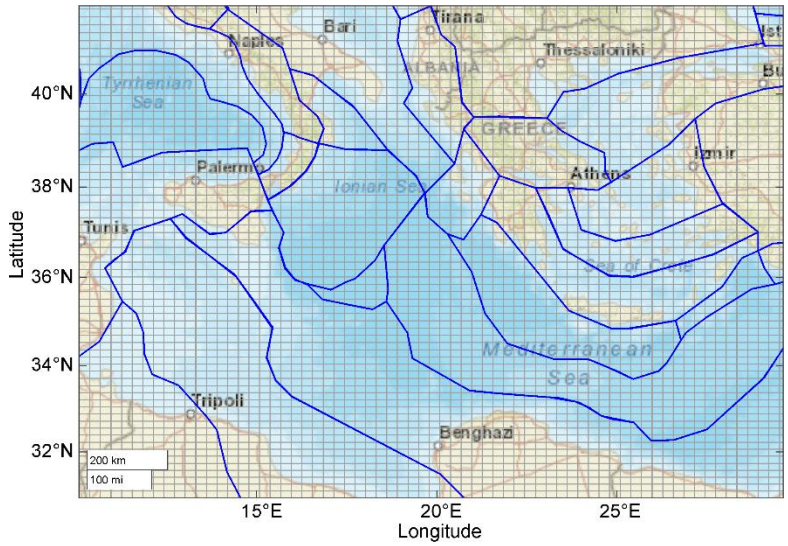

Figure 1.1: Discretization of the crustal sources and tectonic regions of the Mediterranean area.

The tectonic regions are classified into subduction and crustal zones. Types of crustal regions are oceanic and continental crust; that can be stable or active. The active zones are classified according to predominant tectonic regime such as extensional, contractional or strike-slip. For each region, the seismicity is defined by the European-Mediterranean Earthquake Catalogue (EMEC), which contains information about epicentral location, depth, and magnitude of events from 1000 to 2006 [24,25]. In crustal regions, only crustal earthquakes can occur, while in subduction regions, seismic events can occur both on the subduction surface (interface or intraslab events) and on the crust. In addition, it is assumed that the events for both seismicity classes occur with a stochastic homogeneous Poisson process, thus, the frequency of the seismic events can be evaluated keeping separated the contributions of two seismicity classes.

Inside the Mediterranean Area, a characterization (done by Selva et al. (2016) [19]) of the faults that trigger tsunamis, in terms of geometry, kinematics, and activity rates, is based on the work of Basili et al. (2013) [26] that study the importance of the selection of the tsunamigenic faults and their possible impact onto hazard analysis results. The results of work

of Basili et al. (2013) [26] are stored in the European Database of Seismogenic Faults (EDSF) [27].

The tsunami and seismic hazard analysis is performed for the site of Milazzo (ME) in Southern Italy. The location of this site is shown in Figure 1.2 with a triangle. For the hazard analysis, between all sources of the crustal domain, only ones that trigger a tsunami at the site of interest are taken into account and are shown in Figure 1.2 with orange circles. In addition, the depicted blue circles represent the epicentres of subduction earthquakes of the Calabrian Arc. The subduction earthquakes of the Hellenic Arc do not trigger tsunami at the site of interest.

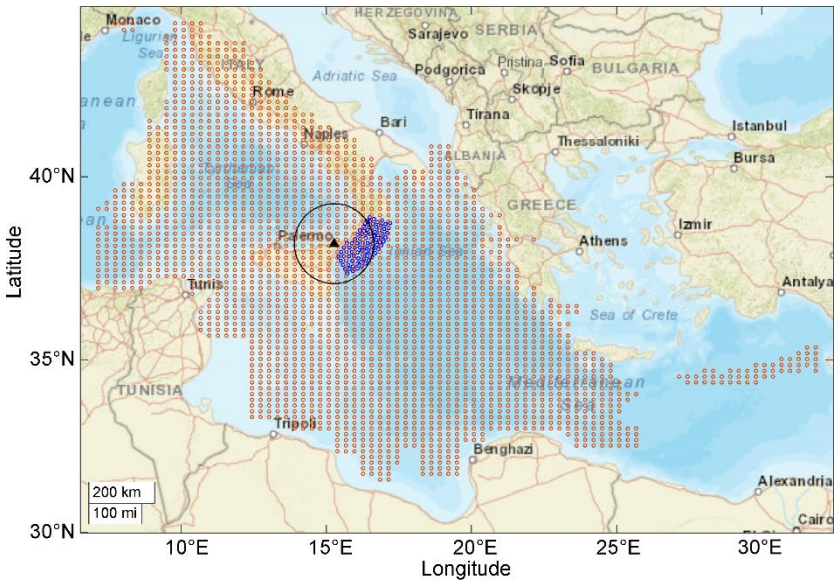

Figure 1.2: Tsunamigenic sources for crustal and subduction earthquakes at the target site of Milazzo (Sicily, Italy).

While the tsunami hazard analysis is developed using seismic sources from the entire Mediterranean area, the seismic hazard analysis is performed only considering sources within a $100\ km$ radius around the site of interest. The choice to select an area of $100\ km$ around the site depends on the effects of site-source distance. In fact, if a source is very far from the site, an earthquake could not cause damage and to have negligible impact at the site. Contrary, a tsunami coming from a far source

may provoke significant effects to the site of interest, as damage to the structures. For these reasons, the *PSHA* considers a limited area around the site of interest where it is deemed suitable to consider the impact of ground shaking, while the assessment of the tsunami hazard takes into account both effects of far and near field, meaning tsunami coming from far and near seismic sources to site of interest.

Figure 1.3-a) shows a zoom of the area of interest for the *PSHA* highlighting the tectonic regions that fall inside this area. Six are the tectonic regions inside of this area and, in figure, each area is defined by an identifier name and the corresponding tectonic regime. Figure 1.3-b) shows, instead, the cells of the crustal domain contained inside the area of interest for the *PSHA*, and each cell belongs to a tectonic region, identified with different colours. In addition, it is observed that this area also contains a part of the subduction zone of the Calabrian Arc.

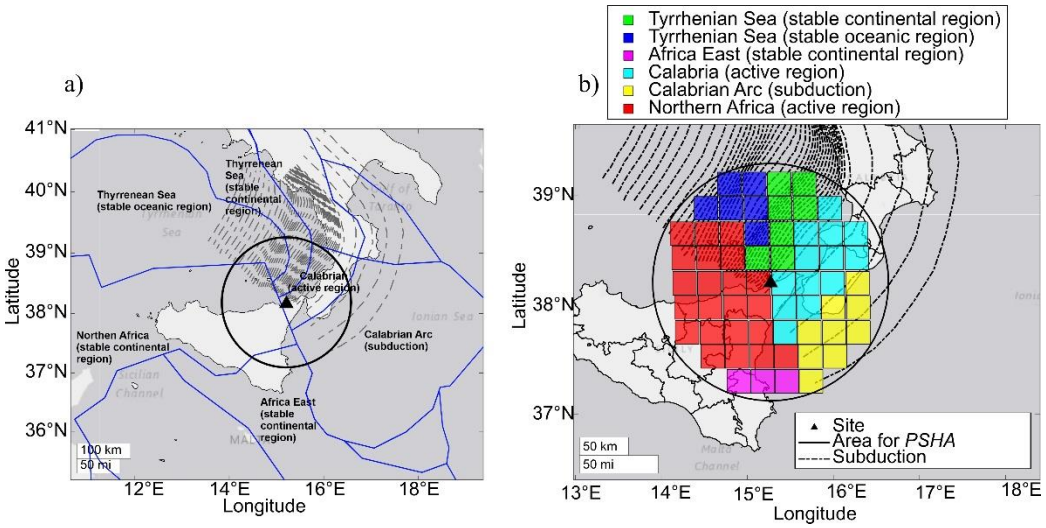

Figure 1.3: a) Tectonic regions inside of the area of interest for *PSHA*. b) Crustal seismic sources considered for *PSHA*.

1.1.1 Finite fault modelling for crustal seismicity

The source model used for the crustal earthquakes is based on the finite fault geometry. The fault modelling considers that the rupture

happens along a plane having a defined orientation in space. Along fault plane, a rectangular area identifies the rupture. As an example, one finite fault model is shown in Figure 1.4. Here, the fault rupture is completely defined by means of three angles that define the focal mechanism of an earthquake: the dip angle (dip) that represents the slope of the fault plane respect to the horizontal plane; the strike angle ($strike$), indicating the exact orientation of the fault trace measured clockwise from the North; and the rake angle ($rake$), that defines the movement of two sides of the fault. An example of the meaning of rake angle is represented in Figure 1.4-a) that shows the foot wall of the fault, and the vector $\boldsymbol{u}$ identifies the relative movement of the hanging wall. Figure 1.4-b) shows the extent of rupture that is characterized by the following geometry: the length along the dip, W; the length along the strike, L; and two depths from the ground level, the upper part of the rupture surface, Z_{tor}, and the bottom part, Z_{bot}. Shear dislocation is assumed to propagate bilaterally in all directions from the hypocentre, which is therefore placed at the centroid of the rectangular rupture surface. The size of the rupture area is evaluated using the scaling empirical relationship of Wells and Coppersmith (1994) [28], which gives the median value conditional on magnitude and $rake$. It should be noted that this scaling relationship is only applied only to crustal events.

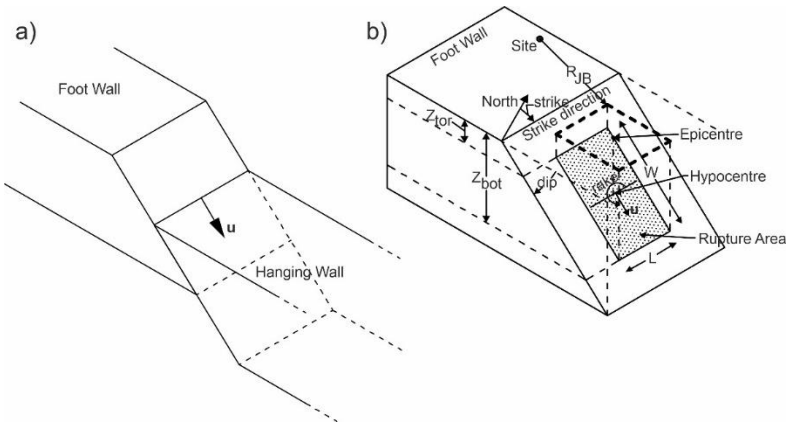

Figure 1.4: a) Movement between hanging wall and foot wall. b) Finite fault geometry.

For the hazard assessment object of this chapter, only 4 $rake$ values are considered, that is, $-90°$, $0°$, $90°$, $180°$. Rake angles of $0°$ and

$180°$ imply that the hanging wall moves horizontally to the strike direction and in this case the fault style is strike-slip; for $rake = 90°$ the hanging wall moves from the bottom to top and is a thrust fault; vice versa when the hanging wall moves from the top to bottom, the fault is normal and $rake = -90°$.

Table 1.1 shows the values of $rake$, dip and $strike$ used for this case study. The values of the angles in table are the bin centres of width of $45°$, $20°$ and $90°$ respectively for $strike$, dip and $rake$. These intervals are used to assess the probability of occurrence of focal mechanisms. In fact, for each $strike$, dip and $rake$ combination, a probability of occurrence is given. Some combinations are excluded in the evaluation of the probability of occurrence because considered unlikely faulting mechanisms. In detail, for strike-slip faults, the dip can be only equal to $70°$ and $90°$. For dip equal to $90°$, only $strike$ values of $22.5°$, $67.5°$, $112.5°$, and $157.5°$ are allowed. For thrust and normal faults, dip equal to $10°$ and $70°$ are excluded, respectively. Thus, the number of combinations considered in the analysis is 72.

Table 1.1: Angles used for *PSHA* [19]**.**

rake [°]	-90	0	90	180				
dip [°]	10	30	50	70	90			
strike [°]	22.5	67.5	112.5	157.5	202.5	247.5	292.5	337.5

The model of Wells & Coppersmith (1994) is based on least-squares method. For this study, the regression of M_w and base-10 logarithm of surface rupture area (A) and subsurface rupture length (L) (corresponding to length along the strike) are used for the *PSHA*. Table 1.2 e Table 1.3 show the regression laws with the corresponding regression coefficients indicated with symbols a and b, and the standard deviations of the base-10 logarithm of the dependent variables $\sigma_{log_{10}(A)}$ and $\sigma_{log_{10}(L)}$, depending on the fault style.

Table 1.2: Regression coefficients of surface rupture area [28]**.**

Equation	Fault style	a	b	$\sigma_{log_{10}(A)}$
$log_{10}(A) = a + b \cdot M_w$	Strike-Slip	-3.42	0.90	0.22
	Reverse	-3.99	0.98	0.26
	Normal	-2.87	0.82	0.22
	Unknown	-3.49	0.91	0.24

Table 1.3: Regression coefficients of subsurface rupture length [28]**.**

Equation	Fault style	a	b	$\sigma_{log_{10}(L)}$
$log_{10}(L) = a + b \cdot M_w$	Strike-Slip	-2.57	0.62	0.15
	Reverse	-2.42	0.58	0.16
	Normal	-1.88	0.50	0.17
	Unknown	-2.44	0.59	0.16

In these tables, A is expressed in km^2 and L in km. The residuals have low standard deviations. Using least-squares regression analyses, the probability density functions (*pdf*) of the residuals have lognormal distributions. An example of *pdf* of residuals of two parameters, $f(A)$ and $f(L)$, is shown in Figure 1.5 for a $M_w = 7$ and thrust fault style.

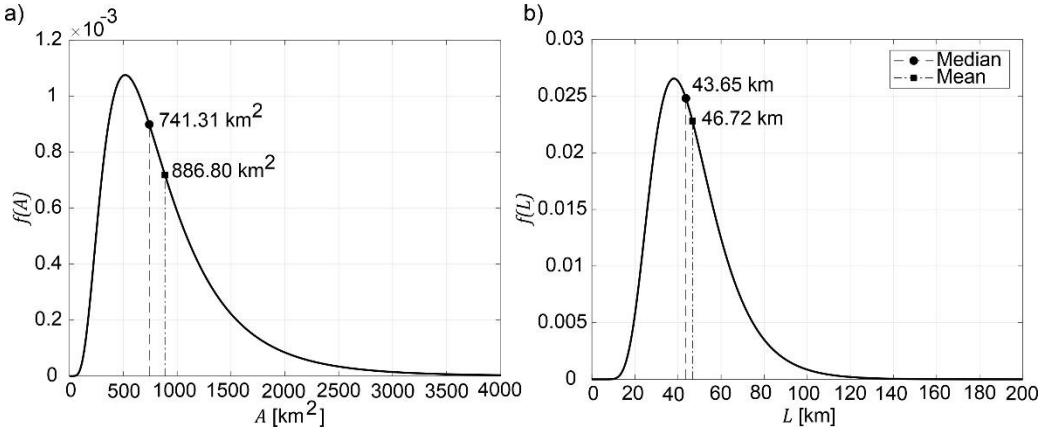

Figure 1.5: a) *pdf* of residuals of rupture area; b) *pdf* of residuals of rupture length.

According to the model, an estimated median and mean rupture area of 741.31km^2 and 886.80 km^2, respectively, are associated with a

magnitude $M_w = 7.0$ earthquake; under the same magnitude, the median rupture length is 43.65 km, whereas the mean is 46.72 km. In the hazard analysis, the uncertainty affecting rupture's dimensions was not accounted for, since a sensitivity study showed that its effect on the final results could be neglected.

As pertaining to Z_{tor} , some assumptions were considered, depending on the style of faulting and magnitude. The rectangles shown in Figure 1.6 represent ruptures for different magnitudes. More specifically, panel a) refers to normal and thrust fault and panel b) to strike-slip fault. For both normal and thrust cases, the rupture corresponding to the largest magnitude considered for the *PSHA* has $Z_{tor} = 0\ m$, implying that the trace of the fault is located on the ground plane. All rupture areas have own barycentre coinciding with the barycentre of the greatest rupture area, and, in addition, all the ruptures are coplanar. For the strike-slip faults, instead, the assumption is that all rupture areas have $Z_{tor} = 0\ m$, and in this case, the barycentre depth of all ruptures varies with the magnitude, in particular low magnitude implies shallow earthquake.

This type of source model is used to give information about the spatial distribution of the seismic event. However, in literature (e.g. [29]), this approach is adopted only for events of low and intermediate magnitude, as for magnitude values greater than 7, such rupture simulations may not be suitable. In these cases, it is preferable to consider multi-segment fault geometries where ruptures should be modelled spanning contiguous parts of each segment. Since information about the complex fault system of the area of the interest is not available, the source model based on the rupture simulations is adapted also to events with higher magnitude values out of necessity.

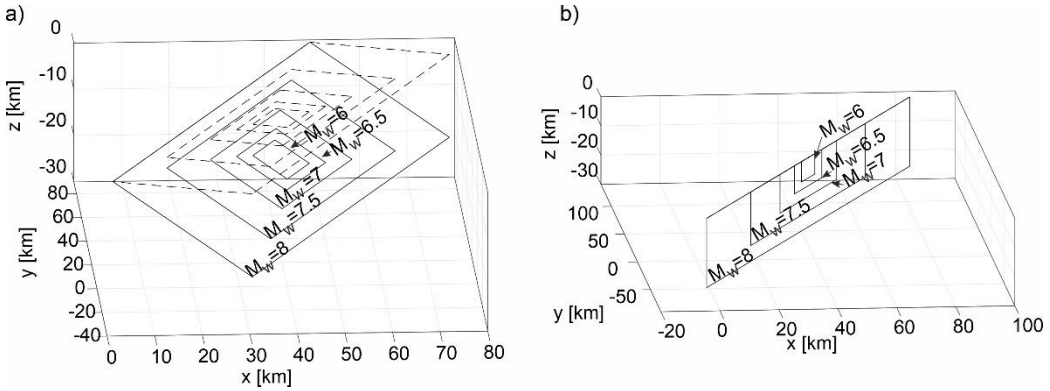

Figure 1.6: Rupture area for different magnitude for a) normal and thrust faults and b) for strike-slip faults.

1.1.2 Subduction interface modelling

Seismic events on the subduction fault can occur both on the interface and on the intraslab zone. The interface belongs to the uppermost part of subduction having low angle of sliding, while intraslab part is characterized by very high sliding, such as subduction fault reaches very high depths. On the interface, earthquakes can occur causing very large rupture widths. Because generally subduction boundaries are long, the combination of large widths and lengths allows to active very large ruptures. Indeed, earthquakes with high magnitude are associated with interface events. On the other hand, intraslab events occur at very high depths and the energy released by the earthquakes is strongly attenuated before arriving at the surface [30].

The subduction fault considered for *PSHA* is the Calabrian Arc, shown in Figure 1.7. Panel a) shows the extension on map of Calabrian Arc, while panel b) represents a 3D-reproduction of whole subduction zone. In each panel, the depth is represented via colour bar. The information derived from figure are taken from EDSF [27] and INGV (personal communication). On map, the subduction interface is shown from red lines not very dense, and the intraslab zone is depicted with the lines with other colours though very close lines. More specifically, the subduction interface extends from $10\,km$ to $40\,km$ of depth, while the intraslab zone reaches $440\,km$ of depth. In addition, a value of modulus of

rigidity equal to $30\ GPa$ is assumed, while considering the slip uniform over the rupture area [19]. This uniform slip value is the mean slip value from the scaling law of Strasser et al. (2010) [31].

For the hazard assessment, only the subduction interface is modelled, while subduction intraslab zone is not taken into account. The subduction interface is, typically, characterized by two parts, the nucleation and propagation zone. The nucleation zone is the part of the interface considered seismically active, where the hypocentres of the earthquakes are located. The propagation zone, instead, is the remaining part of the interface in which is expected the propagation of the rupture surfaces of the earthquakes that happen inside the nucleation zone. In this zone, no earthquakes happen. Three zones in which the subduction is divided are depicted in Figure 1.7-a). For sake of clarity, the interface is enclosed in a polygon distinguishing the two parts: the nucleation and the propagation zones.

The source model used in the hazard assessment for the subduction interface is based on a slab model with a certain sliding with respect to the horizontal plane that covers only the nucleation zone. The propagation zone is not modelled. This slab is shown in Figure 1.7-b) though a polygon (the black one). This polygon is discretized into a rectangular mesh in which the centres of each cell are hypocentres of hypothetical subduction interface earthquakes. Each hypocentre can trigger an earthquake with different values of magnitude. It is clear that earthquakes that happen near to the boundary of the nucleation zone or earthquakes with high magnitude, may trigger rupture surfaces that cannot be contained completely inside the nucleation zone but should necessarily interest also the propagation zone. The source model does not take into consideration these cases because the rupture areas are not modelled. This limitation of the model, which considers only the hypocentres, leads to an approximation on the hazard results. Specific scaling law relationships for subduction earthquakes could be, Strasser et al. (2010) [31], Thingbaijam et al. [32], Goda et al. [33].

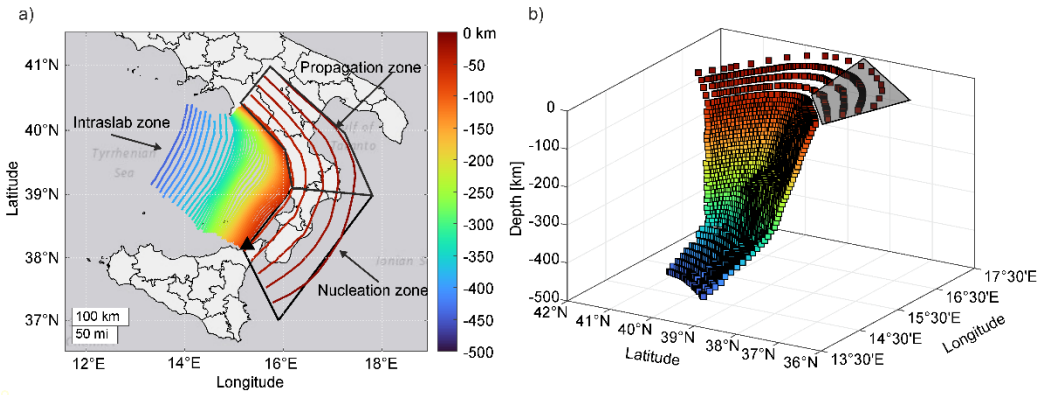

Figure 1.7: a) Calabrian Arc. b) 3D representation of the Calabrian Arc.

Figure 1.8 shows the projection on the horizontal plane of the nucleation zone, in cartesian coordinates for giving an order of magnitude of the extent of this part of the subduction interface. The centres of the cells of the mesh, reported in figure with a 'x' marker, are the epicentres of potential earthquakes. It is noted that some cells of the mesh belong to two tectonic regions considered for the *PSHA*, in particular, 37 cells belong to Calabria (active region) region, called for brevity cyan region and 23 cells to the Calabrian Arc (subduction) region, called yellow region. This discretization of the nucleation zone is arbitrary and serves only for the evaluation of the seismic hazard. A denser discretization is provided for the tsunami hazard assessment. This implies that the number of hypocentres, or equivalently of cells, that trigger tsunami, as well as earthquakes, are much more but this difference does not influence the results of seismic hazard.

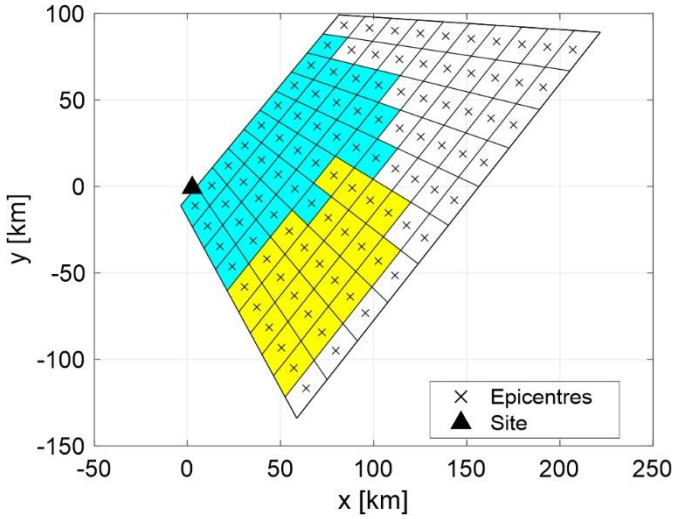

Figure 1.8: Discretization of the interface subduction slab.

1.1.3 Evaluation of occurrence rates of earthquakes

Having defined the source model, the occurrence rate, intended as the number of earthquakes that in one year occur at a seismic source with a value of moment magnitude M_w equal to m (within an interval with finite width centred at m, in fact; i.e., the so-called activity rate), must be defined. With reference to Figure 1.3-a), the occurrence of crustal earthquakes is defined for the 6 tectonic regions in the area of interest, distinguished by different colours in figure, and in particular for the 60 seismic zones, identified by cells of grid (called, herein, in equations: $zone$). For the subduction earthquakes the occurrence rates are evaluated for two tectonic regions located on the interface. Thus, these seismic zones have two occurrence rates distinguished between crustal and subduction earthquakes. The data showed in this section are taken from [19].

The occurrence rate of a seismic zone can be evaluated starting to the rate of corresponding to tectonic region. Thus, the occurrence rate of earthquakes of a zone belongs to tectonic region (Reg), is given by Eq.(1.1)

$$\lambda\left(M_w = m, \mathrm{Reg}\right) = \lambda\left(M = m \,|\, \mathrm{Reg}\right) \cdot P\left[\mathrm{Reg}\right] \tag{1.1}$$

that shows the product between the $\lambda(M_w = m|Reg)$, which is the occurrence rate of earthquakes with $M_w = m$ in the region Reg, and $P[zone, Reg]$, that is, the probability to observe an earthquake in a $zone$ of the region Reg. Therefore, the occurrence rate of a region $\lambda(M_w = m, Reg)$ can be evaluated as sum of occurrence rates of seismic zones in which the region is divided. Eq.(1.2) expresses this relationship:

$$\lambda\left(M_w = m, \mathrm{Reg}\right) = \sum_{k=1}^{n_{zones}} \lambda\left(M_w = m, zone_k, \mathrm{Reg}\right) \tag{1.2}$$

Where $k = 1, \dots, n_{zones}$ is and index that indicates the number of zones of a given region.

Two terms of Eq. (1.1) are evaluated following the approach of Selva et al. (2016) [19] based on an event tree. The event tree explores the aleatory uncertainty going to investigate alternative implementations but also the epistemic uncertainty giving to each alternative a weight. The alternatives are the branches of the event tree, while their weights identify the probabilities to be the best model. In this context, the set of implementations is mutually exclusive and collectively exhaustive. In more detail, 192 models are used for evaluating $\lambda(M_w = m|Reg)$, indicated with symbol RM, and 16 models for the assessment of $P[zone, Reg]$, indicated as ZM. Then, a probability, or equivalently a weight, is associated with each model: $P[RM]$ and $P[ZM]$. In addition, the same event tree with the same models is built considering seismic events that happen at different depths, in particular 5 km, 10 km, 15 km. These three depths are named in the following buffer zones (BF), with the same probability $P[BF]$ to be the more likely depth of seismic event. Lastly, this speech can be summarized in Eq.(1.3) and Eq.(1.4).

$$\lambda\left(M_w = m \,|\, \mathrm{Reg}\right) = \sum_{z=1}^{3}\sum_{i=1}^{192} \lambda\left(M_w = m \,|\, BF_z, RM_i, \mathrm{Reg}\right) \cdot P\left[BF_z\right] \cdot P\left[RM_i\right] \tag{1.3}$$

$$P\left[zone, \mathrm{Reg}\right] = \sum_{z=1}^{3}\sum_{j=1}^{16} P\left[zone, \mathrm{Reg} \,|\, BF_z, ZM_j\right] \cdot P\left[BF_z\right] \cdot P\left[ZM_j\right] \tag{1.4}$$

Where $\lambda(M_w = m|BF, RM, Reg)$ is the occurrence rate of earthquakes with $M = m$ occurred in the tectonic region Reg at a depth BF, evaluated with model RM; and $P[zone, Reg|BF, ZM]$ is the probability that an earthquake could occur in a $zone$ of the tectonic region Reg, located at a depth BF, evaluated with the model ZM.

This procedure can apply to each region, both for the rates associated with crustal seismicity (CS) and interface seismicity (IS). Figure 1.9 shows, an example of activity rates evaluated for different threshold of magnitude for the cyan and yellow regions. As discussed above, these regions are characterized by two seismicity classes: CS and IS. The figure shows in top row the occurrence rates of CS; while the bottom row, the occurrence rates of IS, for the case of cyan region in the first column and yellow region in the second one. The panels a) and b) show the rate of occurrence for *CS*, $\lambda^{CS}(M_w = m, Reg)$, illustrated by black line, while coloured lines are the occurrence rates of the zones of the corresponding region. Panels c) and d) show the rate of occurrence for IS, $\lambda^{IS}(M_w = m, Reg)$. Here, the rates of occurrence of the individual zones are not depicted because depending on the discretization of the slab model of the subduction zone, in particular, it is possible to assume that the rate is uniformly distributed between all cells of the discretization. It can be seen that CS rate is for the cyan region (panel a), at $M_w = 5$ equal to 10^{-2} event per year, while for the yellow region (panel b), at the same magnitude, the rate is equal to 10^{-4}. Both regions have a drop for $M_w = 7.9$, meaning that earthquakes with that magnitude are rare. On the other hand, the seismic activity on *IS* leads to events with magnitude larger than 8, up to 9.4 where rates of $4 \cdot 10^{-7}$ and $4 \cdot 10^{-8}$ are shown for cyan (panel c) and yellow (panel d) region, respectively. Regarding to the rates of the CS zones, the zones enumerated as 4 and 5, in figure panel a), for the cyan region, have the highest rate with the distance of $25\ km$ and $50\ km$ respectively to the site. For the yellow region, instead, all zones have the same rate, in fact, the curves are all overlapped.

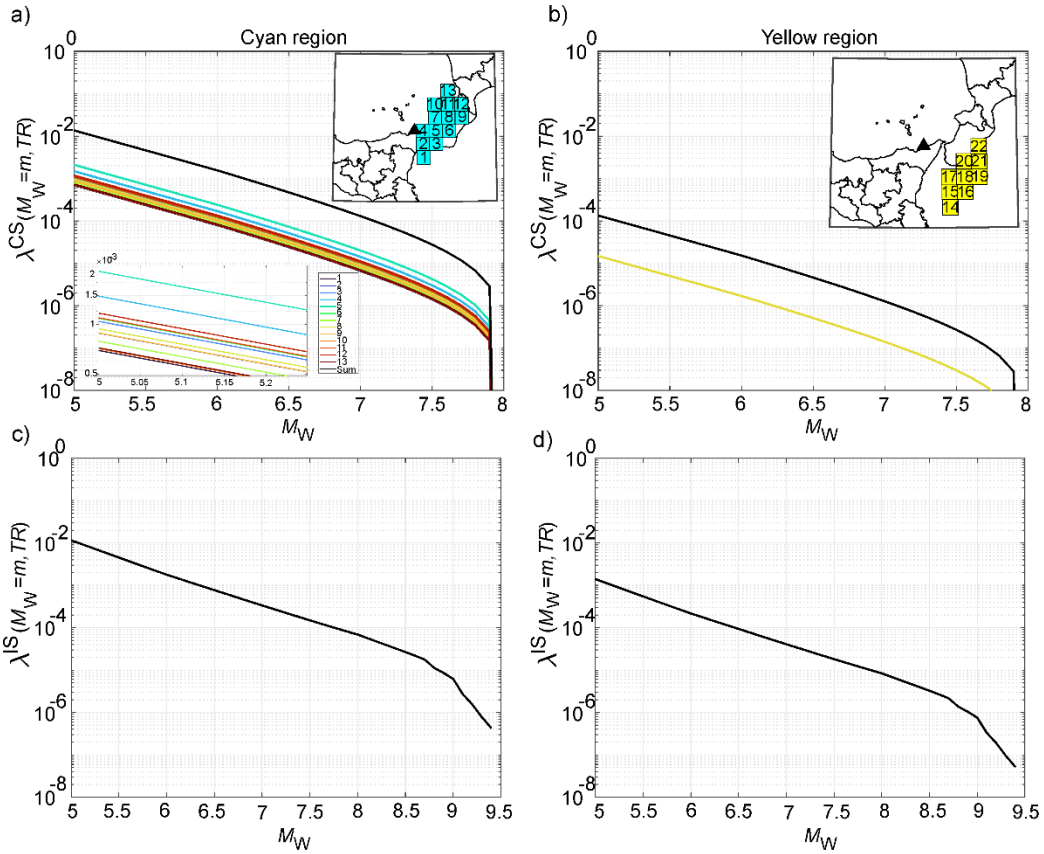

Figure 1.9: Activity rates for crustal seismicity for a) cyan region and b) yellow region. Activity rates for subduction seismicity for c) cyan region and d) yellow region.

To have an overall view of the rates of occurrence of whole area of interest for the *PSHA*. Figure 1.10-a) illustrates the magnitude-frequency plot for all tectonic regions for both CS and IS classes. The colours in figure correspond to the colour used to represent the tectonic regions of Figure 1.3. The figure shows that the crustal tectonic region with the greatest rate of occurrence at varying of magnitude is the Northern Africa region (red line), while the lowest curves are blue and yellow, corresponding to Tyrrhenian Sea (stable oceanic) region and Calabrian Arc region, respectively. Almost all curves have a change of slope after $M_w = 7.4$, highlighting the low frequency of events with magnitude greater than of this threshold. Some regions as yellow and cyan region present at

$M_w = 8$ a drop that led to rate values very low. Lasty, the part of the subduction interface of cyan region has the greatest rates of occurrence.

The knowledge of the rates of occurrence permits to obtain the rate of the earthquakes with magnitude M greater than or equal to minimum magnitude m_{min}, $\nu = \lambda(M_w \geq m_{min}, Reg)$, which is needed to *PSHA*. Figure 1.10-b) shows curves built on the base of curves of panel a), using a data fit model. The slope of these curves is another important parameter for *PSHA*, used, in particular, for the determination of the probability density function of the magnitude. Different alternative models can be used for fitting the activity rates derived from earthquake catalogues, but for the aims of this study, the Gutenberg-Richter relationship is chosen. Eq.(1.5) shows the linear relationship between magnitude and logarithm to the base 10 of the number of the earthquakes per year with magnitude greater than or equal to a particular value:

$$\log_{10}\left[\lambda\left(M_w \geq m \mid \mathrm{Reg}\right)\right] = \log_{10}\left[\lambda\left(M_w \geq m_{\min} \mid \mathrm{Reg}\right)\right] - b \cdot \left(m - m_{\min}\right) \quad (1.5)$$

In this expression, the slope of the curves is indicated with b value. In the figure, the lines are truncated up to maximum magnitude allowed for the tectonic region, thus, up to 8 for crustal regions and up to 9.4 for subduction regions. In figure, the subduction zones are depicted with dotted lines.

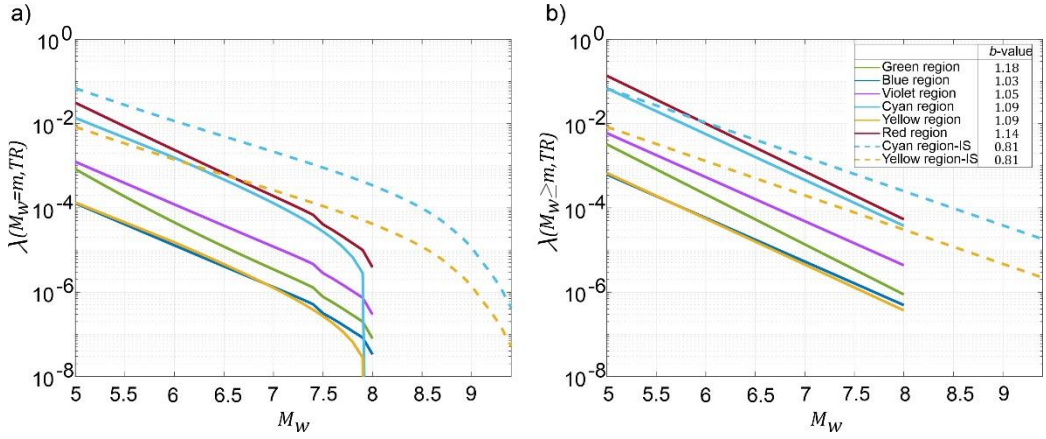

Figure 1.10: a) Activity rates of seismic zones. b) Gutenberg-Richter relationships.

1.1.4 Ground motion prediction equation for subduction zone.

The chosen ground motion prediction model for subduction zone of Calabrian Arc is Abrahamson et al. (2016) [34]. This model is developed with a global dataset of earthquakes in subduction zones. Applicability of this model to this case study was derived from work of Beauval et al. (2012) [35]. Beauval et al. (2012) compare different ground motion prediction models, based on both regional and global datasets, to identify which model provides the best fit to earthquakes that happen on the subduction zone with magnitude greater than or equal to 6. For the different subduction regions tested, as Japan, Taiwan and Greece, it was demonstrated that Abrahamson et al. (2016) is the model that in all cases provides best fit to interface datasets. The functional form of the model for interface subduction events is given by Eq. (1.6) and returns the median value of a pseudo-spectral acceleration.

In the following, the values of parameters of functional form are defined considering the data of case study. Thus, to the aim to evaluate the seismic hazard at Milazzo, the functional form is expressed in terms of *PGA*.

$$\ln(PGA) = \theta_1 + \theta_4 \cdot \Delta C_1 + \left[\theta_2 + \theta_3 \cdot (M_w - 7.8)\right] \cdot \ln\left(R_{rup} + C_4 \cdot e^{\theta_9 \cdot (M-6)}\right) + \\ + \theta_6 \cdot R_{rup} + f_{mag}(M_w) + f_{FABA}(R_{rup}) + f_{SITE}(PGA_{1000}, V_{S30}) \tag{1.6}$$

Where ln is the natural logarithm, $PGA$is the spectral acceleration in units of g, R_{rup} is the closest distance to the rupture area, V_{S30} is the shear wave velocity in the uppermost $30\ m$ of soil column, PGA_{1000} is the median PGA value evaluated with Eq. (1.6) considering $V_{S30} = 1000\ m/s$. The model for magnitude scaling is given by Eq. (1.7):

$$f_{mag}(M_w) = \begin{cases} \theta_4 \cdot \left[M_w - (7.8 + \Delta C_1)\right] + \theta_{13} \cdot (10 - M_w)^2 & \text{for } M_w \le 7.8 + \Delta C_1 \\ \theta_5 \cdot \left[M_w - (7.8 + \Delta C_1)\right] + \theta_{13} \cdot (10 - M_w)^2 & \text{for } M_w > 7.8 + \Delta C_1 \end{cases} \tag{1.7}$$

Where ΔC_1 represents the epistemic uncertainty and depends on the period (T). The epistemic uncertainty is not taken into account herein and

the ΔC_1 assumes value equal to 0.2 for $T = 0s$ corresponding to PGA. $f_{FABA}(R_{rup})$ is the model for forearc or backarc scaling. For Milazzo, $f_{FABA}(R_{rup})$ is given by Eq. (1.8) considering the backarc site.

$$f_{FABA}\left(R_{rup}\right) = \theta_{15} + \theta_{16} \cdot \ln\left[\frac{\max\left(R_{rup}, 100\right)}{40}\right] \tag{1.8}$$

Finally, the model for site response scaling is given by Eq.(1.9):

$$f_{site}\left(PGA_{1000}, V_{S30}\right) = \begin{cases} \theta_{12} \cdot \ln\left(\frac{V_S^*}{V_{lin}}\right) - b \cdot \ln\left(PGA_{1000} + c\right) + b \cdot \ln\left[PGA_{1000} + c \cdot \left(\frac{V_S^*}{V_{lin}}\right)^n\right] & \text{for } V_{S30} < V_{lin} \\ \theta_{12} \cdot \ln\left(\frac{V_S^*}{V_{lin}}\right) + b \cdot n \cdot \ln\left(\frac{V_S^*}{V_{lin}}\right) & \text{for } V_{S30} \geq V_{lin} \end{cases} \tag{1.9}$$

Where V_S^* is given by Eq. (1.10):

$$V_S^* = V_{S30} \quad \text{for } V_{S30} \leq 1000\, m/s \tag{1.10}$$

The near-surface ground condition for Milazzo is assumed as a deep deposit of medium dense sand with $V_{S30} = 270\ m/s$. While there are parameters that are independent from the period and are shown in Table 1.4:

Table 1.4: Period-independent subduction model coefficients [34]**.**

Coefficient	Value over all periods
n	1.18
b	1.88
θ_3	0.1
θ_4	0.9
θ_5	0
θ_9	0.4
C_4	10

And other parameters period-dependent, that for PGA value are reported in Table 1.5.

Table 1.5: Coefficients for median *PGA* (units of g) subduction GMPE model [34]**.**

***T* [s]**	***θ₁***	***θ₂***	***θ₆***	***θ₁₂***	***θ₁₃***	***θ₁₅***	***θ₁₆***	***V*$_{lin}$ [m/s]**	***b***
0	4.2203	-1.35	-0.0012	0.98	-0.0135	0.9996	-1	865.1	-1.186

Figure 1.11 shows an example some results derived from *GMPE* model for the site of interest located in backarc region with $V_{S30} = 270\ m/s$. Panel a) shows *PGA* value with the distance R_{rup}, panels b) and c) the pseudo-acceleration spectra for two distances, $50\ km$ and $200\ km$ respectively, considering, in all panels, three M_w of 7, 8 and 9.

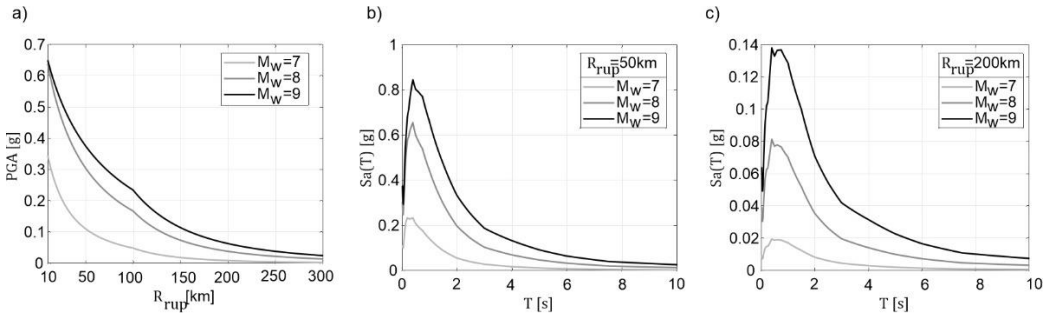

Figure 1.11: a) Attenuation of the *PGA* with the R_{rup}. Median spectra for interface earthquakes at b) $R_{rup} = 50km$ and c) $R_{rup} = 200km$.

Panel a) shows the attenuation of *PGA* values with distance of site from the closest point of rupture plane. M_w of 7 and 8 have *PGA* values almost equal to $0.65\ g$, while for $M_w = 6$, a *PGA* value of about $0.35\ g$ is read. The *PGA* values is under $0.1\ g$ for distances greater than $200\ km$ for all magnitude considered. For distances of greater than $300\ km$ the *PGA* values tend to 0.

The *GMPE* model of Abrahamson et al. (2016) [34] uses as site-source distance, the closest distance of the site to rupture plane R_{rup}. This quantity cannot be evaluated for the subduction source model used for the hazard assessment, because the ruptures are not modelled. Thus, hypocentral distance R_{hyp} is chosen as source-site distance providing approximations of hazard results.

1.2 Probabilistic seismic hazard analysis

Probabilistic seismic hazard analysis is performed to evaluate the number of earthquakes that in one year have cause exceedance of certain ground motion intensity measure threshold. Such number is also called rate of exceedance and obtained via the so-called hazard integral [36]. The results of hazard analysis are usually provided in terms of hazard curves, which associate different threshold values to the exceedance rate with the exceedance rate. In general, the *PSHA* is based on five steps [37]:

1- Identification of seismic sources and selection of an intensity measure.

2- Characterization of the seismicity parameters (magnitudes and rate of earthquakes) for each source.

3- Characterization of all rupture scenarios for identifying the source-to-site distances.

4- Selection of a *GMPE*.

5- Combination of uncertainties on earthquake magnitude, location, and ground motion intensity, using the total probability theorem.

For this case study, the *PGA* is chosen as seismic intensity measure of interest, while the definition of the rate of occurrence on the sources was addressed previously. In addition, the occurrence of earthquakes in time is assumed to follow a homogeneous Poisson process [19] and, for this reason, the seismic hazard at the site of interest can be written as the sum of the rates of exceedance pertaining to the two seismicity classes, that is Eq.(1.11):

$$\lambda_{pga} = \lambda_{pga}^{CS} + \lambda_{pga}^{IS} \tag{1.11}$$

Where λ_{pga}^{CS} is the exceedance rate for CS and λ_{pga}^{IS} is the exceedance rate for IS.

1.2.1 Methodology

The exceedance rate for crustal earthquakes is expressed by Eq.(1.12):

$$\lambda_{pga}^{CS} = \sum_{k=1}^{n_{zones}} \nu_k^{CS} \cdot P\left[PGA > pga\right] \tag{1.12}$$

The exceedance rate for CS is the sum of the exceedance rates of all seismic zones (n_{zones}). $\nu_k^{CS} = \lambda(M_w \geq m, Reg)$ is the rate of earthquakes with $M_w \geq m_{min}$ considering only the contribution of CS for all zones and $P[PGA > pga]$ is the probability that *PGA* threshold is exceeded at the site in one generic (that is, with unknown features) event. To evaluate this probability, it needs to consider the seismic source model adopted that in this case, is the rupture of the faults. The rupture can be seen as a container that enclose information on the earthquake-rupture scenario [38]. For the finite fault geometry model, the information that concerns the rupture are the extension, the orientation, and fault movement. These features allow the characterization of the ruptures. The identification of the fault permits easily to define the magnitude and the source-site distance that enter in the *GMPE*. Lasty, the Eq.(1.12) can be expressed taking into consideration the source model through the Eq.(1.13):

$$\lambda_{pga}^{CS} = \\ = \sum_{k=1}^{n_{zones}} \nu_k^{CS} \cdot \int_{R_{JB}} \int_{M_w} \int_{\boldsymbol{\Theta}} P\left[\left(PGA > pga\right)_k \mid r_{JB}, m, \boldsymbol{\theta}\right] \cdot f_{\left(R_{JB}|M_w,\boldsymbol{\Theta}\right)_k}\left(r_{JB} \mid m, \boldsymbol{\theta}\right) \cdot f_{\boldsymbol{\Theta},k}(\boldsymbol{\theta}) \cdot f_{M_w,k}(m) \cdot dr_{JB} \cdot dm \cdot d\boldsymbol{\theta} \tag{1.13}$$

in which $\boldsymbol{\theta}$ is the vector of focal mechanism that contains the three angles $strike$, dip, and $rake$; while r_{JB} is the Joyner-Boore distance value, the closest distance of the site from horizontal projection of the fault in surface. $P\left[PGA > pga | r_{JB}, m, \boldsymbol{\theta}\right]$ provided by a *GMPE*, is the probability of exceedance of the threshold *pga* given magnitude, Joyner-Boore distance and the focal mechanism and this probability is obtained through the *GMPE*. $f_{R_{JB}|M_w,\boldsymbol{\Theta}}\left(r_{JB}|m, \boldsymbol{\theta}\right)$ is the conditional probability density function of R_{JB} given M_w and $\boldsymbol{\Theta}$; $f_{\boldsymbol{\Theta}}(\boldsymbol{\theta})$ and $f_{M_w}(m)$ are the marginal *pdf* of focal mechanism and magnitude, respectively. The choice to consider the

Joyner-Boore distance depends on the selected *GMPE* that in this case is that of Akkar and Bommer (2010) [39].

The evaluation of $f_{R_{JB}|M_w,\boldsymbol{\Theta}}(r_{JB}|m,\boldsymbol{\theta})$ can be done with a model that takes into consideration the variability of the r_{JB} given m and $\boldsymbol{\theta}$. The uncertainty associated with source-to-site distance is linked implicitly to the variability on the extension of the rupture area. In fact, the regression model of Wells & Coppersmith (1994) provides a lognormal distribution of the rupture area for given magnitude and rake angle. But, in this context, the uncertainty on the distances of site to source is neglected because only the median value of the distribution of the rupture areas is considered. Thus, for given magnitude and focal mechanism the distance site-source is completely determined.

The model used for the determination of the *pdf* of the magnitude, $f_{M_w}(m)$, is based on double-truncated exponential distribution, described by Eq.(1.14):

$$f_{M_w}(m) = \frac{\beta \cdot e^{-\beta \cdot (m - m_{\min})}}{1 - e^{-\beta \cdot (m_{\max} - m_{\min})}}, \quad m_{\min} \le m \le m_{\max} \tag{1.14}$$

where $\beta = ln(10) \cdot b$. Lastly, the marginal *pdf* of the focal mechanisms can be treated as a discrete function. In fact, for each seismic zone are individuated 72 combinations of $strike$, dip and $rake$ as discussed in previous paragraph. So, the *pdf* can be approximated with a probability mass function considering 72 vectors $\boldsymbol{\theta}$ for given region, as Eq.(1.15):

$$\int_{\boldsymbol{\Theta}} f_{\boldsymbol{\Theta}}(\boldsymbol{\theta}) \cdot d\boldsymbol{\Theta} \approx \sum_{f=1}^{72} \sum_{l=1}^{8} \sum_{z=1}^{3} P\left[\boldsymbol{\theta}_f \mid FM_l, BF_z\right] \cdot P\left[FM_l\right] \cdot P\left[BF_z\right] \tag{1.15}$$

In the equation, $P[\boldsymbol{\theta}|FM, BF]$ assumes the meaning of probability to observe inside a seismic source, a focal mechanism $\boldsymbol{\theta}$, to a buffer zone BF, evaluated with a model FM; $P[FM]$ is the weight associated with the model.

To make more clear the Eq.(1.15), the Figure 1.12 shows the probability mass functions of focal mechanisms of two seismic zones, one located north-west respect to the site in panel a), and the other one to

south-east in panel b). On the y-axis is depicted the $P[\boldsymbol{\theta}] = \sum_{l=1}^{8}\sum_{z=1}^{3} P[\boldsymbol{\theta}|FM_l, BF_z] \cdot P[FM_l] \cdot P[BF_z]$ that is the probability to observe a given focal mechanism in a seismic zone. In this way, it is possible to investigate the aleatory variability of the focal mechanisms in areas around the site. Panel a) shows that in some zones the fault mechanism is well-known, in fact, in this example a probability of about 50% is associated with the triplet $\boldsymbol{\theta} = (rake = 90°, dip = 30°, strike = 247.5°)$. On the other hand, panel b) shows that also if there is a peak corresponding to about 15% of probability for $\boldsymbol{\theta} = (rake = -90°, dip = 70°, strike = 202.5°)$ but there are other combinations with comparable probability as the case of $\boldsymbol{\theta} = (rake = 0°, dip = 70°, strike = 202.5°)$. But looking at all combinations, the information that comes out, is that it is more probable that the style of fault in this zone could be normal rather than strike-slip.

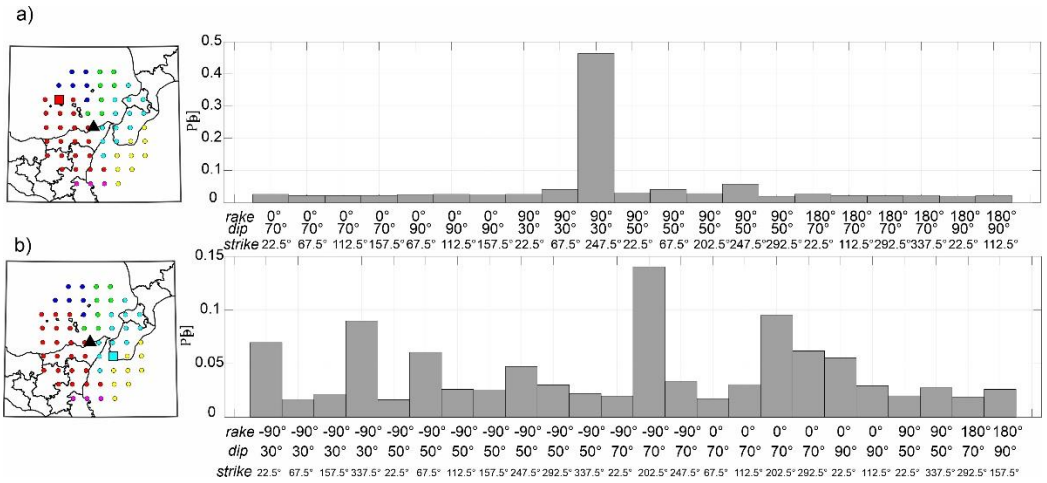

Figure 1.12: Probability mass function of focal mechanism for a) seismic source at north-west and b) seismic source south-east respect to the site.

On the side of interface seismicity, the exceedance rate can be determined through the Eq.(1.16) as:

$$\lambda_{pga}^{IS} = \\ = \sum_{k=1}^{2} v_k^{IS} \cdot \int_{R_{hyp}} \int_{M_w} P\left[\left(PGA > pga\right)_k \mid r_{hyp}, m\right] \cdot f_{R_{hyp},k}\left(r_{hyp}\right) \cdot f_{M_w,k}\left(m\right) \cdot dr_{hyp} \cdot dm \tag{1.16}$$

Where $k = 1$ is referred to the cyan region and $k = 2$ to yellow region, that are the only two tectonic regions that contain the subduction fault.ν_k^{IS} is the corresponding rate of earthquakes with $M_w > m_{min}$. The double integral on the hypocentral distances R_{hyp} and the magnitudes M_w, concerns the product of the exceedance probability of the threshold *pga* conditioned a certain hypocentral distance r_{hyp} and magnitude m, $P[PGA > pga|r_{hyp}, m]$, and the product of marginal *pdf* of hypocentral distance $f_{R_{hyp}}(r_{hyp})$ and magnitude $f_{M_w}(m)$. $P[PGA > pga|r_{hyp}, m]$ derives from a ground motion model, that in this case is Abrahamson et al. (2016) [34]. Such model considers as source-site distance the distance of the site to the shortest point of the rupture surface. However, the ruptures are not conceived in the source model of the subduction. Only the hypocentral distances are allowed, and this is a limit of the source model. $f_{M_w}(m)$ is evaluated, also in this case, with doubled truncated exponential distribution, but the difference with CS is that the interval of magnitude is from 5 to 9.4. Lastly, $f_{R_{hyp}}(r_{hyp})$ is distributed as uniform random variable.

1.2.2 Hazard Results

The results of the *PSHA* are given in panel a) of Figure 1.13, where the black curve is that accounting for all contributions, while those in dark grey and light grey represent the contribution of the crustal and subduction interface hazard, respectively. The intercept to the ordinate of the overall hazard curve corresponds to the rate of earthquakes with $PGA \geq 0.01g$ and is equal to $\lambda(PGA > 0.01g) = 0.18\, yr^{-1}$, which is comparable to that found considering only CS, being it $\lambda^{CS}(PGA > 0.01g) = 0.17\, yr^{-1}$ while, the contribution for IS is $\lambda^{IS}(PGA > 0.01g) = 0.01\, yr^{-1}$, an order of magnitude less than CS. Conversely, looking at $PGA \geq 0.4\, g$, the IS hazard curve returns exceedance rate values larger than CS, that is, the seismic hazard is governed by IS seismicity for high levels of *PGA*. Since the contribution of CS is more influential rather than IS, the hazard for CS is compared with *GMPE* of Bindi et al. (2011) [40], calibrated with a dataset of earthquakes occurred only in Italy, while the Akkar and Bommer (2010) GMPE [39] is referred to earthquakes in Europe and Middle East. The

comparison is allowed because both *GMPEs* predict the geometric mean of the horizontal components of pseudo-spectral accelerations. Panel b) of Figure 1.13 shows that Bindi et al. (2011) [40] underestimates the hazard for $PGA \leq 1.5\ g$.

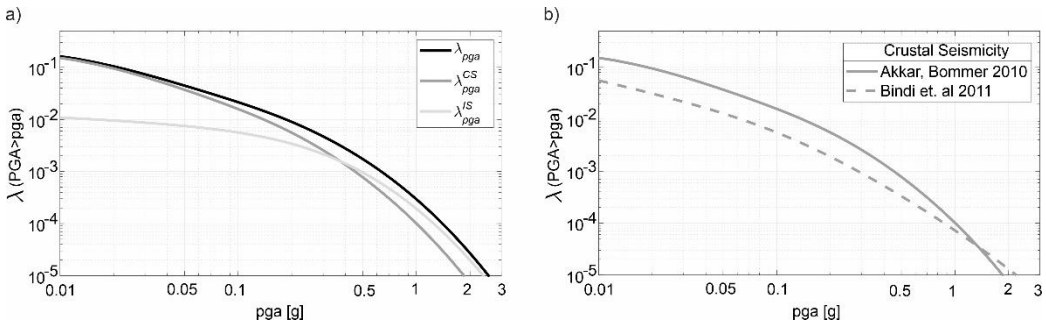

Figure 1.13: a) Seismic hazard curves. b) Comparison between crustal hazard curves considering two different *GMPE*.

1.2.3 Verification

For the aims of this thesis, the results of hazard analysis are reported herein only in terms of *PGA*, but for sake of completeness, the hazard at the site of interest is evaluated also considering some pseudo-spectral accelerations *Sa(T)*. As a result, Figure 1.14-b) shows the uniform hazard spectrum (*UHS*) with exceedance return period (Tr) equal to $Tr = 475\ yr$. In this figure, the *UHS* from analysis is depicted with the black continuous line and is compared with the (elastic) spectrum that the Italian Code or NTC18 [41] provides for structural design, indicated with dashed line. The comparison shows that the spectrum from NTC18 always underestimates the *Sa(T)* for all *T*, presenting a *PGA* value of about $0.2\ g$ against $0.4\ g$ of *UHS* from analysis, and a peak of $0.4\ g$ against $0.9\ g$ respectively; instead, the differences between two spectrums become less significant with $T > 1.5\ s$. The high *Sa(T)* values of *UHS* from analysis depend mainly on part regarding to crustal seismicity, in fact decomposing the *USH* for seismicity class, as done in figure, it is appreciable that for $0\ s < T < 1.5\ s$ the pseudo-spectral accelerations of *CS* represent about 80% of the overall one. In addition, the pseudo-spectral accelerations seem, for *IS*, to be quite similar to those ones of the *UHS* from NTC18.

Before reaching the results showed in previous section, some *PSHA* under simplified assumptions were performed for testing the definitive results. The verification process is focused only on the part of crustal seismicity, because the adopted source model contains a lot of uncertainties. The goal of the verifications is to ensure the absence of programmatic errors in the implemented codes. The verification strategy is to start to easy source models and then to complicate the models, adding uncertainties. The results discussed in the previous section are compared to those provided by dedicated software. A first simplified analysis does not model the finite fault but assumes that the seismic source is represented only by a point that corresponds to the epicentre of the earthquake. This hazard analysis uses the same *GMPE* of final model, that is [39]. The assumption of point source permits to calculate only the epicentral distance, while the model of Akkar and Bommer (2010) [39] considers only the Joyner-Boore distance. For this reason, the conversion relationship of Montaldo et al. (2005) [42] is used for converting the epicentral distance in Joyner-Boore distance. The hazard curve obtained with Matlab code algorithm was compared with the hazard curve derived from REASSESS software [43] and is reported as light grey line in Figure 1.14-a). A second source model used for verification consists in modelling the finite fault geometry considering as focal mechanism the mode of the probability mass function of each seismic zone. Also in this case, the hazard curve was obtained via Matlab code algorithm and compared with the results from the OpenQuake software [44]. The result is the grey line in panel b). The figure shows the curves evaluated with Matlab codes.

The curves derived from verifications are compared with the final hazard curve, which is the black line in panel a). This comparison becomes more explanatory in panel c) where the percentage ratio between the exceedance rates of one of two simplified analysis, λ^*, and λ_{pga}^{CS} is evaluated. Panel c) provides the information that final hazard curve returns rates that are in the middle between the two simplified analysis, in particular the assumption of point sources underestimates the hazard, vice versa the mode of the focal mechanisms overestimates the hazard to the site. In quantitative terms, the ratio maintains under of 20% for values of $PGA < 0.2\ g$ for point sources and $PGA < 0.7\ g$ for the mode of focal mechanisms; instead, both ratios reach about of 60% for $PGA = 3\ g$. In this last case, the 60% indicates that $\lambda^* = (1 \pm 0.6) \cdot \lambda_{pga}^{CS}$.

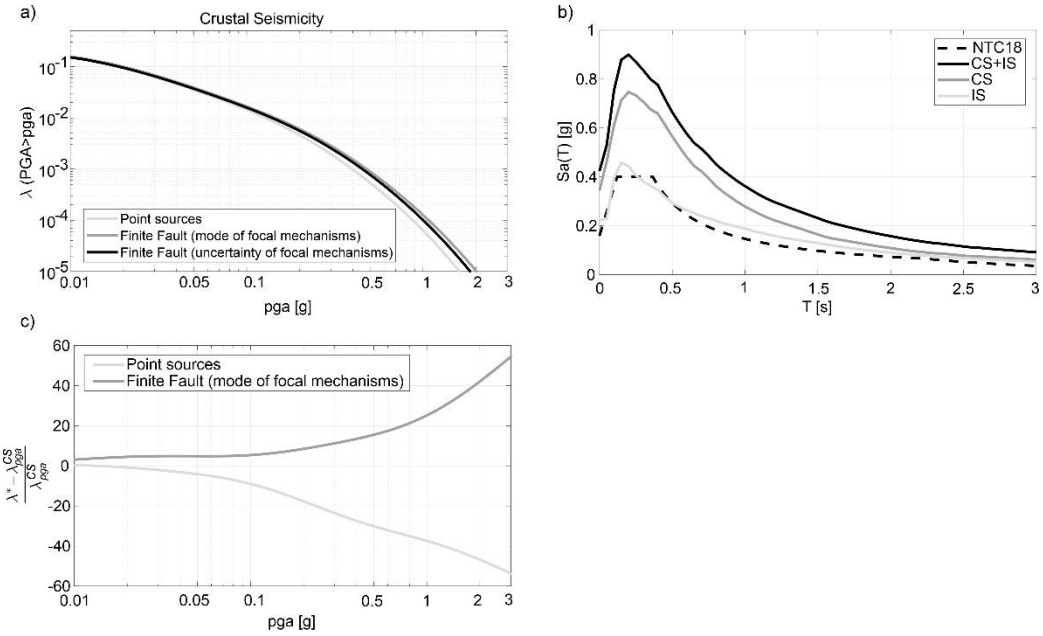

Figure 1.14: a) Comparison between hazard curves obtained with different crustal seismicity source models. b) Uniform hazard spectra. c) Percentage ratio of hazard curves of panel a).

1.3 Available probabilistic tsunami hazard analysis results

This paragraph describes, briefly, the general procedure for probabilistic tsunami hazard analysis based on site-specific inundation scenarios. The objective of the paragraph is to have a general overview of *PTHA* data available for performing conditional tsunami hazard analysis, that will be discussed in Paragraph 1.4. *PTHA* was already developed for the site of Milazzo by Volpe et al. (2019) [20]. In the following, the main input data and results are recalled, which are available thanks to a collaboration between University of Naples, Federico II, and the group of INGV of Rome.

The general *PTHA* procedure can be summarized in four steps. Step (1) is focused on the definition of the seismic sources triggering the tsunami inundation scenarios. Step (2) provides the propagation tsunami scenarios for each individual seismic source of step (1) up to a given offshore isobath. Step (3) relies on a filtering procedure for selecting a subset of relevant scenarios to reduce computational effort preserving, however, the accuracy of the results. Lastly, in step (4), the hazard curves are computed as the result of an ensemble modelling, which is considering both aleatory and epistemic uncertainties. The step (1) was described in section 1.1, regarding the seismic sources, and in section 1.2, dealing with aleatory variability and the epistemic uncertainty of sources. For step (2), offshore tsunami amplitude triggered by the seismic sources of step (1) are evaluated on 11 offshore points along the coast of the Milazzo on the 50 m isobath. Actually, to save computational time, propagation scenarios from step (1) are not individually simulated but are obtained by linear combination of pre-calculated tsunami waveforms produced by Gaussian-shaped unitary sources [45]. In step (3), a filtering procedure is developed to reduce the number of scenarios to consider in the analysis. The filters consist in removing scenarios with offshore tsunami amplitude and occurrence probability below a certain threshold. This filtering procedure allows one to treat separately the far- and near- field scenarios, applying different thresholds for two cases. Inundation simulations from step (3) are performed with the Tsunami-HySEA code, exploiting the nested grid algorithm. The results of the step (3) are time histories of tsunami height

and velocity at each point of a high-resolution grid that covers both on- and off-shore points. At step (4), the time histories are used for obtaining the hazard curves or inundation maps that define the tsunami hazard at site of interest.

1.3.1 Tsunami intensity measures definitions

Tsunami intensity measures used for describing the propagation tsunami model for PTHA and the tsunami fragility functions are the offshore tsunami amplitude, the inundation depth, the flow velocity, and the momentum flux. These quantities are defined in ASCE7-16 [46] and are also briefly introduced in this section.

Offshore tsunami amplitude and inundation depth are depicted in Figure 1.15. The offshore tsunami amplitude is the maximum considered tsunami amplitude relative to the reference sea level, measured where the undisturbed water depth is 100 m; while, the inundation depth is the depth of tsunami water level, including relative sea level change, with respect to the grade plane at the structure. In this thesis, the term tsunami height h_w, is used interchangeably to indicate both of these terms, that is, representing offshore tsunami amplitude when dealing with tsunami height on offshore points, or inundation depth when dealing with inland locations.

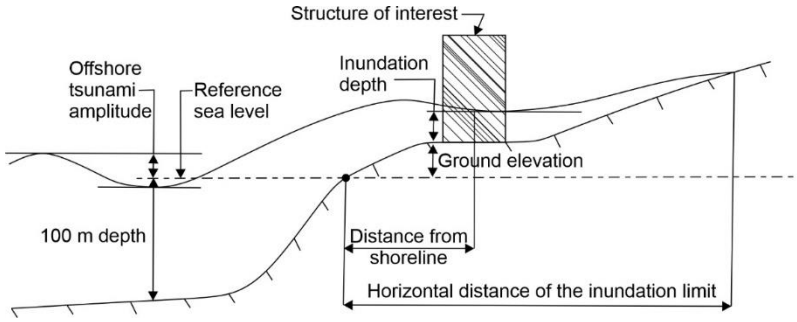

Figure 1.15: Illustration of the tsunami parameters [46]**.**

The others selected intensity measures are the tsunami velocity v_w, that is the flow velocity at the location of the point considered, and the momentum flux, mf, that is a measure of the energy of flux per unit of area

[46], but, herein, is normalized to the density of the sea water, ρ_w, and defined by the Eq. (1.17):

$$mf = h_w \cdot v_w^2 \tag{1.17}$$

1.3.2 Propagation tsunami modelling

The objective of this section is to analyse the time histories of tsunami height and velocity from the study of Volpe et al. (2019) [20] coming from tsunami propagation scenarios. Tsunami propagation scenarios are obtained though simulations of wave propagation triggered by seismic sources. In this case study, each seismic source of Figure 1.2 triggers several tsunami propagation scenarios for a total number of $1'701'341$. Between all these simulations, only 1154 pass the filter procedure and, thus, are analysed for the tsunami hazard assessment. In detail, there are 613 far-field and 464 near-field wave propagation scenarios for crustal sources; while for the subduction zone of Calabrian Arc, there are 13 simulations far-field and 56 near-field; lastly, 8 far-field scenarios from the subduction zone of Hellenic Arc can be found. Each scenario produces a time history of tsunami height and velocity of $8\,h$ (hours) on $56'000$ points of the refined grid with resolution of 0.00625 arcmin (about $11\,m$), that covers the entire area of the petrochemical plant of Milazzo. Figure 1.16 shows the domain of this grid used for tsunami simulations.

More specifically, the time histories of the tsunami height are corrected for a coseismic coastal displacement value [20], that is the vertical displacement of the seafloor due to seismic event. The value of the coseismic displacement can be both positive and negative, indicating the coastal uplift or subsidence, respectively. Figure 1.17 shows an example of a time history of the tsunami height with and without the coseismic displacement.

Figure 1.16: Domain of the grid used for tsunami simulations.

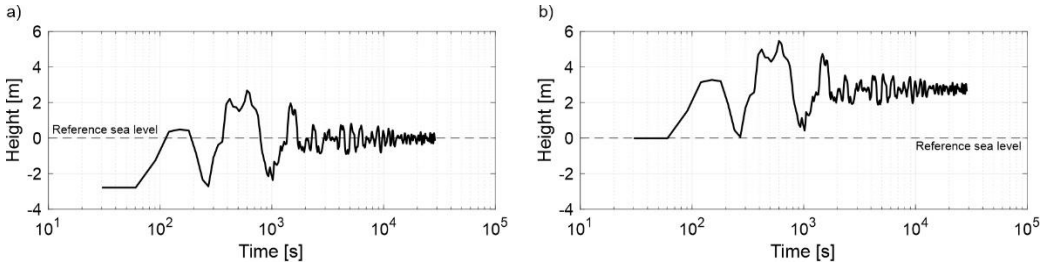

Figure 1.17: Time history of the tsunami height a) with coseismic displacement, and b) without coseismic displacement.

Saving such a number of time histories is computationally demanding and, therefore, only the maximum height ($h_{w,max}$) and the maximum momentum flux (mf_{max}) of time histories are stored for each point of the refined grid. The maximum momentum flux is equal to $mf_{max} = (h_w \cdot v_w^2)_{max}$, that it is different from the product of $h_{w,max}$ and of the square of maximum tsunami velocity $v_{w,max}^2$, because these two physical quantities may not occur at the same time instances. The momentum flux is derived, thus, from the time-histories of height and velocity.

Some time-histories of tsunami height and velocity are, however, saved only for 95 inland points located strategically at the edges of the storage tanks, for a total of $109{,}630$ histories. Some of these simulations

show wave height constant during all time history and for this reason are removed from the analysis because imply that there has been no wave propagation. At the end, the number of simulations analysed is $55{,}686$. Figure 1.18-a) shows the 95 control points in which the simulations are saved. Observed coseismic values for near-field scenarios are about three meters of subsidence for earthquakes of moment magnitude of about 7.

From this database, a subset of three simulations is extracted to show the non-contemporaneity of the maximum momentum flux and the maximum height, and to give an order of magnitude of the maximum values of height, velocity and momentum flux simulated for this case study. Three selected time-histories are those ones containing the highest recorded tsunami height (panel b), the highest recorded momentum flux (panel c) and that with highest recorded tsunami velocity (panel d). In panel b), the highest height recorded is equal to $6.9\ m$; the velocity at this time instances $v_w(h_{w,max})$ is $1.5\ m/s$ while the maximum velocity $v_{w,max}$ of all this simulation is $3.4\ m/s$, corresponding to a tsunami height equal to $0.2\ m$; lastly, the maximum momentum flux of this simulation is equal to $15.4\ m^3/s^2$. The maximum momentum flux is recorded $70\ s$ before the maximum height and 30 s after the maximum velocity, corresponding to an intermediate time instance between maximum height and maximum velocity. Conversely, in panel d), the maximum tsunami velocity recorded among all scenario simulations is equal to $6.5\ m/s$ and in this case, the maximum velocity occurs at the same time instance of the maximum momentum flux recorded during all the same time history. On the other hand, the maximum height of this record is equal to $4.13\ m$ and occurs at velocity of $0.25\ m/s$, after the peak of velocity. In panel a) and d), it is evident that the maximum height and the maximum velocity do not happen contemporary, in particular, great velocities correspond at low heights and vice versa. The maximum value of the momentum flux or equivalently the energy recorded for all simulations is about $90\ m^3/s^2$.

These three tsunami intensity measures give an indication about the tsunami pressures acting on the tanks, because the tsunami height is proportional to the tsunami hydrostatic pressure component, P_{ws}, the velocity to the tsunami hydrodynamic pressure component, P_{wd}; and the momentum flux is proportional to the hydrodynamic pressure resultant. P_{ws} is a triangular load that varies linearly with the tsunami heigh with

maximum value at the base of the tank and P_{wd} is a uniform load along the height. Eq.(1.18) shows how to evaluate two tsunami pressure components:

$$\begin{cases} P_{ws}(Z) = \rho_w \cdot g \cdot (h_w - Z) \\ P_{wd} = \frac{1}{2} \cdot C_d \cdot \rho_w \cdot v_w^2 \end{cases} \quad (1.18)$$

Where ρ_w is the sea water density equal to 1.2 t/m^3, g is the gravity acceleration and C_d is the hydrodynamic coefficient depending on the shape of the structure [46]. Z can assume values between 0 m and h_w, with the $Z = 0\ m$ on the ground level. The values of two tsunami pressure components are labelled on the right y-axis of panels b) and d).

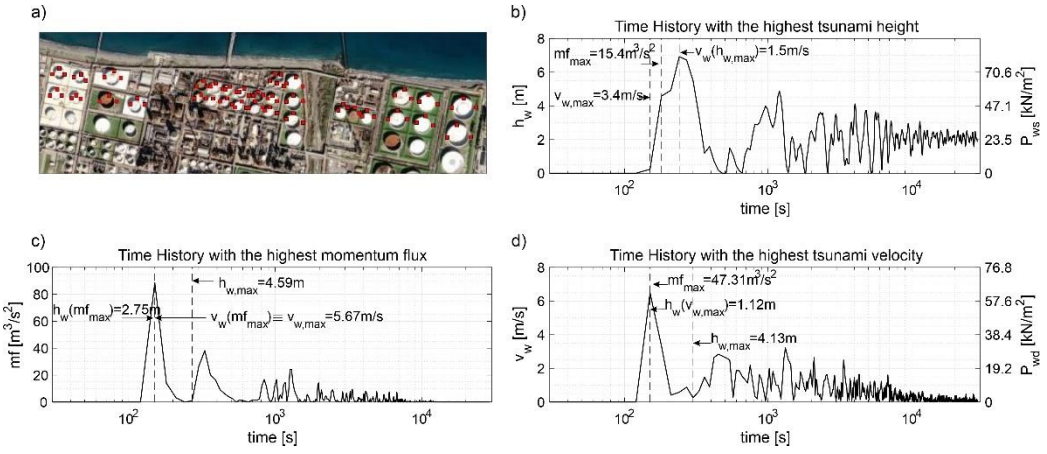

Figure 1.18: a) 95 inland control points in which the simulations are saved. Time histories in which is recorded: b) the highest tsunami height; c) the highest momentum flux; and d) the highest tsunami velocity.

1.3.3 Hazard results

The results of a *PTHA* are the hazard curves that give the exceedance rates, intended as number of tsunami events that on average in one year cause at the site of interest the exceedance of a certain threshold of tsunami intensity measure, varying the threshold. The selected intensity measure for this hazard analysis is the maximum

tsunami height $H_{w,max}$, with a corresponding threshold value indicated with the symbols $h_{w,max}$. The hazard curves used herein are the mean curves of an ensemble modelling those accounts for both the epistemic uncertainty given from several alternative implementations and the aleatory variability that is contained inside the seismic source models (see paragraph 1.1). Figure 1.19 shows an example the ensemble modelling for 1 point of 95 inland control points (red marker), considering the hazard curves in terms of maximum height. For this point, 100 hazard curves are obtained using 100 alternative models, considering each one equally probable. The value of the exceedance rate, fixed a certain threshold and a model, is evaluated as the sum of the rates of occurrence of seismic sources that trigger an inundation scenario with height greater than the threshold. Thus, the mean value of rate of exceedance is the mean of exceedance rates of all models. Eq. (1.19) summarized in symbols the evaluation of exceedance rate:

$$\lambda\left(H_{w,\max} > h_{w,\max}\right) = \frac{\sum_{j=1}^{n_{\text{models}}} \sum_{i=1}^{n_{\text{sim}}} \left(I_i \cdot \nu_{T,i}\right)_j}{n_{\text{models}}} \tag{1.19}$$

Where $i = 1,2, \dots n_{sim}$ and $j = 1,2, \dots, n_{models}$ are two indexes that run, respectively, on the number of simulations $n_{sim} = 1154$ and the number of models $n_{models} = 100$. ν_T is the rate of occurrence of tsunami on a seismic source and I is an indicator function which assumes the value of 1 if the height of a generic simulation is greater than the threshold and 0 otherwise. In this way, all the seismic sources both far- and near- field are considered for the analysis.

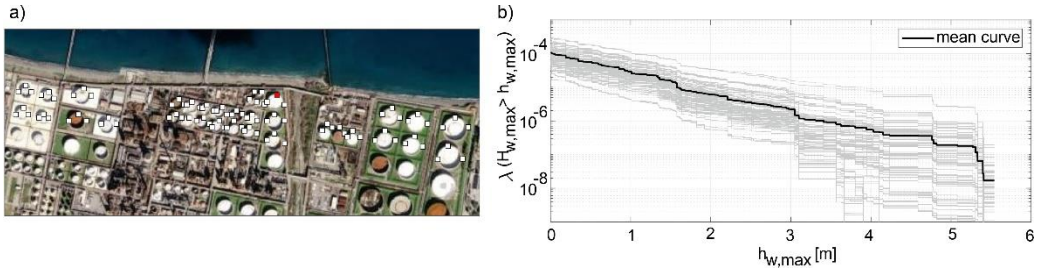

Figure 1.19: a) Inland points in which the simulations are saved. b) Mean tsunami hazard curve between 100 curves obtained with different models.

To have an ensemble view of the hazard of the geographical area of interest, Figure 1.20 shows the hazard maps and the probability maps for the two tsunami intensity measures. More in detail, the hazard maps in panels a) and b) provide the value of the intensity measure with return period $Tr = 200^{\cdot}000\ yr$ corresponding to an exceedance rate of $\lambda\left(H_{w,max} > h_{w,max}\right) = 5 \cdot 10^{-6}\ yr^{-1}$. Panel c) maps the probability that in a reference period, Δt, of $50\ yr$ there is at least a tsunami having maximum height during inundation greater than $2\ m$, while panel d) displays the probability that, in $50\ yr$, at least one tsunami has maximum momentum flux during the inundation greater than $30\ m^3/s^2$. This probability is evaluated assuming that the events occur following a homogeneous Poisson process. In all panels of the figure, there is a black line that represents the shore and three streak lines that are the quays for handling of boats or ships. Panel a) shows that the greatest tsunami heights are recorded near to the coast with value up to $3.5\ m$, while the propagation decreases almost rapidly within a few feet. In panel b), the map highlights an enhanced current vorticity inside the docks. The panel c) shows that the probabilities to exceed a tsunami height of $2\ m$ in $50\ yr$ is the order of $1 \cdot 10^{-3}$ in proximity of quays and between them, while panel d) reveals the exceedance probability of a maximum momentum flux of $30\ m^3/s^2$ in $50\ yr$ is of order of magnitude of 10^{-4} at the sea near the coast and the quays, while for the inland points, near the tanks the probabilities tend to the zero.

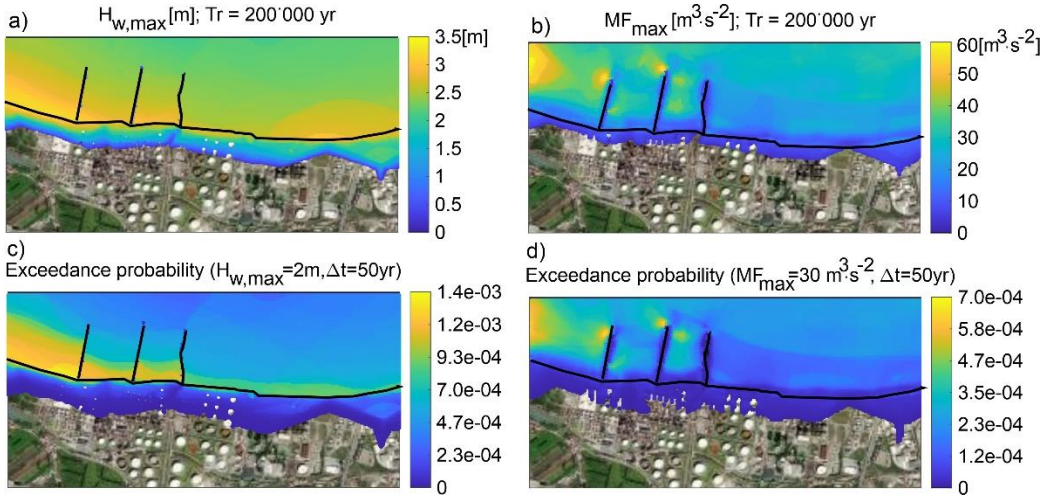

Figure 1.20: Hazard maps: a) for maximum tsunami height; b) for maximum momentum flux. Probability maps: c) for maximum tsunami height; d) for maximum momentum flux (Reproduction of the maps of article of Volpe et al. 2019 [20]**).**

1.4 Models for conditional tsunami hazard

The tsunami hazard at the site of interest can be expressed under different intensity measures. Each intensity measure is representative of different effects on the structures, for instance the tsunami height is a measure of the intensity of the hydrostatic pressure on the storage tanks that leads to elastic buckling of the shell, or the momentum flux is a quantity proportional to the hydrodynamic pressure that can provoke sliding or the overturning of the tank. Thus, the estimation of the structural performance of a tank under tsunami action is a complex phenomenon that depends on the contemporaneity of all actions on the structure. Thus, it seems appropriate to develop conditional hazard, which allows one to derive the distribution of a secondary intensity measure conditional to the occurrence of the primary intensity measure. In more detail, in this paragraph, this concept is expressed in terms of joint probability density function *JPDF* of maximum momentum flux and velocity at the instant of maximum height $\tilde{v} = v_w(h_{w,max})$ conditional on the occurrence of maximum height.

1.4.1 Joint probability density function of momentum flux and velocity given tsunami height.

The objective of this section is to model the joint distribution of the maximum moment flux and the maximum velocity at the maximum height conditional to the maximum height, that is, $f_{MF_{max},\tilde{V}|H_{w,max}}$, which can be obtained from Eq.(1.20):

$$\begin{aligned} & f_{MF_{\max},\tilde{V}|H_{w,\max}}\left(mf_{\max},\tilde{v}\mid h_{w,\max}\right)= \\ & = f_{MF_{\max}|\tilde{V},H_{w,\max}}\left(mf_{\max}\mid\tilde{v},h_{w,\max}\right)\cdot f_{\tilde{V}|H_{w,\max}}\left(\tilde{v}\mid h_{w,\max}\right) \end{aligned} \tag{1.20}$$

Where $f_{MF_{max}|\tilde{V},H_{w,max}}$ is the conditional *pdf* of MF_{max} given $\tilde{v}$ and $h_{w,max}$, while $f_{\tilde{V}|H_{w,max}}$ is the marginal *pdf* of the $\tilde{v}$ conditional to $h_{w,max}$.

Assuming that momentum flux and velocity are jointly lognormal, conditional to $h_{w,max}$, allows one to derive $f_{MF_{max}|\tilde{V},H_{w,max}}$, because it is defined by two parameters, that is, conditional mean $\mu_{ln(mf_{max})|ln(\tilde{v}),h_{w,max}}$ and the standard deviation $\sigma_{ln(mf_{max})|ln(\tilde{v}),h_{w,max}}$, as Eq. (1.21):

$$\begin{cases} \mu_{\ln(mf_{\max})|\ln(\tilde{v}),h_{w,\max}} = \mu_{\ln(mf_{\max})|h_{w,\max}} + \rho \cdot \dfrac{\sigma_{\ln(mf_{\max})|h_{w,\max}}}{\sigma_{\ln(\tilde{v})|h_{w,\max}}} \cdot \left(\ln(\tilde{v}) - \mu_{\ln(\tilde{v})|h_{w,\max}}\right) \\ \sigma_{\ln(mf_{\max})|\ln(\tilde{v}),h_{w,\max}} = \sigma_{\ln(mf_{\max})|h_{w,\max}} \cdot \sqrt{1-\rho^2} \end{cases} \tag{1.21}$$

Where $\mu_{ln(mf_{max})|h_{w,max}}$ and $\sigma_{ln(mf_{max})|h_{w,max}}$ are the mean and the standard deviation of logarithm of the momentum flux given tsunami height; $\mu_{ln(\tilde{v})|h_{w,max}}$ and $\sigma_{ln(\tilde{v})|h_{w,max}}$ are the mean and the standard deviation of $f_{\tilde{V}|H_{w,max}}$; and ρ is the correlation coefficient between the momentum flux and the velocity given by Eq. .

$$\rho = \frac{COV\left(\ln(\tilde{v}_w), \ln(mf_{\max}) \mid h_{w,\max}\right)}{\sigma_{\ln(\tilde{v}_w)|h_{w,\max}} \cdot \sigma_{\ln(mf_{\max})|h_{w,\max}}} \tag{1.22}$$

where the symbol $COV(.)$ indicates the covariance.

These parameters are evaluated through regression analysis. To do so, one should look at Figure 1.21. In panel a) and b), the histograms of the $h_{w,max}$ and $\tilde{v}$ of all tsunami simulations are shown. The heights are collected in bin with width of $0.1\ m$ and more than the 60% of simulations is concentred towards to the heights less than $2\ m$, only few simulations reach peaks of tsunami height up to $7\ m$. For the $\tilde{v}$, instead, the maximum recorded value is $4\ m/s$ but a 80% of the records returns velocity values less than $1\ m/s$. Panel c) shows, instead, the frequency of the simulations for the mf_{max} that varies with bin width of $1\ m^3/s^2$. In this case, more than the 50% of the simulations have mf_{max} in the first bin. The choice to use $\tilde{v}$ and not maximum velocity of the time history is based on the observation that in the tsunami simulations, the maximum velocity is not contemporary to the maximum tsunami height (as discussed in section 1.3.2). Thus, in

the view vulnerability analysis of the tanks, to use the maximum of both intensity measures would result an unlikely scenario.

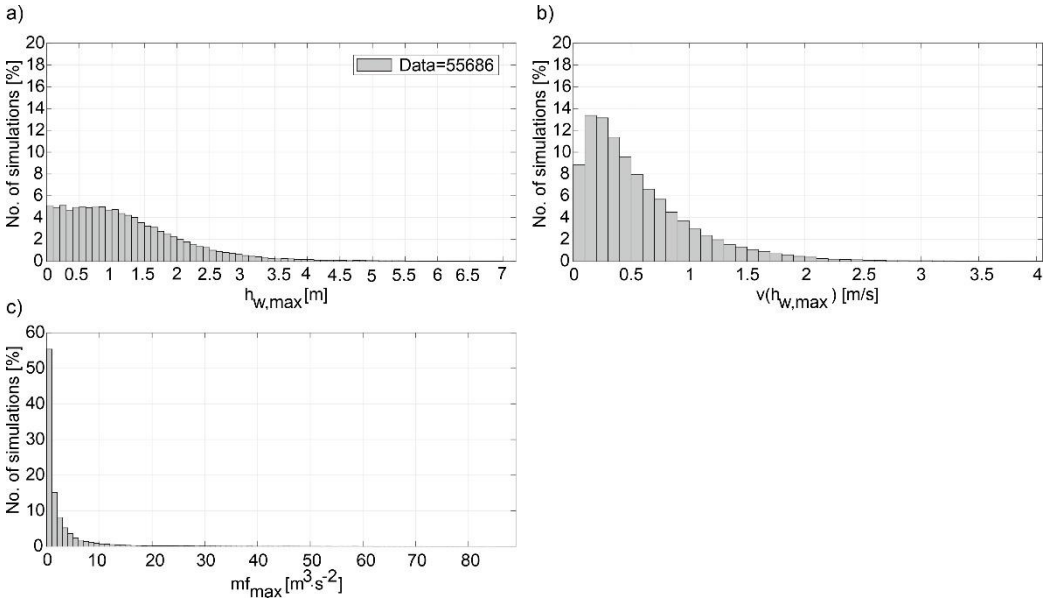

Figure 1.21: a) Histogram of the maximum tsunami height. b) Histogram of velocity at the instant time of maximum tsunami height. c) Histogram of the maximum momentum flux.

From these histograms it is possible to carry out the regression models that allow to derive the conditional mean and the standard deviation needed for computing $f_{MF_{max}|\tilde{V},H_{w,max}}$.

For each bin of Figure 1.21-a), the mean and the standard deviation of the velocity and the momentum flux are evaluated for the simulations that fall inside a given interval of height, and the results are reported in Figure 1.22 in the four panels with the circular markers. In each panel, it is found the best-fitting curve. Focusing on the standard deviations, the data are located on a line enough horizontal, thus with the good approximation, it can be assumed that the standard deviations are constant with the tsunami height, with values: $\sigma_{ln(\tilde{v})|h_{w,max}} = 0.9\ m/s$ and $\sigma_{ln(mf_{max})|h_{w,max}} = 1\,m^3/s^2$.

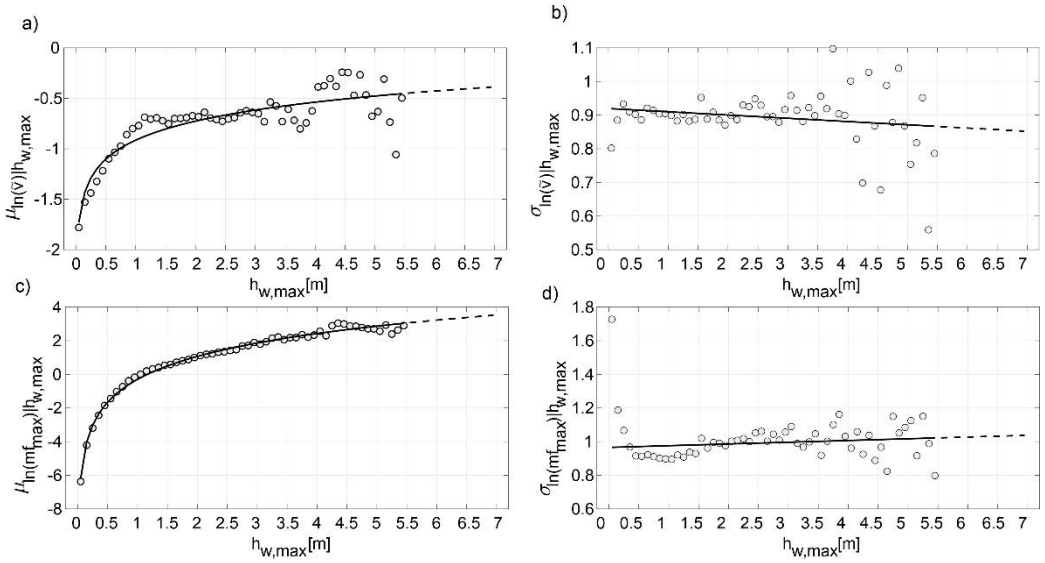

Figure 1.22: a) regression curve of the mean of the logarithm of the velocity at the instant time of the maximum height given a maximum tsunami height value. b) Linear regression curve of the standard deviation of the logarithm of the velocity at the time of maximum height given height value. c) Nonlinear regression curve of the mean of the logarithm of the maximum momentum flux given a height value. d) Linear regression curve of the standard deviation of the logarithm of the maximum momentum flux given height value.

The means are estimated with a non-linear fitting model. These functions are expressed by Eq.(1.23) and (1.24):

$$\mu_{\ln(\tilde{v})|h_{w,\max}} = \alpha_1 \cdot \ln\left(h_{w,\max}\right) + \beta_1 \tag{1.23}$$

$$\mu_{\ln(mf_{\max})|h_{w,\max}} = \alpha_2 \cdot \ln\left(h_{w,\max}\right) + \beta_2 \tag{1.24}$$

where α_1,α_2, β_1, β_2 are the regression coefficients reported in Table 1.6. In Figure 1.22-a) and c), the values on the y-axis are the means of random variables independent and identically distributed with same dispersion. In Figure 1.23-a), a linear fit is applied, instead, to the correlation coefficient, for finding a relationship with maximum tsunami height. The equation is expressed in (1.25):

$$\rho = a \cdot h_{w,\max} + b \tag{1.25}$$

where *a* and *b* are regression coefficients in Table 1.6.

Table 1.6: Regression coefficients.

α_1	α_2	β_1	β_2	a	b
0.2830	1.9613	-0.9084	-0.2644	-0.0618	0.5883

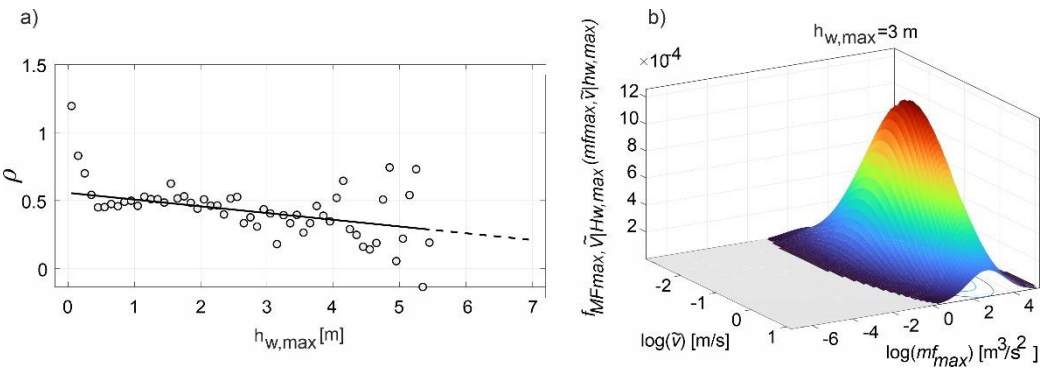

Figure 1.23: a) Linea regression curve of the correlation coefficient between the velocity at the time of tsunami height and the maximum momentum flux, given height value. b) Joint probability density function of the maximum momentum flux and the velocity at the time of the tsunami height, conditional to maximum tsunami height.

Both for Figure 1.22 and Figure 1.23-a), the fitted models are valid for the simulation data of this case study. Lastly, the bivariate Gaussian model on which the conditional hazard model is based, is shown in Figure 1.23-b). Here, an example is depicted considering a threshold height of $3\ m$.

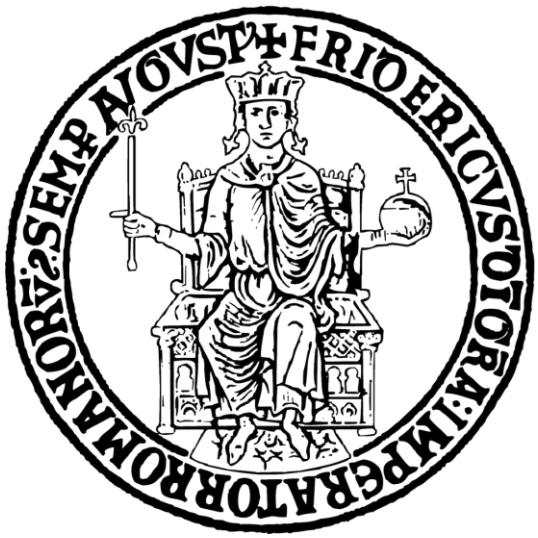
FRIDERICVS DEI GRA ROMANORVM IMPERATOR SEMPER AVGVST

Chapter 2

Tsunami fragility for anchored floating-roof atmospheric tanks.

Courage isn't having the strength to go on. It is going on when you don't have strength.

Napoleone Bonaparte

One of the major issues in *QRA* [47] in the process industry are cases of natural events, such as landslides, hurricanes, tsunami, floods or earthquakes, triggering extensive industrial accidents [48]. The main feature of such accidents is that damage sustained by the industrial equipment (e.g., structural damage to storage tanks or rupture of connecting pipelines) can cause the release of hazardous substances into the environment, that is so-called NaTech events. This loss of containment may cause a series of cascading effects such as chain fires, blasts, and dispersion of toxic clouds, with potential loss of human life [49].

Analytical procedures for NaTech *QRA* require a probabilistic description of hazard at the site of interest, vulnerability models for the industrial components, exposure information and an evaluation of the possible consequences of accident scenarios that could be triggered by NaTech events [47,50]. The focus of this chapter is to evaluate the vulnerability of anchored floating-roof atmospheric storage tanks impacted by tsunami waves. This is motivated considering the incentives for industrial facilities to be located in coastal zones, due to better access to maritime transportation, and the vulnerability of atmospheric storage tanks

against content release following damage to the structure and connections induced from external pressure and drag forces during flood-like events [51–53].

The present study comes in continuation of past works that studied the seismic vulnerability of such tanks [54,55], and aims to cover additional failure mechanisms, levels of tank contents and sources of uncertainty with respect to previous similar works [56]. More specifically, finite element models of various cylindrical storage tanks are developed, in the spirit of past works that dealt with seismic vulnerability via numerical models, [57,58] and are subjected to a simplified representation of tsunami-induced actions, with the objective of deriving fragility functions pertaining to a loss-of-containment limit state. These models consider the response of the anchorage system to tsunami-induced drag and buoyant forces, stresses due to potential loss of contact of the base plate with the foundation and stability issues of the shell walls due to external pressures from inundation.

Another crucial point for the derivation of the fragility curves concerns the performance-based engineering methods for tsunami. The tsunami is a dynamic action, thus, the behaviour, or similarly the performance, of the structure is well-captured if the inundation time-history is applied to it. But dynamic analyses are not always easy to implement. For this reason, existing literature studies (e.g. [59–61]) have developed performance-based engineering methods in which tsunami load is modelled as quasi-static action. In this way, nonlinear static (pushover) analyses have been applied for structures. Such research studies are influenced from ASCE7-16 [46] that distinguishes the tsunami action into the hydrostatic and hydrodynamic component. Particularly important is the modelling of the hydrodynamic force. Foster at al. (2017) [62] have demonstrated that hydrodynamic drag force on the overall structure and individual structural components can be safely modelled as static actions because these forces are typically of long duration. In addition, several authors have focused their studies on pushover analysis for tsunami loading. Macabuag et al. (2014) [63] compare the structural response of a concrete resisting frame under tsunami loadings assessed with different code-based, including the ASCE7-16 [46]. In this work, the tsunami inundation depth is assumed constant, increasing monotonically the flow velocity. This approach is called in literature constant-depth pushover.

Attary et al. (2017) [64] perform pushover analysis using a random set of tsunami inundation depths and flow velocities values using the expressions in FEMA [65]. Starting to these studies, Petrone et al (2017) [59] have developed tsunami fragility curves using two types of structural analysis: the tsunami time-history analysis, and the variable-depth pushover. Time-history analysis is based on the application to the structure of the time-history of the inundation depth and the time-history of the two components of the flow velocity. Variable-depth pushover analysis allows to apply to the structure lateral forces that increase monotonically varying both the inundation depth and flow velocity. More specifically, for each inundation depth level, the corresponding flow velocity is evaluated assuming a constant Froude number. The structural performance is expressed in terms of tsunami base shear versus total drift. The results of this work show that the engineering demand parameters and collapse fragility curves obtained via variable-depth pushover analysis and the time-history analysis are in good accordance. However, the variable-depth pushover analysis presents a particular limitation because the analysis is implemented in load-control and for this reason is not able to capture the degrading portion of the pushover. This limitation is overcome by Baiguera et al. (2019) [61] that implements a variable-depth pushover analysis in displacement control, in which the displacement increases monotonically and at each step of the analysis, the corresponding tsunami force is evaluated. A subsequent study of Baiguera et al. (2021) [60] has applied this methodology to buildings located in zones with high tsunami impact, following the ASCE 7-16 [46] provisions, demonstrating the advantages to adopt the pushover analysis approach for design of these structures.

This chapter is structured with the following steps: the presentation of the chosen methodology; the modelling assumptions for the tsunami-induced loads on the tanks; the structural behaviour and the selected failure mechanisms. Additionally, the geometry and some detailing information of the case-study tanks are reported. Subsequently, the numerical models of these structures are described in some detail, with a focus on sources of non-linear behaviour built into said models. Finally, the results of the analyses and the procedure employed to develop fragility functions from said results are presented. The chapter concludes with a brief discussion of these results and some final remarks.

2.1 Methodology

The present study uses detailed numerical models of three archetypal floating-roof atmospheric storage tanks, together with a simplified representation of tsunami-induced loads on these structures. These tanks have been designed for the purposes of this investigation according to European codes [66–69], with a focus on the thickness of the cylindrical shell, the width and thickness of the annular foundation plate and the anchors. Numerical structural analysis, employing the finite element method, is used to determine if at least one of three possible failure mechanisms can be activated for given tsunami loading and quantity of liquid content present in the tank. The three failure mechanisms considered are buckling of the cylindrical shell wall due to compressive circumferential stresses, induced by the tsunami external pressure overcoming the internal hydrostatic pressure of the vessel, shear failure of the anchors due to lateral hydrodynamic forces exerted by the tsunami and axial tension failure of the anchors due to buoyant forces. These three mechanisms are schematically illustrated in Figure 2.1, where the forces acting on a partially filled tank under tsunami inundation are also shown. It is assumed that activation of any of these failure mechanisms will likely cause leakage due to rupture of connections with piping systems, so that the occurrence of at least one tantamount to reaching a loss-of-contents limit state. The uncertainties in structural properties considered in the fragility derivation include the axial and shear resistance of the anchors, and the level of geometric fabrication imperfections of the tank shell that drives stability. Uncertainty in the tsunami-induced equivalent static loads is also taken into account, as will be elaborated in the following.

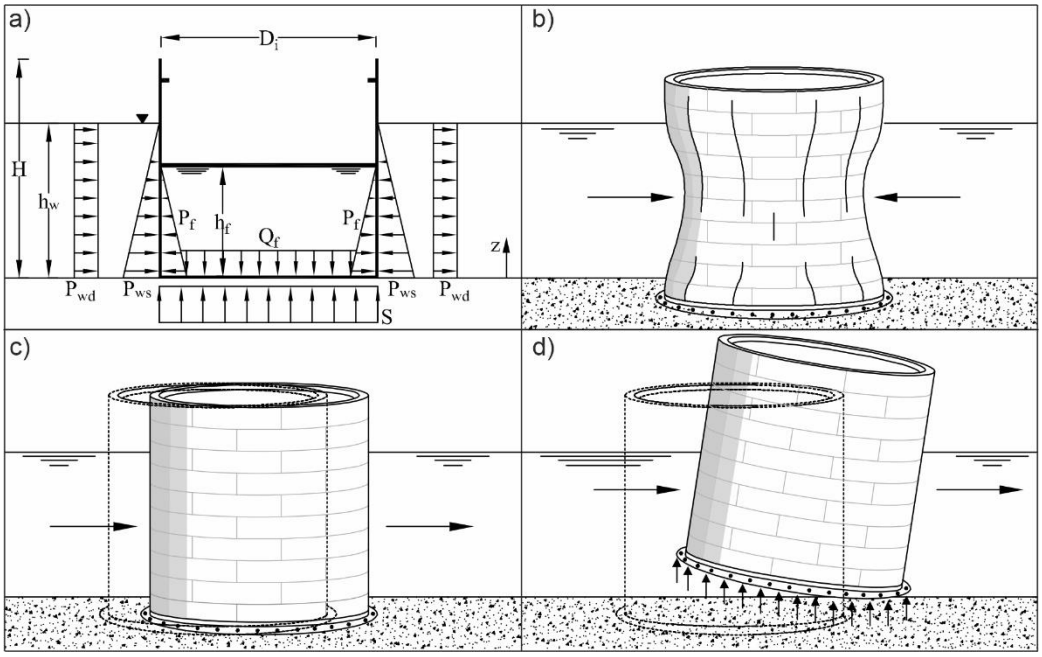

Figure 2.1: a) equivalent static tsunami load and schematic representation of possible failure modes considered: b) shell buckling, c) the shear failure of the anchors, and d) the tensile rupture of the anchors.

2.1.1 Equivalent static loads

A simplified taken on the effect of tsunami inundation on structures, in terms of loads, consists in separating these effects into a hydrostatic and a hydrodynamic component. In this context, each component can be represented by an equivalent static load, as suggested by various works [70], which is also the approach adopted by a number of normative documents on structural actions for design [46,65]. Furthermore, the same simplified approach has been adopted in the past in the context of atmospheric tank risk analysis against flooding [53] and tsunami and the same path is followed in the present study as well.

More specifically, the hydrostatic component consists of an external lateral pressure, $P_{ws}(Z)$, and a corresponding buoyant pressure $S = P_{ws}(Z = 0\ m)$, from Eq.(2.1):

$$P_{ws}(Z) = \rho_w \cdot g \cdot (h_w - Z) \tag{2.1}$$

where ρ_w is the mass density of the inundating water, g is the acceleration of gravity, Z the distance from the inundation surface and h_w the corresponding depth. In this case, a value of $\rho_w = 1.2\ t/m^3$ is assumed, corresponding to seawater with sedimentary content according to [65]. On the other hand, the hydrodynamic component is represented by a uniform lateral load along the direction of flow, whose value is provided by Eq. (2.2):

$$P_{wd} = \frac{1}{2} \cdot C_d \cdot \rho_w \cdot v_w^2 \tag{2.2}$$

Where C_d is the drag coefficient, which depends on the obstacle's (tank) geometry, taken here as two [65], and v_w is the average particle velocity of the wave normal to the structure. Finally, the internal liquid provides on the tank wall a hydrostatic action, P_f, given by Eq. (2.3) and on the base plate a dead weight load $Q_f = P_f(Z = 0\,m)$.

$$P_f(Z) = \rho_f \cdot g \cdot (h_f - Z) \tag{2.3}$$

where ρ_f is the mass density of the contained liquid, taken as $0.81\ t/m^3$, which corresponds to an average value for flammable substances typical of the petrochemical industry, and h_f is content liquid height.

2.1.2 Failure modes

As mentioned earlier, the failure modes taken into account for the fragility analysis of the tanks, that is shell buckling under compressive circumferential stresses, shear failure of the anchorage system and uplift due to failure of the anchors against tensile load, all potentially lead to displacements that are too large for the pipe-to-tank connections to accommodate. For this reason, it is assumed that exceedance of each tank's capacity (C) against any of these failure mechanisms by tsunami-induced demand (D), will lead to a rupture of one or more pipe connections and consequent loss of content.

Some textbook analytical formulations (e.g., [71]) lead to evaluate the critical load at which the shell begins to buckle, but under simplified assumptions as the small deformation or without to consider the interaction between hydrostatic and hydrodynamic tsunami pressures. So, given the complexity of wave propagation phenomenon and the nonlinearity response of the tank at the external loads, the present study, uses an *FEM* model to calculate demand and adopts the Eurocode 3 part 1-6 [67] procedure for evaluating the capacity of the steel cylindrical shell against buckling, where said capacity is expressed in terms of the design circumferential compressive stress leading to instability,$\sigma_{\theta,C}$, as per Eq. (2.4):

$$\sigma_{\theta,C} = \alpha_\theta \cdot \sigma_{\theta,cr} \tag{2.4}$$

where $\sigma_{\theta,cr}$ is the critical circumferential compressive stress calculated according to [67] and α_θ is a coefficient that accounts for geometric imperfections and depends on fabrication quality. This approach can be justified by the fact that cylindrical tanks subjected to tsunami- or flood-induced external pressure are expected to reach instability under stresses in the elastic range, unlike the seismic case where buckling is often observed in locations where plastic strains have been developed. In more detail, Bakalis and Karamanos (2021) [72] have observed that during the uplift of an unanchored storage tank, due to the seismic action, two regions at the base of the shell wall exceed the yield limit of the steel material, while the remaining part presents low levels of stresses and deformations. The yielding of the steel is observed near the connection zone between the base plate and the shell wall at the uplifted side, and the lower course of the shell wall at the compression side. Thus, the tank's capacity to withstand buckling depends not only on the shell slenderness, but also on the geometric imperfections that are mainly concentrated at the locations where curved steel plates are welded together to form the cylindrical shell. In the present chapter, uncertainty in fabrication quality is taken into account by arbitrarily assuming that α_θ is a normal random variable (RV) with a mean of 0.65, which would correspond to high fabrication quality according to Eurocode 3-1-6 [67] (an arbitrary value taken as mean value between $\alpha_\theta = 0.75$ and $\alpha_\theta = 0.50$, that are the two values α_θ corresponding to excellent and normal fabrication quality, respectively) and standard deviation of 0.125.

Regarding the shear and axial bearing capacity of the anchorage system, consisting of steel anchor bolts embedded in the concrete of the foundation raft, recourse was made to literature recommendations [73], which are based on experimental data, that link capacity to the nominal design strength and also provide a measure of its dispersion. More specifically, for the axial bearing capacity two failure mechanisms are considered: steel rupture of the anchor bolts and concrete cone breakout. The tensile capacity associated with concrete cone breakout, $N_{u,c}$, is given by a semi-empirical formulation based on experimental data [74], where the failure load for headed stud fastening systems can be calculated as:

$$N_{u,c} = \alpha_c \cdot \left(16.8 \ \frac{N^{0.5}}{mm^{0.5}} \right) \cdot L_B^{1.5} \cdot f_{ck}^{0.5} \tag{2.5}$$

where f_{ck} is the concrete characteristic compressive strength, L_B the embedment length, both expressed in using units of N and mm, and α_c is a Normal RV with mean 0.99 and standard deviation 0.178. Only values of $\alpha_c > 0$ are allowed because tensile steel strength cannot be negative. For the tensile strength of the anchor bolt itself, a deterministic value was considered, calculated using the mean ultimate stress. An experimentally calibrated semi-empirical model was also used for the anchors' shear capacity, $V_{u,s}$ [75]:

$$V_{u,s} = \alpha_V \cdot A_s \cdot f_{ub} \tag{2.6}$$

where A_s is the nominal cross-sectional area of an anchor bolt, f_{ub} the bolt's ultimate tensile stress and α_v is another normal RV with mean 0.68 and coefficient of variation of 0.35.

In addition to failure criterions discussed above, sloshing phenomena of the stored contents are not taken into account, for two main reasons, because the behaviour of the tank is examined considering the tsunami action applied quasi-statically, and also because the tanks of the case study are equipped with floating roof that reduces drastically the movement of the liquid mass at the top. Another failure criterion not investigated is the failure of the welding connection.

2.1.3 Design of archetype tanks

Floating-roof atmospheric storage tanks, whose main scope is the storage of highly flammable liquids such as gasoil, fuel, or combustible oils, are generally designed according to the provisions for steel thin-shell structures. The main structure consists of a cylindrical shell supported by a base plate and featuring a floating plane roof that can adapt to the level of the liquid content. The primary objective of adopting a floating roof solution is to avoid gas accumulation under the roof, from the evaporation of the liquid contents, that may pose a blast hazard. Another objective is the prevention of gas leakage from the roof-shell junction, thanks to the roof's flexible sealing joint. These tanks can be closed-off by a fixed roof or just rely on the floating roof whose motion beyond the top is impeded by a stiffening ring beam. The base plate consists of a thicker annular plate, which extends beyond the outer face of the vertical shell to accommodate anchor bolts installation and possible local uplift. Extension of the base plate acts as a simple bearing plate where are located the anchor bolts that fix the structure to the foundation.

For the purposes of this study, three archetype storage tanks are designed according to European standards. Each tank is chosen to represent a different height-to-base radius ratio. Equivalent static wind and seismic actions for the design are calculated according to the Eurocodes, [68,76] for a reference coastal site in northern Sicily (Italy) as a plausible site for an oil refinery. Given that the archetype tanks are presumed to operate under atmospheric pressure, their cylindrical steel shell wall, base plate and anchorage system are designed in accordance with the provisions of Eurocode 3 [66,67,69]. For the preliminary design phase, the recommendations of the widely used American Petroleum Institute standards (*API*) [77] were also followed, regarding the width of the external annular base plate and minimum thicknesses of the cylindrical steel shell wall and base plates. Another consideration was to design the annular base plate with thickness inferior to that of the vertical shell, so as to lead potential yielding under seismic conditions away from the wall base and towards the base plate [78]

Some schematic drawings of a typical tank are shown Figure 2.2, including horizontal and transverse sections along with the configuration near the anchor bolts. These drawings also help define the geometry

parameters used herein, that is the thicknesses of the cylindrical shell near the base, t_w, the base plate, t_{bp}, and the annular plate, t_{ap}, the width of the annular plate, w_{ap}, and the anchor bolt diameter, d_B, number, n_B, spacing i_B, and embedment depth in the concrete foundation raft, L_B. Following the indications of the standards above, three tanks with different slenderness ratio are considered. In this context, the slenderness is defined by the ratio between the maximum height of liquid content, $h_{f,max}$, and the radius of tank, R. It also was assumed a freeboard of $1\,m$ for all tanks, so that $h_{f,max} = H - 1\,m$, where H is the height of tank. The slenderness values are reported in Table 2.1.

Moreover, the tanks are designed with a steel of class *S355*, while the anchor bolts with a steel of resistance class of *8.8*. For the design of tanks with diameter $D < 60\,m$, according to [77], it is allowable that the thickness of the shell is uniform along all height. Table 2.1 also reports the geometrical features of tanks analysed for this study, that are the outcomes of nonlinear elastic analyses of FEM models, that will be described in next section, using the combinations of actions of Eurocode 0 [79] and also indications about seismic action of Eurocode 8-1 [80]. The seismic parameters used for obtaining the pseudo-acceleration spectra, in \a return period of $Tr = 475\,yr$, it is considered a peak ground acceleration calculated on the rock of $0.1607\,g$. In addition, the soil is classified to be of *C* category according to Eurocode 8-1 [80].

Table 2.1: Geometrical characteristics of archetypes tanks.

Tank	H	R	$h_{f,max}/R$	t_w	t_{bp}	t_{ap}	w_{ap}	d_B	n_B	i_B	L_B
	[m]	[m]	[-]	[mm]	[mm]	[mm]	[m]	[mm]	[-]	[mm]	[mm]
Slender	11	5	2	20	8	10	1	27	12	2640	216
Intermediate	13	12	1	25	15	20	1.8	30	45	1750	240
Squat	15	28	0.5	30	20	25	2	39	120	1470	312

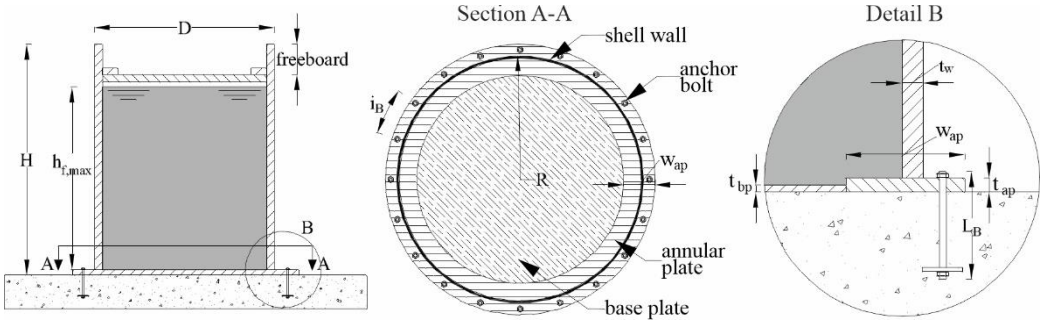

Figure 2.2: Scheme of floating-roof anchored atmospheric storage tank.

2.2 Numerical models and structural analysis

2.2.1 FEM model and non-linearities

The three archetype tanks are modelled using four-node finite elements available in the software SAP2000 v.23.0.0 [81], that combine plate bending and membrane action formulations. The finite element mesh discretization is increased towards the base of the cylindrical shell, adapting to the expected concentration of bending-induced stresses, as shown in Figure 2.3. The presence of a stiffening ring beam along the rim of the tank is modelled by means of a kinematic constraint of the top nodes that conserves the undeformed circular shape.

In such cylindrical tanks, the boundary conditions in the vicinity of the annular plate can be affected by localized uplift under certain loading conditions. For example, past works have analysed the behaviour of the partial uplifting of the base plate for cylindrical tanks subjected to internal hydrodynamic pressures induced by seismic actions [82,83]. In that case, base uplift was also accompanied by material non-linearity, mainly due to yielding of the annular plate. In the case at hand, the yielding of the base plate is not considered because the exceedance of this stress does not provide the rupture, but a large inelastic deformation that may lead to high repair costs [84]. The contact of the base circular and annular plates with the foundation mat was modelled via unilateral compression-only Winkler springs [57] corresponding to a coefficient of subgrade reaction of $50\ N/cm^3$, while material non-linearity for the tank steel was not included in the model.

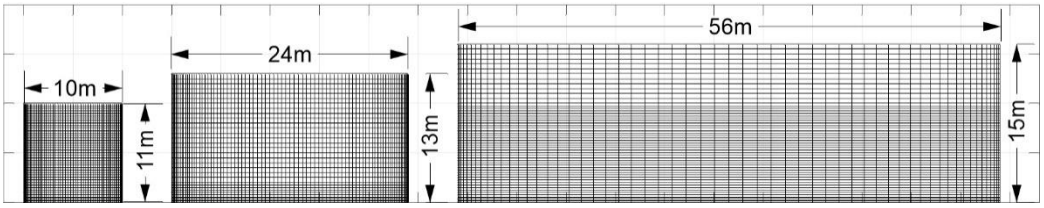

Figure 2.3: FEM models of archetypes tanks.

On the other hand, consistent with the design assumption of no preloading of the anchor bolts, their axial behaviour was modelled via tension-only bilinear yielding springs. Shear behaviour of the anchor bolts in the model was assumed linear elastic; given that friction forces between base plate and foundation mat were not included in the model, the consideration of possible failure mechanisms involving bolt shear was relegated to the post-processing of analysis results. The elastic stiffness of the anchor bolts under axial force was calculated according to Eurocodes 3-1-8 [69] while for shearing stiffness no information is available inside the citated Eurocode. For this reason, the shear stiffness was evaluated, in approximate way, modelling an individual anchor as fixed at the bottom and free to translate but not to rotate at the top, when it is subjected to a horizontal force at the top (more details are given in Appendix).

Figure 2.4-a) shows the gradual uplift response of the intermediate tank's base plate, as the tsunami height increases from 2.7 m to $2.8\,m$, while flow velocity is fixed at $1\ m/s$ and the tank is filled up to one-third of its maximum storage capacity. The figure helps appreciate the fact that, depending on each tank's filling level, buoyant forces from the tsunami can lead to an almost complete loss of contact of the base plate to the foundation. For these cases, it was necessary to include large-displacement geometric non-linearity in the analysis, in order for the model to account for the stiffening effect of membrane forces generated in the deflected base plate, avoiding unrealistic deflections predicted by plate bending theory. Generally, the base plate is not designed to resist vertical actions directed upward. For this reason, when the buoyant force exceeds the self-weight of the tank and the liquid content, the base plate loses contact with the foundation mat. The anchors are the only components of the tank-system that react to buoyant force, reducing the floatation probability. The failure of the base plate may be associated with the exceedance of the yielding tension stress of the steel, but in this case, large plastic deformations may be observed, but likely without leading to the loss of contents. The behaviour of the bottom plate under the buoyant force is also studied by Mia et al. (2023) [84]. They show that the exceedance of the yielding stress depends on the thickness and the diameter of the base plate. An adequate thickness prevents the spillage of the stored contents. In addition, anchored tanks with small diameters

have a low probability of floatation, because the resultant of buoyant force is proportional to area of the base plate, thus, likely the anchors are able to resist to this resultant force. On the contrary, anchored tanks with large diameters manifest shell buckling before of the yielding of the base plate. For these reasons, the failure of the base plate is not taken into consideration in the analysis but is considered in the design of the thicknesses as shown in Appendix.

Figure 2.4-b) shows the values of the membrane compressive circumferential stresses σ_θ at the nodes of the shell elements of wall, along the direction of flow, fixing the velocity and the external height of the tsunami. Two cases examined in figure refer to the squat tank with filling levels of $3\ m$ and $5\ m$, respectively, one lower than and the other equal to the $5\ m$ of external tsunami height. In both cases, Archimedes' force is greater than the self-weight of the tank, because otherwise the hydrostatic pressure of the internal liquid develops circumferential stresses putting in tension the whole structure. The results of nonlinear elastic analyses in large displacements show a concentration of compressive circumferential stresses (negatives values in figure) in the zone around of $3\ m$ from the base of the tank, for both cases. This seems to highlight that the influence of filling level has an effect only on the modulus of stresses, that reduce themselves increasing internal liquid, but the zone where the shell buckling can happen, remains the same. Another consideration can be done around the connection zone between base plate and base of the wall. In this area, it is observed a relevant concentration of compressive circumferential stresses. This disturbance could depend on from the fact that the material non-linearity of the shell elements does not take into considerations and for this reason the redistribution the stresses during the steps of the nonlinear analyses does not allow. But this effect due to modelling problem is not relevant for the scope of this chapter, because the shell buckling could never occur near the base of the shell wall. Another cause of this effect could be an insufficient discretization of the mesh that does not catch well the real behaviour at the base. In this connection, the reliability of the mesh was verified through validation analyses comparing the circumferential stresses outcoming from linear elastic analyses, of the only shell walls of the tanks examined with the analytical solutions of bending theory, considering as boundary condition the tanks fixed at the base [85].

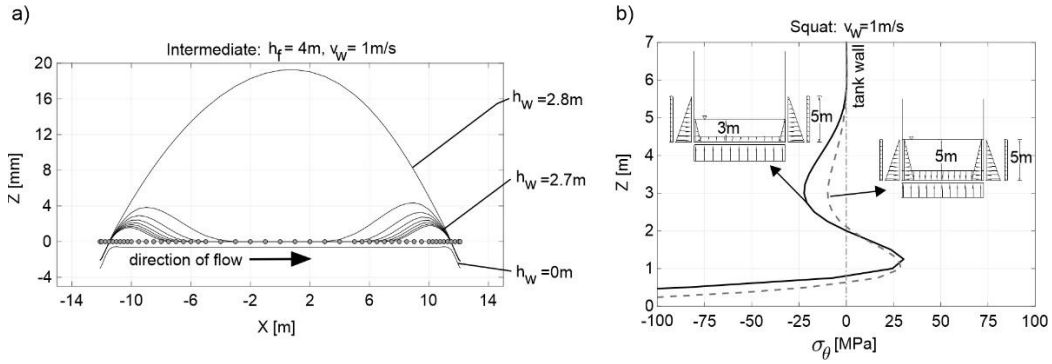

Figure 2.4: a) Uplift of the base plate of intermediate tank. b) Membrane circumferential stresses along the shell wall of squat tank.

2.2.2 Results and discussion

For each archetype tank, a series of analyses were carried out varying the tank's content level and the tsunami height and velocity. More specifically, the liquid content levels cover the entire allowable range, starting from a minimum filling level of one metre and going up to each tank's $h_{f,max}$, at $1.0\,m$ increments. Tsunami height values are taken to vary from a lowest-considered value of $1\,m$ up to each tank's full height, again at one-metre increments. In addition to these levels, also $0.5\,m$ of filling is considered. Finally, water velocities considered ranged from zero to $5\ m/s$, at $1\ m/s$ increments. For the slender tank alone, velocity was considered up to $10\ m/s$, in order to better map the development of tensile forces imposed on the anchors. The upper limits of these intervals were chosen after examining a series of inundation scenarios, as discussed in the next section.

The static nonlinear analysis is distinguished into two steps. Initially the tank is loaded with the self-weight and hydrostatic pressure of the filling level; then hydrostatic and hydrodynamic pressures of the tsunami are applied. The tsunami action on the tank is applied considering the same height level across the circumference. In detail, the hydrostatic pressure acts in radial direction towards the centre with an equal intensity for each direction across the circumference, while the hydrodynamic pressure has direction and verse of the flow and an intensity that varies with the cosine

of the angle between flow and radial direction. The main results that were extracted from each run for post-processing were the peak average circumferential compressive stress in the cylindrical shell wall, $\sigma_{\theta_{max}} = min\big(\sigma_\theta(Z \geq 1\,m)\big)$ and the tensile forces at the anchor bolts F_T. An example is shown in Figure 2.5 , where the results in terms of $\sigma_{\theta_{max}}$ are plotted for five filling levels of the slender archetype tank, for various tsunami heights, for a velocity of $1\ m/s$. The variation of $\sigma_{\theta_{max}}$ versus the velocity does not relevant, for this reason it is chosen to focus on the variation with the tsunami height. The results of the nonlinear elastic analyses in large displacements show a trend ascendent and linear for fixed filling level. Fixing a generic value of tsunami height, the greatest circumferential stress is associated with the case of tank almost empty, while the cases in which the $\sigma_{\theta_{max}}$ is null, mean that the shell wall is put into tension by hydrostatic action of liquid content and the tsunami wave effects can be neglected.

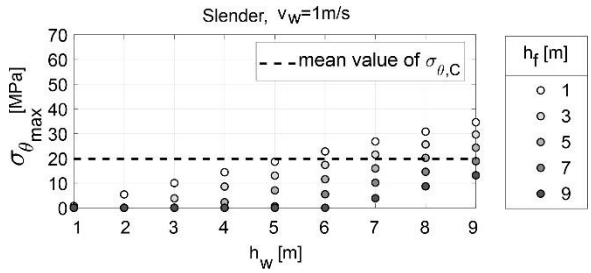

Figure 2.5: Maximum circumferential compressive stress in the shell wall for different levels of tsunami heights and levels of liquid content for slender tank.

Figure 2.6 shows the tensile force of two anchors in the slender tank, varying the tsunami velocity for five levels of tsunami height and for two filling levels of $1\ m$ and $9\ m$, respectively in panel a) and b). The black points on the circumferences indicate the positions of the anchor examined in two panels and the arrows the direction of the flow. The objective of figure is to investigate the effect of interaction between buoyant force and hydrodynamic pressure, in more detail between the uplift and the overturning moment, for the cases of tank almost empty, in panel a), and full, in panel b). The choice to examine two anchors in figure is justified from the fact that it is unnecessary to show the tension of the anchor located in upward direction because for fixed tsunami height, increasing the velocity, this anchor would carry on increasing its level of

tension, not providing any helpful information on the response of the tank. Conversely for the anchor located in leeward direction, in Figure 2.6-a), where for a low level of filling, it shows a decrease of tension when the velocity increases. What happens it is that at the beginning, for velocity values equal to zero, all anchors are in tension for all selected tsunami heights. In these cases, only the presence of the Archimedes' force acts on the tank because the hydrostatic actions are self-balanced. This means that the base plate losses completely the contact with the foundation mat and only the anchors react to the buoyant force. As well as the velocity increase, the hydrodynamic pressure induces a rotation of the tank with subsequently decrease of the tension inside the anchor to the leeward, this implies that the base plate approaches to the foundation mat. For values of velocities greater than $6\ m/s$ it is observed that the tension is null, this means that the base plate is in contact with the foundation putting itself in compression and discharging the anchor. In Figure 2.6-b), it is analysed the behaviour of the anchor located in orthogonal direction to the flow when the tank is completely full. Contrary to the case of tank almost empty, where for all selected tsunami levels the Archimedes' force was greater than self-weight, now this condition is verified only for $8\,m$ and $9\,m$, and this it is evident looking at F_T values do not null for velocity equal to zero. Focusing only on $8\,m$ and $9\,m$ of tsunami height, it is observed that up to velocities of $2\ m/s$ the tank results completely uplifted to the ground and all anchors are in tension; with velocities greater than $2\ m/s$ some anchors begin to decrease their tension level, leading the opposite part to the flow direction of the tank to be in contact with the foundation. For $4\ m/s$ e $5\ m/s$, the tank is supported on the foundation mat for half part of the base plate, corresponding to its semi-circumference, and for this reason that in figure it reads a tension force equal to zero. Then for velocities greater than $5\ m/s$ the selected anchor returns to being in tension, but, from this point on, the part of base plate in contact is always the same and increases only the values of tension in the anchors. The failure of the anchors with the subsequently redistribution of the forces is not covered from *FEM* model, but only in post-process it is taken into account of this for the fragility calculations.

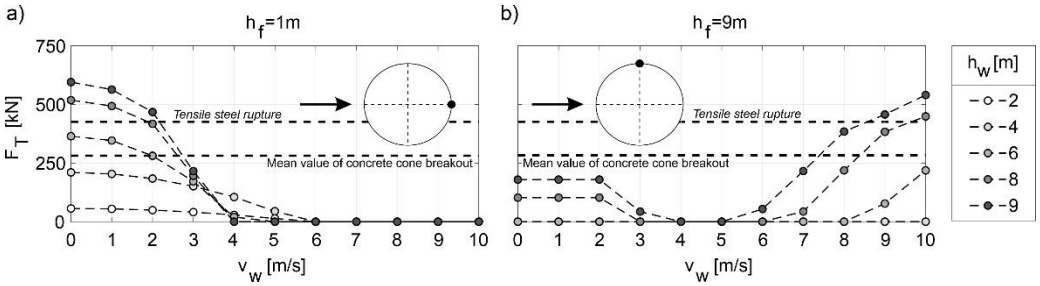

Figure 2.6: Tensile force of two anchors in the slender tank, for some values of tsunami height and velocity, in condition of: a) empty tank; b) full.

2.3 Derivation of fragility functions

2.3.1 Treatment of uncertainties on the demand parameters

Static nonlinear analysis on the tanks has the scope to study of the behaviour of the structures under different heights and velocities of tsunami, having fixed the internal filling level. On the other hand, to derive the fragility functions, it needs to analyse the scenarios of tsunami height and velocity that can occur at the site of interest and to select the scenarios that presumably can lead to the structural damage of the tank. This evaluation can be done only analysing the simulations of the wave propagation at the site of interest. As discussed in Section 1.3.2, the maximum tsunami height happens almost never at the same time the maximum tsunami velocity, thus, to consider the maximum of both two demand parameters, is a condition very disadvantageous and unlikely. The conditions most realistic are ones in which the velocity is evaluated in correspondence of maximum tsunami height. Thus, regression analysis was done under these assumptions.

The uncertainties on the demand parameters are given to the distribution of residuals the of the logarithm of the $\tilde{v}$ and the mf_{max}, in Figure 2.7. For each value of $h_{w,max}$, the behaviour of the tank is analysed for values of velocities and momentum flux obtained from the residual distributions.

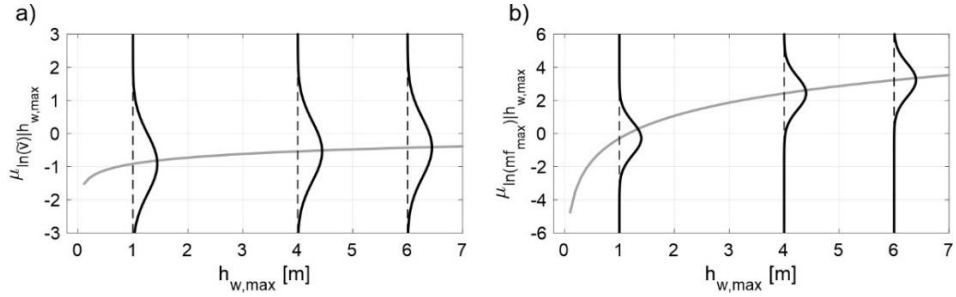

Figure 2.7: Conditional distribution of a) logarithm of tsunami velocity at the time of maximum height and b) logarithm of maximum momentum flux.

The fragility curves are expressed in this context as probability of failure. The failure, F, is intended as a structural damage that involves into

release of hazardous substances, when the tank is subjected to a certain level of maximum tsunami height $h_{w,max}$ and a fixed percentage of internal liquid level, Ψ. The probability of failure is calculated according to Eq. (2.7):

$$P\left[F \mid h_{w,\max}, \Psi\right] = \\ = \int_{\tilde{V}} \int_{MF_{\max}} P\left[F \mid \tilde{v}, mf_{\max}, h_{w,\max}, \Psi\right] \cdot f_{MF_{\max}|\tilde{V},H_{w,\max}}\left(mf_{\max} \mid \tilde{v}, h_{w,\max}\right) \cdot f_{\tilde{V}|H_{w,\max}}\left(\tilde{v} \mid h_{w,\max}\right) \cdot d(\tilde{v}) \cdot d\left(mf_{\max}\right) \tag{2.7}$$

in which $f_{MF_{max}|\tilde{V},H_{w,max}}\left(mf_{max}|\tilde{v}, h_{w,max}\right)$ is the conditional probability density function of momentum flux given the velocity at the time instance of maximum height and the maximum height; $f_{\tilde{V}|H_{w,max}}\left(\tilde{v}|h_{w,max}\right)$ is the conditional probability density function of velocity at time instance of maximum height given the maximum height. These quantities are obtained in conditional hazard of Section 1.4. Lastly, $P\left[F|\tilde{v}, mf_{max}, h_{w,max}, \Psi\right]$ is the conditional probability of exceeding of a particular damage state capacity given an event of a particular velocity, momentum flux and height, when the tank is filled up to a certain level. The evaluation of the failure and the corresponding probability is discussed in the next section.

2.3.2 Treatment of uncertainties on the capacities

Objective of this Section is the calculation of $P\left[F|\tilde{v}, mf_{max}, h_{w,max}, \Psi\right]$. In Section 2.1.2, it was discussed of failure mechanisms at which a generic anchored atmospheric liquid storage tank with floating roof may be subjected during tsunami impact. Thus, the probability to observe at least one failure mechanism is equal to Eq. (2.8) :

$$P\left[F \mid \tilde{v}, mf_{\max}, h_{w,\max}, \Psi\right] = 1 - \prod_{i=1}^{3}\left(1 - P\left[F_i \mid \tilde{v}, mf_{\max}, h_{w,\max}, \Psi\right]\right) \tag{2.8}$$

where $i = 1,2,3$ indicates the failure mechanism activated, in particular $i = 1$ is the shell buckling; $i = 2$ is the tension failure of the anchor bolts; and

$i = 3$ the sliding of the tank after the shear rupture of the anchors. $P\left[F_i|\tilde{v}, mf_{max}, h_{w,max}, \Psi\right]$ is the probability of failure associated with one out of three mechanisms. The product indicates the stochastic independence between mechanisms.

In more detail, a failure criterion is associated at each mechanism. For the shell buckling, the criterion regards the uncertainty associated with fabrication process, in particular from the Eq.(2.4), it is possible to identify the capacity and to evaluate the probability of failure for shell buckling as showed in Eq.(2.9):

$$P\left[\alpha_\theta < \frac{\sigma_{\theta_{\max}}}{\sigma_{\theta,cr}} | \tilde{v}, mf_{\max}, h_{w,\max}, \Psi\right] = \Phi\left(\frac{\frac{\sigma_{\theta_{\max}}}{\sigma_{\theta,cr}} - 0.65}{0.125}\right) \tag{2.9}$$

where $\sigma_{\theta_{max}}$ is the maximum compressive circumferential stress along the middle plane of shell wall under a certain tsunami action and internal filling condition. This probability is evaluated as a standard normal cumulative distribution with mean and standard deviation defined in Section 2.1.2.

The probabilities regarding the failures of shear and tension of anchor bolts are assessed by Monte-Carlo simulations.

The shear failure occurs when the tank slides under lateral actions induced by the tsunami causing the shear rupture of the anchors. These lateral tsunami actions are due primarily to hydrodynamic forces that are proportional to the momentum flux. Thus, the shear failure is conditioned by maximum momentum flux acting on the tank and by the corresponding tsunami height that on average occurs. The mean of the logarithm of tsunami height in correspondence of maximum momentum flux, $\mu_{ln(h_w)|mf_{max}}$ is derived from time histories through a regression analysis and the results are plotted in Figure 2.8, while the equation of the regression curve is expressed by (2.10).

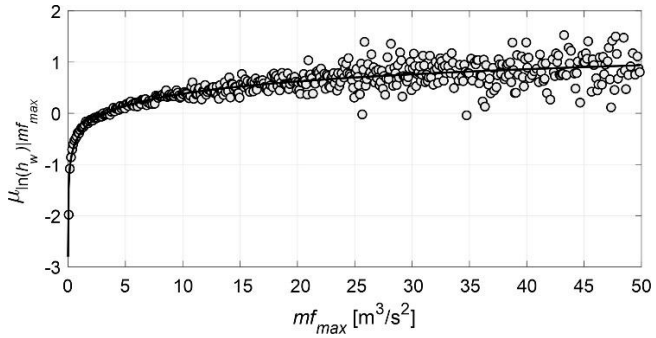

Figure 2.8: Nonlinear regression curve of the mean of the logarithm of the height given maximum momentum flux.

$$\mu_{\ln(h_w)|mf_{\max}} = 0.3456 \cdot \ln\left(mf_{\max}\right) - 0.4138 \tag{2.10}$$

The objective of the regression analysis is to quantify the Archimedes' force acting on the tank at varying of the momentum flux and to investigate its behaviour. Two different conditions can occur. The first one regards the case of the Archimedes' force greater than self-weight. Here, the base plate is completely lifted off the foundation mat and only the anchors can resist at the lateral actions. The other one regards the Archimedes' force when is less than or equal to self-weight. In this case, the base plate is totally or partially in contact with the foundation mat and the lateral tsunami action is opposed by both the anchors but also by friction developed between the concrete of the foundation and the steel of base plate.

Focusing on the first case, each anchor is loaded with a shear equal to the hydrodynamic force resultant uniformly distributed throughout all anchors. This simple way to distribute the shear is on the safe side because from analysis with *FEM* model, it results that the shear forces in each anchor are negligible, especially for tanks for large diameters. Instead, on the side of shear capacities, the shear resistances of all anchors are assumed stochastically independent and identically distributed. This means that the shear resistances of each anchor are different from each other, and their values are randomly extracted from same probability density function of α_V, defined in Section 2.1.2. At this point, the shears of anchors are compared with the corresponding

resistances to evaluate how many of these are failed. The failure of only some anchors involves in a redistribution of forces in uniform manner on the remaining and a revaluation of demand over capacity ratios that allows to identify the possible failure of other anchors. The iterations stop when or all anchors fail or resist. This is the outcome of one simulation inserted in Monte-Carlo method. In the first case, the simulation implies failure, otherwise no. Thus, the probability of failure is evaluated as the ratio between the number of failed simulations and the total number of simulations.

For the case in which the Archimedes' force is less than or equal to self-weight, the friction force should be considered. From phenomenological point of view, it happens that up to certain levels of momentum flux, the anchored tank does not move, the anchor deformations are nulls and shear forces are completely absorbed from the friction. But as soon as the momentum flux increases and the available friction resistance is exceeded, the tank begins to slide, and the anchors are required to engage in bearing. The contact between the anchors and the base plate provides large deformations and consequently an increase of shear demand in the anchors that load themselves up to reach the ultimate shear capacity corresponding to steel rupture. The load-displacement behaviour of an individual anchor to the shear also includes failure mechanisms of the concrete [86], but in this thesis are not investigated. In addition, the anchor-base plate-foundation interaction is not conceived in the *FEM* model, and the friction is considered in post-process as a force to subtract at the shear of the anchors. In each simulation, the value of friction coefficient is extracted from a *RV* variable normally distributed with mean 0,5 and coefficient of variation of 0,3 [87].

Lastly, the tension failure of the anchors happens if all anchors exceed at least one resistance between the concrete cone breakout and/or the tension steel rupture. Also in this case, it proceeds with Monte-Carlo simulations consisting in the progressive failure of the anchors, as well as explained for the shear case. The differences with the previous case are that the friction force does not contribute to the equilibrium of the vertical forces and the redistribution of the forces due to the failed anchors happens in proportional way. This last assumption takes into consideration the fact that the anchors are not subjected only to tension, but also to a bending moment caused by the hydrodynamic pressure. In these

conditions, it develops a neutral axis that divides the base plate into two parts, one compressive and the other one tensile, but since the effect of the hydrodynamic action does not make relevant changes to the depth of the neutral axis, this can be considered fix, in way that the stress increases proportionally after the failure of some anchors during the steps of a simulation. At the instance time in which at least one anchor fails, all the anchors are all in tension, thus, the neutral axis is outside the cross section. This because anchor failure is not so much due to the overturning moment, but rather to the buoyant force.

The definition of multiple random variables allows to discuss about the intracomponent and intercomponent correlations [88]. The intracomponent correlation refers to the stochastic dependency among the two capacity parameters for a single anchor. The intercomponent correlation, instead, presents the spatial dependency of the single capacity parameter among all anchors. From the results of the simulations, it is observed that, for an individual anchor, the tension failure is governed by the concrete cone breakout, while the shear failure is due to the shear rupture of the steel. For this reason, tension and shear strength of an individual anchor are assumed uncorrelated because the tension failure happens mostly on the concrete side. Thus, the intracomponent correlation between two strengths is not considered. On the other hand, the intercomponent correlation is taken into account only for the shear steel strength. For the tension steel strength, all anchors have the same strength value equal to the mean ultimate stress. For the shear steel strength, the probability of shear failure of the anchors is evaluated considering both all anchors with the mean value of the shear strength but also with strength values for each anchor extracted randomly from the same distribution. The results show that is not great differences for the two cases, thus, the second case is chosen for the fragility analysis.

2.3.3 Parametric models

The fragility curves obtained from nonlinear elastic analysis are, then, adapted to a parametric model. The parametric model that to describe the best fit model for all failure mechanisms, is the Weibull cumulative density function (*cdf*), defined through two dimensionless

parameters: the percentage of the filling level $\Psi = h_f / h_{f,max}$ and the percentage of the submersion of the tank, $\Phi = h_w / h_{f,max}$. The definition of the percentage of submersion is based on the assumption that the allowable maximum tsunami height level is the maximum filling level. Eq.(2.11) shows the probability of failure with Weibull distribution for each failure mechanism, $P[F_i|\Phi,\Psi\,]$.

$$P\left[F_i \mid \Phi, \Psi\right] = 1 - e^{-\left(\frac{\Phi}{a_i(\Psi)}\right)^{b_i(\Psi)}} \tag{2.11}$$

The subscript $i = 1,2,3$ is used, always, to distinguish the failure mechanisms, in particular, with $i = 1$ is indicated the shell buckling, $i = 2$ the tensile failure of the anchors and $i = 3$ the sliding after their shear failure. $a_i(\Psi)$ and $b_i(\Psi\,)$ are the Weibull scale and shape parameters, respectively. These two parameters are calibrated for filling level and for each failure mechanism. Figure 2.9 shows the trend of the two parameters at varying of filling level, for the three failure mechanisms, taking as example the intermediate tank. The figure is structured in way that the first row shows the values of a while the second one, values of b; instead, each column is referred to a failure mechanism. From the figure results that for shell buckling, both parameters have linear trend; while for the tension failure criterion, a is linear function while b is a parabolic function; lastly, for the shear failure criterion, both parameters are defined by a bilinear function. The equations of the parameters of the Weibull *cdf* with the filling level, are shown in Table 2.2 for all tanks geometries.

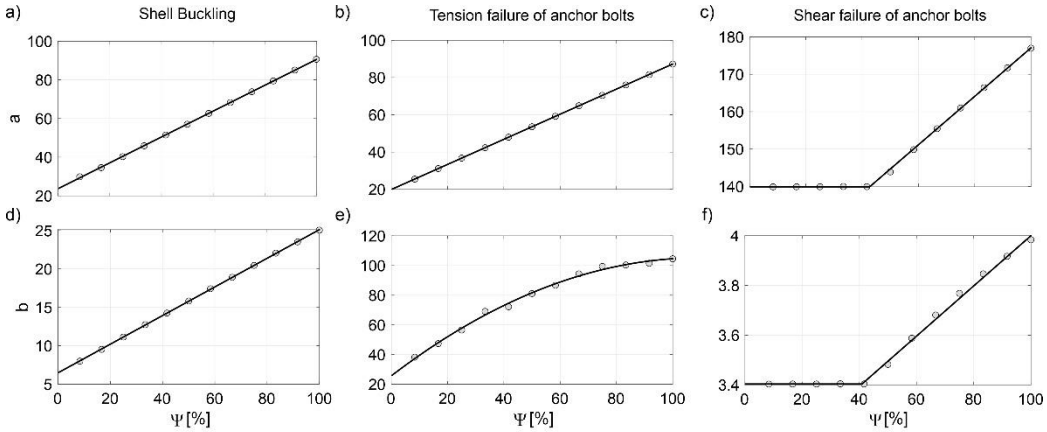

Figure 2.9: Parameters of Weibull *cdf* at varying of the filling levels, for intermediate tank. In the first row, the scale parameter "a" for failure mechanism: a) shell buckling; b) tension of anchor bolts; c) shear of anchor bolts. In the second row, the shape parameter "b" defined for: d) shell buckling; d) tension of the anchor bolts; e) shear of the anchor bolts.

Table 2.2: Scale and shape parameters of Weibull cdf for all tank geometries and failure mechanisms.

Tank	Shell buckling		Tensile failure of anchor bolts		Shear failure of anchor bolts	
Slender	a_1	$0.59 \cdot \Psi + 57.25$	a_2	$0.69 \cdot \Psi + 35.49$	a_3	$\begin{cases} 149.92 & \Psi < 45\% \\ 0.69 \cdot \Psi + 119.26 & \Psi \geq 45\% \end{cases}$
	b_1	$2.65 \cdot 10^{-5} \cdot \Psi^3 - 2.09 \cdot 10^{-3} \cdot \Psi^2 + 0.12 \cdot \Psi + 5.47$	b_2	$-2.30 \cdot 10^{-3} \cdot \Psi^2 + 0.33 \cdot \Psi + 16.88$	b_3	$\begin{cases} 3.20 & \Psi < 39\% \\ 5.70 \cdot 10^{-3} \cdot \Psi + 2.98 & \Psi \geq 39\% \end{cases}$
Intermediate	a_1	$067 \cdot \Psi + 23.69$	a_2	$0.67 \cdot \Psi + 19.90$	a_3	$\begin{cases} 139.92 & \Psi < 43\% \\ 0.65 \cdot \Psi + 112.23 & \Psi \geq 43\% \end{cases}$
	b_1	$0.19 \cdot \Psi + 6.48$	b_2	$-6.60 \cdot 10^{-3} \cdot \Psi^2 + 1.45 \cdot \Psi + 25.65$	b_3	$\begin{cases} 3.40 & \Psi < 41\% \\ 0.01 \cdot \Psi + 2.99 & \Psi \geq 41\% \end{cases}$
Squat	a_1	$0.66 \cdot \Psi + 10.15$	a_2	$0.67 \cdot \Psi + 11.82$	a_3	$\begin{cases} 145.74 & \psi < 45\% \\ 0.76 \cdot \Psi + 111.38 & \psi \geq 45\% \end{cases}$

	b_1	$0.42 \cdot \Psi + 9.00$	b_2	$-0.01 \cdot \Psi^2 + 4.44 \cdot \Psi + 35.31$	b_3	$\begin{cases} 3.69 & \Psi < 44\% \\ 0.01 \cdot \Psi + 3.01 & \Psi \geq 44\% \end{cases}$

The results of the fit are shown in Figure 2.10, for the case of intermediate tank when is half full.

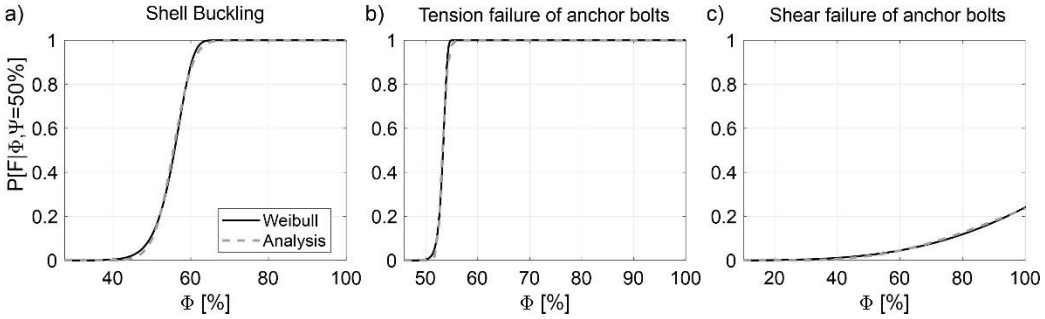

Figure 2.10: Validation of the fit model, for intermediate tank, for: a) shell buckling; b) tension failure of anchor bolts; and c) shear failure of the anchor bolts.

The parametric fragility functions that taken into consideration the interaction of all three failure mechanisms is obtained as Eq. (2.12)

$$P\left[F \mid \Phi, \Psi\right] = 1 - \prod_{i=1}^{3} \left(1 - P\left[F_i \mid \Phi, \Psi\right]\right) \tag{2.12}$$

2.3.4 Results

Figure 2.11 shows the fragility curves for slender (panel a), intermediate (panel b) and squat (panel c) tank given filling level Ψ, obtained from Eq. (2.12). The abscissa axis shows the percentage of submerged tank, while the percentage on each curve is referred to a given filling level.

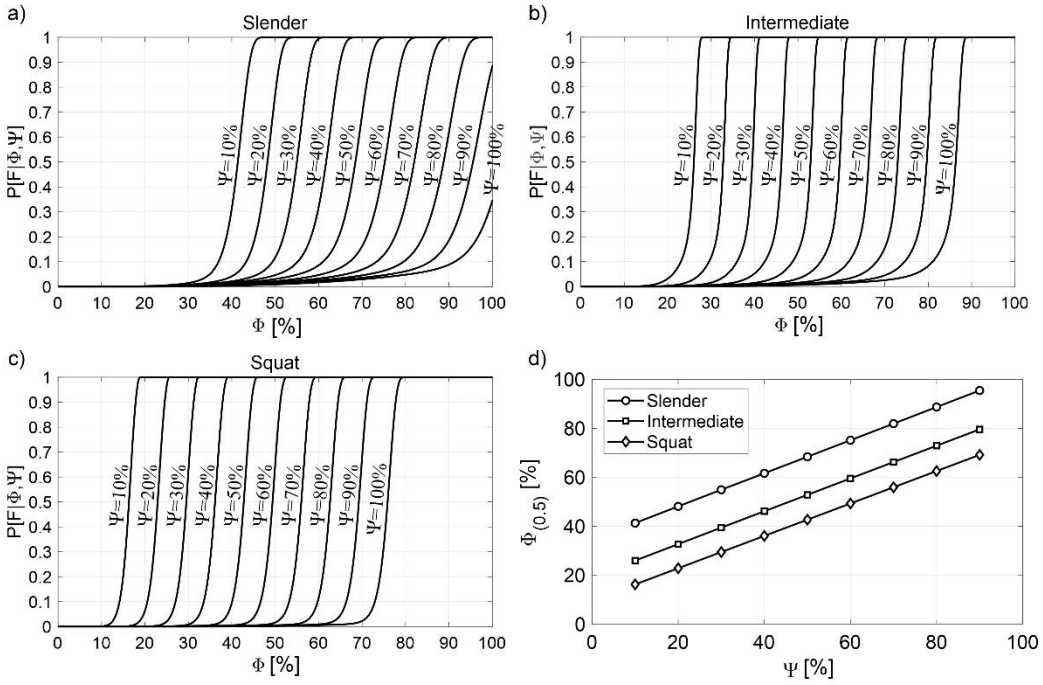

Figure 2.11: Fragility curves at varying of the filling level for: a) slender tank; b) intermediate tank; c) squat tank. d) Grade of submersion of the tank with probability of failure of fifty percent at varying of filling level.

Looking at an individual tank, the curves move to the right as the filling level increases. The meaning of this trend is explained in Figure 2.11-d), that showed an example the influence of the degree of filling on the vulnerability of the tanks. The panel d) shows the value of percentage of the submersion that has a probability of failure of the 50%, $\Phi_{(0.5)}$, with the filling level. The markers in figure indicate the filling levels considered in the other panels up to the 90%. The trend makes clear that the probability of failure of 50% is reached more rapidly for almost empty tank rather than for almost full tank. In quantitative terms, it is observed that for filling level of 10%, the probability of failure of 50% is reached for a grade of submersion of 40% for slender tank; 22% for the intermediate tank; and 18% for the squat tank. Conversely, a full tank needs of a tsunami wave that exceeds at least about the seventy percent of total height for all tanks to obtain a probability of failure of 50%. Particular case is the completely full slender tank that leads to that probability of failure of 50% when the tank is completely inundated. This last consideration may be an expected

result, because increasing the filling level, the hydrostatic action and the self-weight of the liquid content counteract the hydrodynamic and hydrostatic tsunami actions avoiding any type of failure mode. In additional, the panel d), shows that the three lines referred to three tanks are quite parallels and the lowest one is that of the squat tank. This means that for all filling levels, the fraction of submerged tank that leads to the probability of failure of 50% of the squat tank is always the lowest and for this reason results to be the most vulnerable.

The trend of fragility curves is influenced also by the failure modes. Figure 2.12 shows some examples of fragility curves for three tanks, for different filling levels, highlighting the influence of the failure modes. In detail, the rows show the different filling levels, and the columns are referred to three geometries. Each panel shows a dotted curve that is the overall fragility function considering the interaction of all failure mechanisms, while the dark grey curve is fragility curve built considering only the failure mechanism of the shell buckling; the grey curve is referred to only tension failure of the anchors; and the light grey curve corresponds only to the shear failure of the anchors. For low levels of filling level, the fragility curves seem to be governed from only one mechanism that is dominant on the others, in particular, it is observed the mechanism that controls the failure for the slender is the tension of the anchors, panel a); while, for the squat tank, the dominant failure mode is the shell buckling, panel c). In these panels, it is seen as the overall curve (dashed line) is almost completely overlapped to the curve of the predominant mechanism. Conversely, the intermediate tank presents more than one mechanism that governs the overall fragility curves for low liquid levels. In more detail, the panel b) and e) show the trend that it is common to all curves of the intermediate tank up to 50% of filling where for $P[F|\Phi,\Psi] \leq 0.2$ the fragility is what it would have if it were considered only the shell buckling, while for $P[F|\Phi,\Psi] > 0.2$ the curve carries on with an trend identified from fragility of only resistance mechanisms in tension. On the other hand, for high filling levels, the interaction of all mechanisms is not negligible, for this reason, the failure modes cannot be treated separately, as shown in panel g), h), and i). Focusing on the failure mechanism, it is observed that squat tanks are subjected to the shell buckling; contrary, slender tanks are affected by the tension failure of the anchors, while the intermediate tanks have an intermediate behaviour between two previous

cases. The shear failure of the anchor bolts, instead, is negligible because the anchorage system is adequately designed to resist to the seismic and wind design actions.

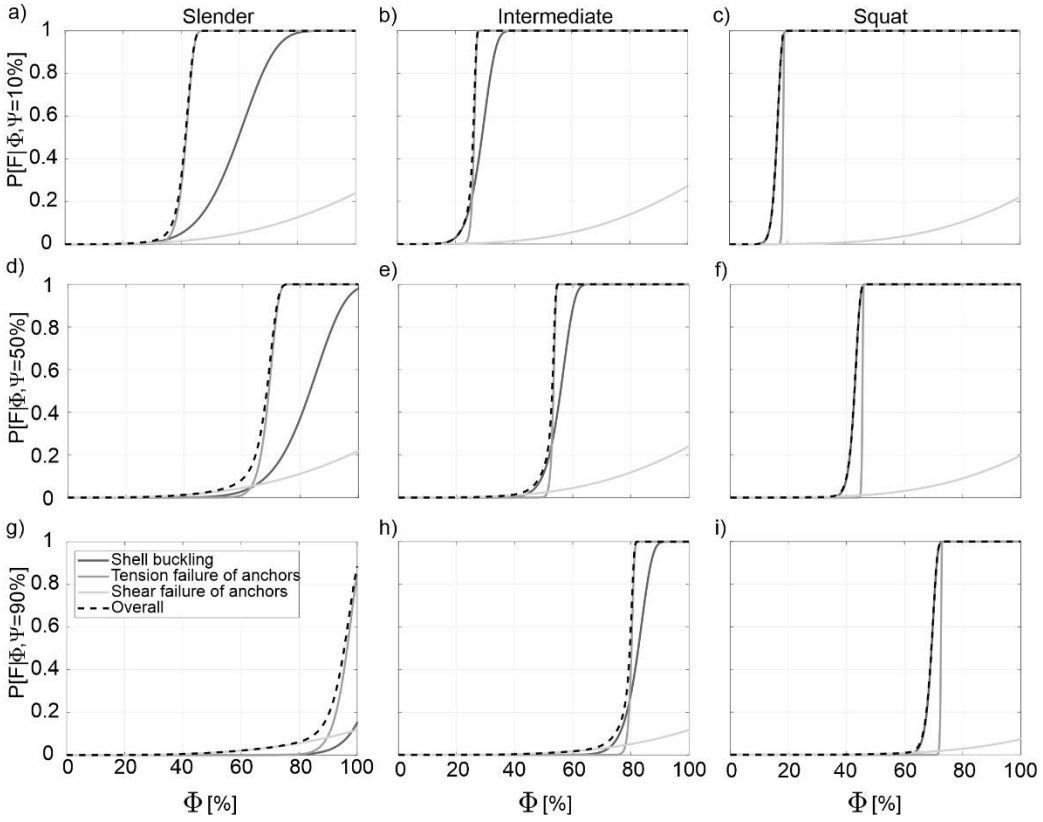

Figure 2.12: Fragility curves for individual failure mode. Fragilities for filling level of 10% for a) slender, b) intermediate, c) squat tanks. Fragilities for filling level of 50% for d) slender, e) intermediate, f) squat tank. Fragilities for filling level of 90% for g) slender, h) intermediate, i) squat tanks.

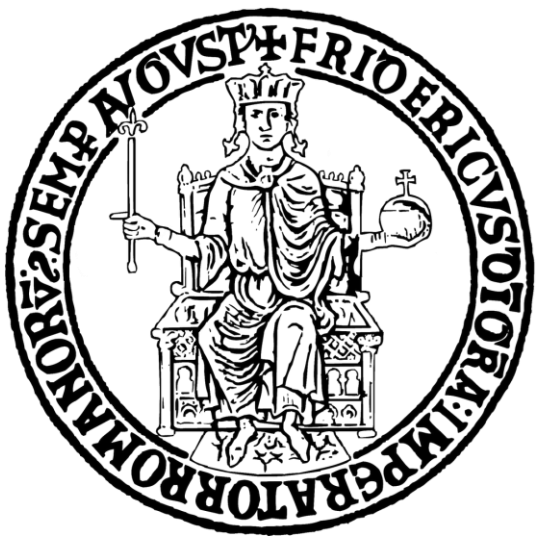
AVGVST FRIDERICVS DEI GRA IMPERATOR ROMANORVM SEMP

Chapter 3

NaTech multi-hazard risk assessment

È buona regola, quando ci si trova di fronte a un problema da risolvere, chiarirne prima di tutto i termini e poi decidere quale strategia sia più adeguata alla sua soluzione.

Rita-Levi Montalcini

Natural phenomena can have a strong impact on industrial plants endangering the environment and human life. A natural event may be the cause of technological accidents leading to the dispersion in the environment of toxic or highly flammable substances. In the industrial field, technological accidents due to natural events are called NaTech events [89] and can be associated with structural damage at the industrial unit or to the detachment of pipelines. Following a NaTech event, content release may provoke explosions, pool fire or toxic dispersions that trigger a series of cascading effects leading to an escalation of unpredictable accidents.

In this thesis, risk assessment is evaluated as the mean annual frequency of industrial accidents that may lead to potential fatalities after a natural event [90]. *QRA* were developed in literature [89,91] to provide information about the spatial and temporal distributions of potential fatalities as exposition of thermal radiation, concentration of toxic substances, explosions due to overpressures. *QRA* procedure allows to evaluate the consequences of a NaTech event in terms of human and economic losses, simulating escalation scenarios [92].

The state-of-the-art presents *QRA* developed considering the hazard related to only one natural event. Examples are the works of [93] on floods or [94,95] on the earthquakes. Other works, instead, as [58], evaluate the risk as the exceedance probability of a damage limit state at which the industrial unit is prone during the specific natural event, in a certain return period, at the site of interest.

The novelty of this study is to carry out a multi-hazard risk analysis for NaTech scenarios, focusing on cascading hazard of tsunamis triggered by earthquakes. Several authors discuss of multi-risk assessment due to cascading hazard, e.g. [96,97]. Other authors, instead, propose methodologies of multi-risk to take into account the link between different hazards, e.g. [98–101]. Three are the main points of the multi-risk framework: the joint probability of hazards, time-variant multi-hazard dependent vulnerability, and combination of losses from different hazards in a coherent manner [102].

Tsunamis have a low probability of occurrence but high impact in terms of structural damage and thus in terms of economic losses [103,104]. In this context, the risk can be analysed under different aspects: or considering two natural events separately, or the interaction between them. Herein, it will talk about of seismic risk when an earthquake occurs near the site without to trigger tsunami; and tsunami risk when an earthquake from a far source triggers tsunami that leads to damage at site.

The consolidated procedure to evaluate the risk starts with the identification of the hazard at the site of interest, and the vulnerability of the structures taken into consideration. These steps of risk analysis should be followed for each hazard, considered separately, to obtain the mean annual frequency of events that cause the release of content after structural damage. To have a complete view of the multi-risk, also consequences analysis should be developed, including simulations of the dispersion of the hazardous substances in the industrial area with the corresponding cascading effects, but this falls outside from the scope of this study. Then, also an expected losses analysis could be carried out, following the approaches to existing literature, e.g. [102,105–107] . In this way, the risk analysis is complete and allows to take decisions if the risk can be tolerated or if measures of risk reduction are required.[90]

The object of this chapter is to perform a risk analysis for a tank farm of 12 tanks supposed all squat, located along the coast of Milazzo. Thus, this chapter is structured as follows: first paragraph describes risk analysis methodology; in the second paragraph, the risk results are presented considering two natural events separately, while third paragraph discusses of contemporary failure of tanks; lastly, fourth paragraph shows a framework on the evaluation of the losses considering the interaction of two natural events; some conclusive remarks are finally given in section five.

3.1 Multi-hazard risk assessment methodology

The multi-risk analysis is performed for a case study of hypothetical oil refinery of only anchored atmospheric storage tanks when are subjected to ground shaking and/or to tsunami impact. The framework to follow for the risk analysis focuses on two main points: the knowledge of the hazard of the site of interest and the vulnerability of the structures examined. The seismic and tsunami hazard analyses are based on probabilistic approaches providing as results the hazard curves that express the variation of selected intensity measure (im) versus the exceedance rate, that is mean annual number of events that exceed a defined threshold im. The structural vulnerability, instead, aims to investigate the response of the tank to different levels of im following also in this case a probabilistic approach. The results of the vulnerability analysis are the fragility curves that express the probability of failure of structure to reach or exceed a specific level of damage under different levels of im. In this context, the failure is intended as the structural damage or the detachment of the pipeline causing the release of liquid content. The multi-risk analysis ends with the assessment of the structural failure rate intended as the mean annual number of events that cause the failure of the tank. The failure rate is obtained as integral of the hazard and the vulnerability.

3.1.1 Case study

Multi-hazard risk analysis is performed for the case study of a group of 6 tanks installed at Milazzo, at the North-East tip of Sicily (Italy), located to the Thyrrenean coast. The position on map of the petrochemical plant is shown in Figure 3.1-a) with a triangle. Panel a) shows the map of the bathymetry in terms of mean depth of sea level around the site of interest (data from [108]). The map shows that near the coast where the site is located, the bathymetry has depths up to $1000\ m$. The bathymetry allows to have information on the propagation effects of the tsunami wave, in terms of height and velocity. In addition, also the seabed features influence the wave propagation so much that earthquakes with magnitude relatively small could trigger abnormal tsunamis [109]. The oil refineries

are exposed to tsunami hazard because, typically, are built at few steps from the shore. In fact, panel b) shows the position of the system of 6 storage tanks taken into consideration for the risk analysis. It can be seen that they are very close to the shore, in fact, the tank with an identifier number (ID) “1” is located at a distance to the shore of 100 m, and the tank number 2 has a distance of 200 m, while the distance between them is about 20 m. The other tanks from the 4 to 6 number have about the same distance from the shore of 200 m, while the distance between them is about 10 m. All the plant is characterised by a sea level altitude and a site condition with a shear wave velocity assumed equal to $270\ m/s$. Generally, each tank is inside of catch basin, useful to collect the liquid that leaking from a damaged tank. This is practical solution to reduce the risk of industrial accident. All examined tanks are cylindrical steel shell structures, anchored at the base and resting on concrete foundation mat. This support condition is generally recommended in seismic zones. In addition, these tanks are equipped of a floating roof that moves along the height of shell following the filling level. One of the functions of the floating roof is to limit the movement of the liquid mass at the top avoiding sloshing phenomenon that may cause spillage of liquid in the connection between the roof and the shell; the other main feature is not to accumulate the gas under the roof that could be cause of explosions. The liquid contents typically are highly flammable substances as gasoil or fuel oil. The selected tanks have the same geometry, shown in Table 3.1. Thus, all tanks have almost the same dynamic response under seismic and tsunami action.

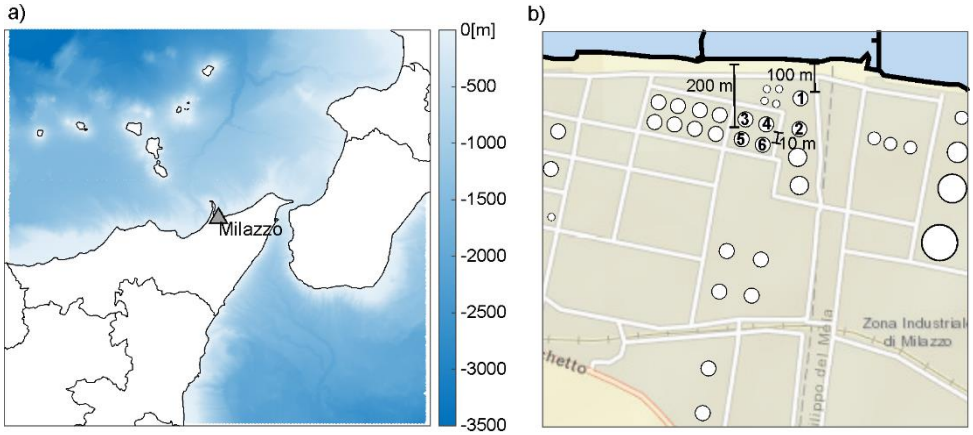

Figure 3.1: a) Bathymetry. b) Selected tanks for the case study.

Table 3.1: Geometrical features of the tanks of the case study.

Height	Diameter	Thickness wall	Thickness base plate	No. anchors	Diameter of anchors
$16\ m$	$55\ m$	$30\ mm$	$20\ mm$	120	$39\ mm$

3.1.2 Probabilistic multi-hazard analysis

The *PSHA* and *PTHA* are developed as discussed in the Chapter 1. For clarity, here, it is briefly summarized the main characteristics of the hazard analyses for the examined case study.

PSHA is performed for a circular area of $100\ km$ of radius from the site of interest, as shown in Figure 3.1-a). The earthquakes that occur in this area are both crustal and subduction. The part of the subduction that is inside the area of interest is the interface of the Calabrian Arc and it is depicted in figure as a dotted polygon. The intensity measure selected for the seismic hazard analysis is the peak ground acceleration *PGA*, thus the hazard curve is expressed in terms of the exceedance rate at varying *pga* threshold, $\lambda_{pga} = \lambda(PGA > pga)$. The hazard curve of the site is obtained by adding the exceedance rates of the two seismicity classes, this because the earthquakes occur both on the earth's crust and subduction

interface with a homogeneous stochastic Poisson process. Source models adopted for two seismicity classes are widely discussed in Chapter 1.

PTHA is taken from literature data of Volpe et al. 2019 [20]. This analysis is based on simulations of inundation scenarios of far- and near-field sources. Each simulation provides different registrations of tsunami height and velocity in each point of a refined grid. Figure 3.2-b) shown both onshore and offshore grid points, around the petrochemical plant. The figure shows the hazard map of the maximum height observed at return average period of $Tr = 300^{\cdot}000\ yr$. It is noteworthy that the grid does not cover the tanks far from the coast because of the influence of the tsunami is attenuated. The intensity measure chosen to carry out the *PTHA* is the maximum tsunami height, h_{wmax}. Thus, the tsunami hazard curves are expressed in terms of the exceedance rate of maximum tsunami height $\lambda_{h_w} = \lambda(H_{w,max} > h_{w,max})$ at varying of threshold h_{wmax}.

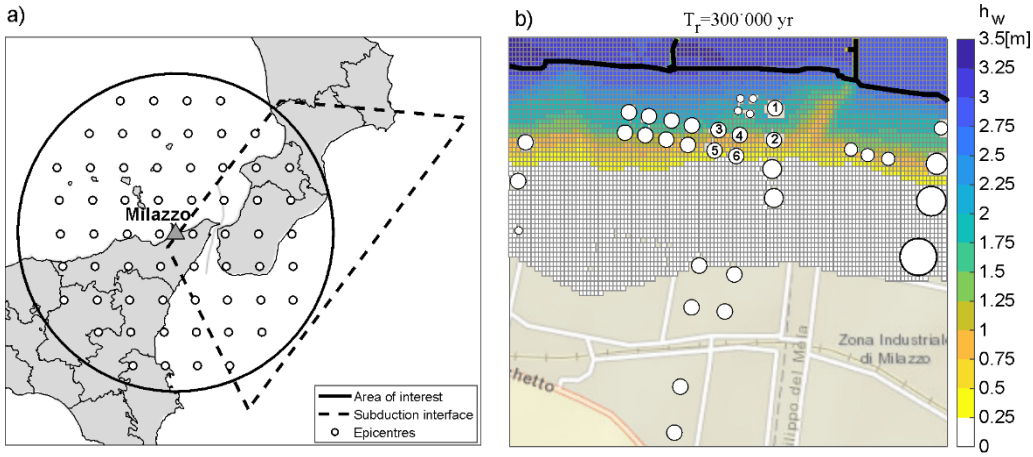

Figure 3.2: a) Examined area for PSHA. b) Hazard map in terms of height, for the tanks of the case study.

3.1.3 Fragility functions

The selected case study for risk analysis involves a vulnerability analysis for anchored atmospheric storage tanks subjected to both ground shaking and tsunami.

The dynamic response of the tank under tsunami action is different from ground shaking but, in both cases, depends mainly on the boundary conditions at the base and of dynamic behaviour of the liquid content. In fact, for the effect of the lateral accelerations due to an earthquake, a part of the liquid mass at the bottom of the tank responds with an impulsive motion, translating rigidly with the shell wall, while the other part in proximity of the free surface and in contact with the shell wall, in addition to translate laterally, moves upwards creating convective motions [110]. For the tsunami action, instead, the liquid mass does not move dynamically and responds with a hydrostatic pressure along the shell wall of the tank, in opposition to the external pressures [111]. These two different types of behaviour could take to several forms of damage. Typically, under seismic action, the shell wall can experience large meridional compressive stresses at the base causing large plastic deformations called elephant foot buckling, while in the upper zone, the convective motions can trigger sloshing phenomena provoking damage to the roof with consequent spillage of internal liquid. In addition, the base shear resulting by ground shaking could overcome the friction action, forcing the tank to slide. In this case, the failure of the tank is governed by possible detachment of the pipelines, and if the tank is anchored at the base, it is observed also the shear failure of the anchor bolts [112]. On the other hand, the tsunami acts along the shell wall with a hydrostatic pressure that triggers circumferential compressive stresses that may lead to elastic buckling of the shell wall, and with a hydrodynamic pressure that may induce sliding and/or overturning of the tank. The shell buckling is the most likely possible failure criterion that was observed from the analysis of past accidents triggered by floods events [51], that can be considered like tsunami inundation, with the consequence to lead to the structural collapse with instantaneous release of all liquid content. Another failure criterion regards to flotation of the tank due to Archimedes' force that acts on the base plate and is in opposite with the self-weight of the tank and the liquid content. This criterion becomes a concern when the tank is empty [65]. In this case, the anchorage system is put in tension, while the effect of the hydrodynamic force takes shear and moment. Thus, the anchorage system at the base is fundamental to reduce the occurrence of many of these failure phenomena helping the tank to resist better at the external actions, even if this constructive detail takes to an increase of the costs of facility.

To each structural failure mentioned above may be associated with a release of substances, that is the key issue for performing an *QRA*. Hence, the fragility functions are expressed in terms of structural damage that cause release of contents. The seismic fragility model adopted in this study is based on the literature work of Salzano, Iervolino and Fabbrocino 2003 [54]. The seismic fragility functions are obtained on the base of observation of past accidents and express the probability of failure given a certain threshold of *pga*. These empirical fragility functions are obtained from a dataset containing 532 observations of damage post-industrial accidents. A subset of these data provides information for this case study, in particular fragility functions are developed for anchored atmospheric storage tanks; for two filling levels, specifically, greater than 50% and near full; considering the cases in which the structural damage triggers rapid loss of content. No information is given on the influence of the slenderness ratio on the fragility functions; thus, the curves can be used for tanks with different geometries. The seismic fragility model is characterized by a log-normal cumulative density function (*cdf*) with median (μ) and standard deviation (β) reported in Table 3.2. From historical analysis of seismic damage on storage tanks, catastrophic failures occur with a grade of filling level greater than of 50%, because fundamentally the damage is associated with movement of liquid mass, thus, in condition of almost empty tank, it can be assumed that the fragility model returns nulls probabilities of failure at varying of *pga* thresholds.

Table 3.2: Median (μ) and standard deviation (β) of log-normal distributions for different filling level conditions [54]**.**

Filling condition	μ	β
Near full	1.25	0.65
Half full	3.72	0.8
Empty (assumed)	0	0

The choice to use seismic empirical fragility curves does not allow to carry out evaluations about the optimal seismic intensity measure. The intensity measure assessment depends strongly on the available information coming from examined database. In this case, the fragility curves adopted were developed considering the observed damage to

storage tanks during occurred major earthquakes from 1993 to 1995 [113]. Detailed information was not always available, especially for the oldest events, about the heights, diameters, wall thickness and fluid levels at the time of the earthquake, and this aspect does not allow to evaluate the vibration period of the structures. Another discussion point concerns the documentation about the seismological and geological aspects of the earthquakes. For many events of this database, or only values of PGA are available, or macroseismic intensity observations are used for reconstructing shaking distributions, always in terms of PGA, in the absence of instrumentally recorded data.

Of course, the use of an intensity measure closest to the dynamic of the system could be much more suitable to describe the behaviour of the structure under seismic action, but this discussion can be done only for fragility curves developed analytically. In fact, from the work of Luco and Cornell [114], the optimal intensity measure allows to have a structural response independent from seismological parameters as, for example, magnitude and distance. According to Bakalis at al. [58], the PGA value or the spectral acceleration at the impulsive period, are two reasonable choices because typically the impulsive period is relatively short. On the other hand, the convective response can only be captured in correspondence of convective spectral acceleration that is referred to a long period, sometimes also greater than $4\,s$. This can be view in Appendix where the seismic design is developed.

Tsunami fragility functions, instead, are widely discussed in Chapter 2 and briefly recalled here. The tsunami fragility functions are derived from analytical models based on static nonlinear elastic analysis on finite element models. These models take into account the interaction of failure criterions mentioned above developing parametric models distinguished for each failure mechanism based all on Weibull distribution. Both effects of the velocity and height of wave are investigated. In fact, these fragility models consider the tsunami load acting on the tank as a quasi-static pressure, so to distinguish the contribution of the hydrostatic component from the hydrodynamic one, following the approach of ASCE 7-16 [46]. The fragility curves are developed choosing as intensity measure the maximum tsunami height and, as well as the seismic case, are obtained for given filling level.

Since, the filling level is unknown when an earthquake or a tsunami hit a storage tank, for this reason, can be treated as a *RV*. The assumption is that the filling level is expressed by a uniform *RV*. In more detail, Eq. (3.1) expresses the fragility function independent from the filling level for the seismic case.

$$P\left[F \mid pga\right] = \sum_{i=1}^{3} P\left[F \mid PGA = pga, \Psi = \psi_i\right] \cdot P\left[\Psi = \psi_i\right] \tag{3.1}$$

Where $i = 1,2,3$, indicating three cases of filling considered for seismic fragilities, in particular $i = 1$ is the case of empty tank; $i = 2$ is half full tank; and $i = 3$ is the near full tank. ψ is the value of the percentage of filling level; and $P[\Psi = \psi]$ is the probability to have a filling level Ψ equal to ψ, uniformly distributed. $P[F|PGA = pga, \Psi = \psi]$ is the probability of failure conditioned to filling level, obtained from Salzano, Iervolino and Fabbrocino 2003 [54].

For tsunami case, the equation that describes the independence of the probability of failure from the filling level is Eq. (3.2).

$$P\left[F \mid \Phi\right] = \int_{10\%}^{100\%} P\left[F \mid \Phi, \Psi\right] \cdot f_{\Psi}\left(\psi\right) \cdot d\psi \tag{3.2}$$

This equation is expressed through an integral because the fragility curves are derived from analytical solutions. The lowest limit of the integral is set on 10% because a minimum operative filling level should always be guarantee. The tank is never completely empty. $P[F|\Phi, \Psi]$ is the probability of failure conditioned to filling level, evaluated as Eq. (2.12) and $f_{\Psi}(\psi)$ is the uniform probability density function of the filling levels.

3.1.4 Structural failure rate

The risk is evaluated in terms of structural failure rate λ_f that is the mean annual number of events that lead to the structural damage followed by release of contents. Failure rate is defined as the integral of the product between the fragility curve $P[F|im]$, and the absolute value of the

differential of the hazard curve $|d\lambda_{im}|$. This integral is expresses by Eq. (3.3):

$$\lambda_f = \int_{-\infty}^{+\infty} P[F \mid im] \cdot |d\lambda_{im}| \tag{3.3}$$

The structural failure rate evaluated in this way is referred at individual tank supposed isolated.

3.2 Results of multi-hazard risk analysis

3.2.1 Results of hazard and vulnerability analysis

Figure 3.3 shows the results of probabilistic hazard analysis for the seismic and tsunami cases. For the seismic case, panel a), only one curve defines the hazard to the site of interest, instead, for tsunami case, panel b), the hazard changes point by point. Each tsunami hazard curve is signed by a number that indicates the corresponding tank inside the map in panel b). The grid points corresponding to hazard curves are chosen as the nearest point to tanks side sea front. These points are depicted in figure with red square markers. As expected, the closest tanks to the coast exhibit exceedance rates greater than of these ones further away; and tanks located behind other tanks are shielded by these ones and presenting exceedance rates smaller than those ones in front. It can be concluded that the most exposed tanks to tsunami action are those ones the closest to the coast.

Comparing the seismic and tsunami occurrence rates, it is observed that $\lambda(PGA > 0\ g) = 2 \cdot 10^{-1}\ yr^{-1}$ is some orders of magnitude greater than the greatest tsunami occurrence rate, that is equal to $\lambda(H_{w.max} > 0\ m) = 1 \cdot 10^{-4}\ yr^{-1}$.

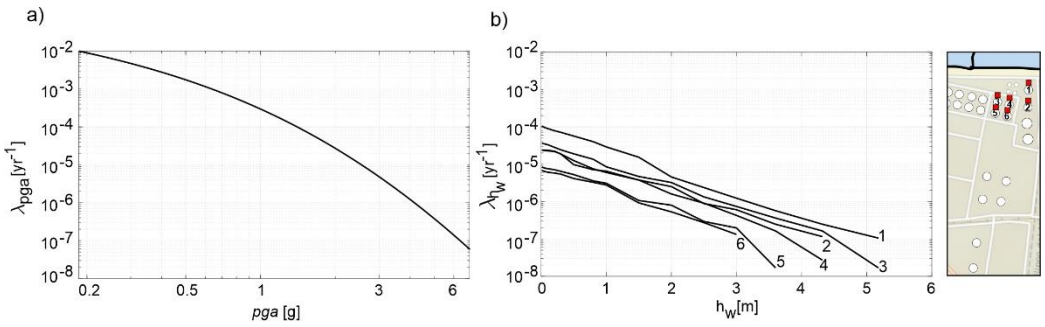

Figure 3.3: a) Seismic hazard curve. b) Tsunami hazard curves for the tanks inside map.

Figure 3.4 shows the fragility curves for the seismic case in panel a) and for tsunami case in panel b). Both panels depict with dotted lines the fragility curves conditioned by a certain filling level; while the continuous lines are fragility curves with a filling level assumed as a

uniform *RV*. For the sake of comparison, the figure shows the tsunami fragilities only for the filling levels considered for the seismic case, but these can be derived for any degree of filling because are obtained following an analytical approach.

The results of vulnerability analysis show that the behaviour of a tank under seismic action is completely different from the behaviour under tsunami action. As discussed in previous sections, the influence of the filling level is a crucial aspect in the evaluation of the fragility functions. Indeed, seismic fragility functions (panel a) show that the probability of failure for given *pga* value, is greater for the case of near full tank rather than half full or almost empty case. On the other hand, the behaviour under tsunami action is completely the contrary. Tsunami fragility curves in panel b) show that an almost empty tank has a probability of failure greater than full tank, for given percentage of submersion.

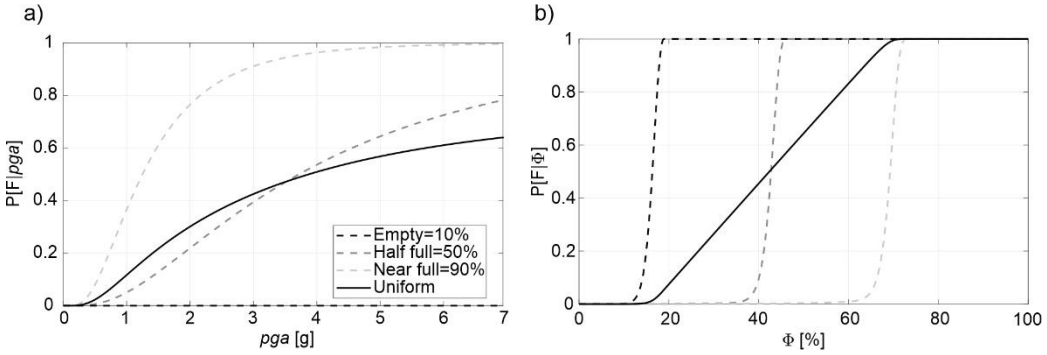

Figure 3.4: a) Seismic fragility functions. b) Tsunami fragility functions.

3.2.2 Results of structural failure rates

In this section, structural failure rate is evaluated for each tank of case study considering separately the seismic and tsunami action. Risk analysis is carried out considering different configurations of degree of filling, in particular focusing on the cases of almost near and half full; uniform distribution of filling level; and only for tsunami, the case of almost empty tank, because this condition for the seismic case provides null failure rates. Table 3.3 shows the numerical values of seismic $(\lambda_{f,S})$ and

tsunami $(\lambda_{f,T})$ failure rates for the 6 tanks considered for the analysis. The seismic failure rates are the same for all tanks because the seismic hazard is the same for all points of the area of interest.

The results of this risk analysis confirm what was discussed in the section of the fragility functions. The influence of the filling level on the risk moves in opposite direction for two natural events, in particular, the failure rate increases with the filling level for the seismic case, vice versa, for tsunami. It is observed that for this specific site, for fixed filling level, the seismic failure rates are some orders of magnitude greater than the corresponding tsunami failure rates. An explanation of this result can be linked to the hazard at the site, with the seismic hazard predominant on the tsunami hazard. The influence of the hazard at the site has an impact also on the tsunami failure rates of different tanks. More in detail, the tanks near the coast have a tsunami failure rate greater than of tanks far from the coast.

Table 3.3: Structural failure rates for seismic and tsunami action for different configuration of filling levels.

ID	$\lambda_{f,S}\ [yr^{-1}]$			$\lambda_{f,T}\ [yr^{-1}]$			
	Near full	Half full	Uniform distribution	Near full	Half full	Almost empty	Uniform distribution
1	5.45E-04	6.82E-05	1.70E-04	3.93E-10	3.26E-09	2.85E-06	2.20E-07
2				1.20E-10	9.77E-10	1.16E-06	7.93E-07
3				2.33E-10	1.77E-09	1.75E-06	1.46E-07
4				1.08E-10	8.87E-10	1.03E-06	7.34E-08
5				3.67E-11	3.15E-10	3.97E-07	2.48E-08
6				1.66E-11	1.62E-10	1.97E-07	7.08E-08

3.2.3 Comparison of tsunami failure rates with the literature results

The object of this section is to compare the tsunami failure rates derived from analytical fragility functions obtained from Chapter 2 with the tsunami failure rates evaluated with the tsunami fragility function of literature work of Basco and Salzano (2016) [56] expressed in terms of

maximum momentum flux. This comparison is possible thanks to the results of the work of Volpe et al. (2019) [20] that provide hazard curves both maximum tsunami height and maximum momentum flux.

As case study, three archetype tanks of Chapter 2 are taken into consideration, assuming them located at position of the tank shown in the top right corner of the panel a) of Figure 3.5. The hazard curves considered for the risk assessment are shown in Figure 3.5, in particular, panel a) shows the tsunami exceedance rates in terms of maximum tsunami height and panel b) in terms of maximum momentum flux λ_{mf}.

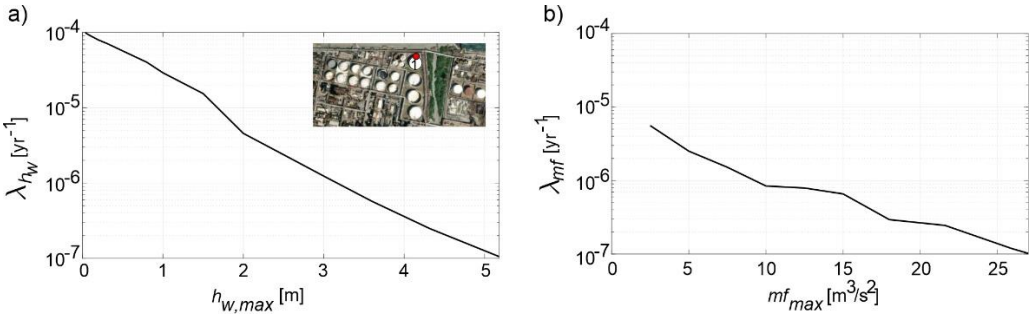

Figure 3.5: Tsunami hazard curves in terms of a) maximum tsunami height, and b) maximum momentum flux [20]**.**

Basco and Salzano (2016) [56] evaluate the tsunami fragility functions for 115 tanks with different geometries. Three of these tanks are chosen with similar geometry to the archetypes. Fragility models are based on log-normal cumulative density functions. Table 3.4 shows the geometries, the median value $\mu_{log(MF_{max})}$ and standard deviation $\sigma_{log(MF_{max})}$ of the logarithm of the momentum flux of selected tanks.

Table 3.4: Geometry features of selected tanks from database of Basco and Salzano (2016) and corresponding log-normal distribution parameters of fragility function [56]

D [m]	H [m]	t_W [mm]	$\mu_{log(MF_{max})}$	$\sigma_{log(MF_{max})}$
10.5	9	8.4	2.60	0.48
24	12.6	12.5	3.00	0.50
48	7.20	12.5	2.30	0.50

The tsunami failure rates derived from Basco and Salzano (2016) $\lambda_{f,Basco}$ and from parametric model of Section 2.3.3 are given in Table 3.5. The results show that the tsunami failure rates do not present large differences.

Table 3.5: Comparison between tsunami failure rates evaluated with fragility function of Basco and Salzano (2016) [56] **and analytical fragility of Chapter 2.**

	$\boldsymbol{\lambda_{f,Basco}}$ $[\boldsymbol{yr^{-1}}]$	$\boldsymbol{\lambda_{f,T}}$ $[\boldsymbol{yr^{-1}}]$
Slender	$6.79 \cdot 10^{-7}$	$2.17 \cdot 10^{-7}$
Intermediate	$3.12 \cdot 10^{-7}$	$4.00 \cdot 10^{-7}$
Squat	$1.14 \cdot 10^{-6}$	$8.09 \cdot 10^{-7}$

3.3 Cascading effects

Another aspect to take into account in NaTech risk assessment is the possibility to evaluate the domino effect due to the release of content. The loss of content may be cause of an explosion, pool fire, or delayed explosions of a vapour cloud. The industrial accidents of a unit may trigger further accidents at another unit, and so on, triggering cascading effects. A measure of evaluation of the escalation of these NaTech events can be in terms of number of victims at following of cascading effects or the probability that a unit *j* can loss content due to an event at the initiating unit *i* [89]. The probability of loss of containment of the unit *j* is dependent from the distance to the initiating unit *i*. The evaluation of the dispersion or propagation of the NaTech event are treated for the *QRA* that falls outside from the scope of this thesis. The objective of this section, instead, is to provide tools to carry out the loss analysis due to the domino effects. Thus, risk assessment for simultaneous failure of a group of the tanks will be discussed.

3.3.1 Simultaneous failure framework

The probability to observe the loss of content after a natural event of exactly k tanks on n totals, is expressed through the sum of n Bernoulli *RVs*. In fact, the random variable, loss of content, can have only two realizations: occurred or not occurred. The loss of content, in this context, represents the failure of the industrial unit. The event, k failed tanks and $n-k$ not failed tanks, sorted in a specific sequence, has a probability equal to the product of the probability of failure and not failure associated with each tank in a specific combination, given the stochastic independence of random variables.

The sum of n Bernoulli *RVs*, s-independent, is a Binomial *RV* if the parameter probability of failure is common to all tanks [115]. This happens for the seismic case, under the assumption that *similar* tanks are clustered together close enough to preclude variability in the shaking intensity that they experience in a single event. Therefore, the probability that k tanks fail simultaneously, $P[F_k|pga]$, is evaluated by Eq.(3.4):

$$P\left[F_k \mid pga\right] = \binom{n}{k} \cdot \left(P\left[F \mid pga\right]\right)^k \cdot \left(1 - P\left[F \mid pga\right]\right)^{n-k}; \quad k = 0,1,2,...,n \quad (3.4)$$

The failure rate of exactly $N = k$ tanks can be determined by Eq.(3.5):

$$\lambda_{f,S}(N = k) = \int_0^{+\infty} P\left[F_k \mid pga\right] \cdot \left|d\lambda_{pga}\right| \quad (3.5)$$

For the tsunami case, the structural failure rate of exactly $N = k$ tanks, can be evaluated by Eq. (3.6):

$$\lambda_{f,T}(N = k) = \nu_T \cdot P\left[F_k \mid T\right] \quad (3.6)$$

where ν_T is the tsunami occurrence rate, that is the mean number of tsunamis that occur in one year at the site of interest; and $P[F_k|T]$ is the probability of failure of exactly $N = k$ tanks conditional to tsunami occurrence. This equation is another way to write the failure rate expressed by Eq. (3.3) and can be also used to evaluate the probability of failure, given tsunami event, of an individual tank, $P_{f|T}$, as Eq.(3.7):

$$P_{f|T} = \frac{\lambda_{f,T}}{\nu_T} \quad (3.7)$$

The numerator, $\lambda_{f,T}$ is the tsunami failure rate of an individual tank evaluated by Eq.(3.3).

$P[F_k|T]$ is the sum of n Bernoulli random variables, s-independent, with parameter $P_{f|T}$ that is different tank by tank. Thus, this probability can be evaluated through Eq. (3.8) as:

$$P[F_k \mid T] = \begin{cases} \prod_{s=1}^{n}\left(1 - P_{f|T}\left(id_s\right)\right) & \text{for } k = 0 \\ \sum_{i=1}^{\binom{n}{k}}\left[\prod_{j=1}^{k} P_{f|T}\left(u_{i,j}\right) \cdot \prod_{z=1}^{n-k}\left(1 - P_{f|T}\left(\bar{u}_{i,z}\right)\right)\right] & \text{for } k = 1,2,\ldots,n-1 \\ \prod_{s=1}^{n} P_{f|T}\left(id_s\right) & \text{for } k = n \end{cases} \tag{3.8}$$

where $ID = \{id_1, \ldots, id_n\}$ is the vector containing the identification number of all tanks as the first column of Table 3.3; and id_s with $s = 1,2, \ldots, n$ indicates the elements of the vector ID. $P_{f|T}(id_s)$ is the probability of failure of the tank id_s given event. U is the matrix of the of ID combinations of failed tanks, with number of rows equal to the number of combinations given by binomial coefficient, $\binom{n}{k}$, and number of columns equal to the number of tanks failed. The generic element of U is u_{ij}, in which the subscripts $i = 1,2, \ldots, \binom{n}{k}$ indicate the row of U; and $j = 1,2, \ldots, k$ indicates the column of U. $\bar{U}$ is the matrix of the of ID combinations of not failed tanks, with number of rows equal to the number of combinations given by binomial coefficient, $\binom{n}{k}$, and number of columns equal to the number of tanks not failed. The generic element of the matrix $\bar{U}$ is $\bar{u}_{iz}$, in which the subscript $z = 1,2, \ldots, (n-k)$ indicates the column of $\bar{U}$. $P_{f|T}(u_{i,j})$ is the probability of failure of the tank in the position of the element i,j of the matrix U, given event. $P_{f|T}(\bar{u}_{i,z})$ is the probability of failure of the tank in the position of the element i,z of the matrix $\bar{U}$, given event.

More specifically, Table 3.6 shows an example the matrices U and $\bar{U}$ for $k = 5$ and $n = 6$.

Table 3.6: To the left: matrix of the ID combinations of k failed tanks out of n total tanks. To the right: matrix of the ID combination of $(n-k)$ not failed tanks out of n total tanks.

$U_{i,j}$	ID				
combinations	1	2	3	4	5
	1	2	3	4	6
	1	2	3	5	6
	1	2	4	5	6
	1	3	4	5	6
	2	3	4	5	6

$\overline{U}_{i,z}$	ID
combinations	6
	5
	4
	3
	2
	1

The rate of contemporary failure of k tanks out of n can be evaluated considering the occurrence of both events in a small interval time. This is a simple way to consider the interaction of two events, and it can be considered a simple application of multi-risk assessment. Thus, the contemporary failure rate of exactly k tanks out of n at following of seismic and tsunami actions that happen almost at the same time, $\lambda_{f,E}$, can be evaluated as Eq.(3.9):

$$\lambda_{f,E}(N=k) = \lambda_{f,S}(N=k) + \lambda_{f,T}(N=k) \tag{3.9}$$

3.3.2 Results

The rates associated with contemporary failure of exactly k tanks out of n , for varying k , are shown in Figure 3.6, where panel (a) shows the structural failure rates considering two natural events separately while panel (b) shows the results considering the interaction of two events. The case study taken in consideration is represented by 6 tanks of Figure 3.3. When k assumes a value of 0 means that no tanks failed, while for k equal to 6, all tanks are failed. From panel (a), the failure rates due to earthquakes are some orders of magnitude greater than those due to tsunami and this difference is more evident when k is increasing. For k greater than 3, the tsunami failure rates become less than $10^{-12}\ yr^{-1}$ assuming values too low to show on the same plot. This result implies that the sum of the rates, for the multi-risk analysis shown in panel (b), implies rates that are like the seismic failure rates. The root cause of this result

can be associated with a substantial difference of the two hazards at the site of interest.

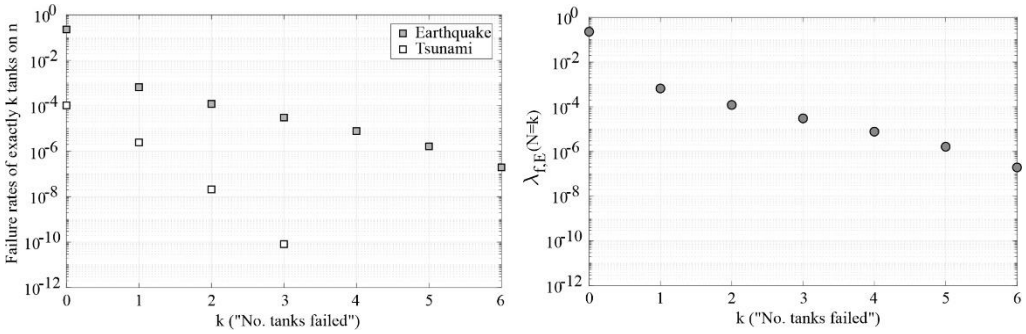

Figure 3.6: a) Failure rates of exactly k tanks out of n. b) Failure rates of exactly k tank out of n considering the sum of seismic and tsunami failure rates.

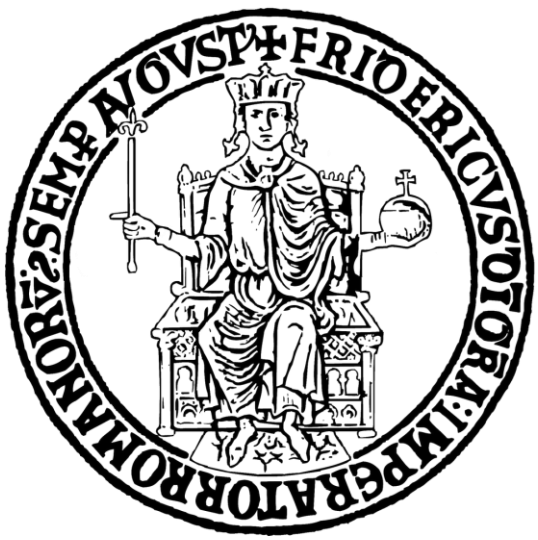
AVGVST FRIDERICVS DEI GRA IMPERATOR ROMANORVM SEMP

Chapter 4

Conclusions

Chi è sempre prudente non arriva mai primo. Io intendo giocare e vincere. È una follia? Farò il pazzo tutta la vita.

Diego Armando Maradona

The thesis presents a NaTech multi-hazard risk assessment for a petrochemical plant located in Southern Italy, comprising mainly anchored atmospheric storage tanks exposed to seismic and tsunami actions. The risk is measured in terms of structural failure rate, that is the mean annual number of natural events that cause structural damage at an industrial liquid storage unit with consequent release of its contents. To carry out risk assessment, hazard and vulnerability analysis are implemented considering two natural events separately. More specifically, probabilistic seismic hazard analysis and tsunami vulnerability of tanks are the main results of this study, while probabilistic tsunami hazard analysis and seismic vulnerability of tanks are taken from existing studies in the literature.

The hazard at the site is expressed in terms of exceedance rate, that is the mean annual number of events that have an intensity greater than a certain threshold. The intensity measure chosen for seismic hazard is the *PGA*. The *PSHA* is developed with the classical approach of hazard integral, taking into consideration uncertainty in finite fault geometry and also two different seismicity classes: crustal and subduction earthquakes. Inside the seismic hazard results, it needs to take into considerations of some limitations of the subduction source model. Specifically, the subduction rupture scenarios are not simulated, and the seismic events

are modelled only with the corresponding hypocentres. This allows to consider only the hypocentral distance as site-source distance, while the Abrahamson's GMPE is implemented with the closest distance of the site from the rupture. This limitation, therefore, leads to approximated values of the exceedance probability given magnitude and distance site-source of the hazard integral.

PTHA was available in literature for this site considered for the case study, providing exceedance rates for each point, on- and off-shore, of a refined grid around the petrochemical plant. That analysis had been carried out though inundation simulations, providing time histories of tsunami height and flow velocity. The intensity measure chosen for the hazard analysis is maximum tsunami height. The hazard results show that the exceedance rates decrease moving away from the coast. The results of *PTHA* are used to develop models of conditional tsunami hazard. Conditional hazard consists in developing conditional probability density functions of secondary intensity measures given a value of the primary intensity. This analysis has allowed to obtain a joint probability density function of maximum momentum flux and flow velocity, conditional to a value of maximum height. This result was subsequently used to evaluate the probability of failure of the storage tanks under tsunami action.

A crucial point in NaTech risk quantification is the evaluation of vulnerability of industrial facilities. The results of vulnerability analysis are the fragility curves that express the probability of failure given various values of an appropriate intensity measure. Failure in this context is defined as structural damage that leads to content release, which can correspond to more than one damage mechanism, each with its own failure criterion. Because each failure criterion is governed by different hazard parameters, several intensity measures were considered, and conditional hazard models were used.

The tsunami fragility functions are the main result of this work of thesis. The probability of failure is evaluated for anchored storage tanks under tsunami action considering the combined effects of hydrostatic and hydrodynamic forces that may lead to shell buckling or rupture of the anchorage system under tension or shear, with consequent of flotation, sliding or overturning of the tank. In this context, three archetype tanks with different aspect ratios are designed according to Eurocodes and

modelled with finite element method. Static nonlinear analyses are carried out for different levels of internal liquid, tsunami height and velocity. The fragility curves obtained from structural analysis are then fitted with a parametric model. The results highlight that the fragilities are influenced by the filling level, which causes the governing failure mechanism for each tank geometry to vary.

The seismic and tsunami risk quantification is evaluated for a group of 6 squat tanks located in different positions along the coast. Considering an individual tank, it is observed that the failure rate for seismic action increases with the filling level, while the opposite trend is observed for the tsunami case, in which the failure rate decreases as the tanks are progressively fuller. Only for the tsunami case, the position of the tanks influences the failure rates that decrease for tanks far from the coast. In addition, risk analysis is carried out considering the contemporary failure of a given number of tanks and it is resulted that the failure rates obtained for the seismic case are some orders of magnitude greater than of ones for the tsunami case. This result highlights that for this site, examined for the case study, the tsunami risk is smaller than that attributed to ground shaking. An explanation of this result is due to the high difference of the two hazards for this specific site. The work of thesis gives a contribution for a more accurate evaluation of the NaTech risk, providing also insights useful in the context of a multi-hazard *QRA* for industrial plants.

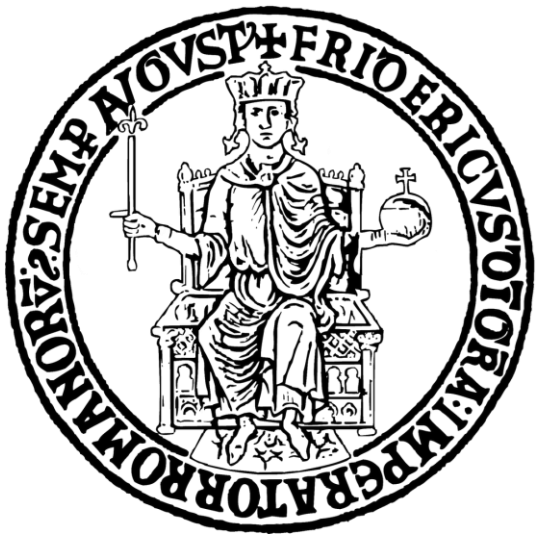
AVGVST FRIDERICVS DEI GRA IMPERATOR ROMANORVM SEMP

Appendix A: Design of anchored atmospheric storage tanks

The object of this appendix is to describe the procedures for the design of the thicknesses of the shell wall and the base plate and the diameter and number of the anchor bolts for the archetype tanks. The design is carried out according to European standards, but also following some requirements of the American standards.

These anchored tanks are designed to resist to wind and seismic actions. The external actions are applied on finite element models on which static nonlinear analyses are carried out. Nonlinearity considered for the design phase is limited to the contact issue at the edge of the annular plate, while material behaviour remains linear-elastic.

5.1 Wind action.

The reference standards adopted for the evaluation of the wind action for circular cylinders are:

-Eurocode 1: Actions on structures – General actions – Part 1-4: Wind actions. (EC1-1-4) [76].

-Norme tecniche per le costruzioni. (NTC2018) [41].

As support of these standards, a document published by the Italian national research council (consiglio nazionale delle ricerche; CNR)[116], collects information from the above standards.

5.1.1 Evaluation of external pressions acting on the circular cylinders

The aerodynamic behaviour of the structures with circular base is focused on the height-diameter ratio, H/D, Reynolds number, Re, and the roughness of the lateral surface, k. The wind pressure acting on the external surface, can be evaluated according to EC1-1-4 as Eq. (5.1):

$$w_e = q_p(H) \cdot c_{pe} \tag{5.1}$$

where $q_p(H)$ is the peak velocity pressure evaluated at an altitude of reference H tank height, and c_{pe} is the external pressure coefficient. The wind pressure is uniform along the height of the structure.

The peak velocity pressure $q_p(H)$ is evaluated according to Eq. (5.2) and it is expressed in $[N/m^2]$:

$$q_p(H) = \left[1 + 7 \cdot I_v(H)\right] \cdot \frac{1}{2} \cdot \rho \cdot v_m^2(H) \tag{5.2}$$

Where $\rho = 1.25\ kg/m^3$ is the air density; v_m is the mean wind velocity in $[m/s]$ at height H; and I_v is the turbulence intensity. The mean wind velocity v_m is expressed by Eq.(5.3):

$$v_m(H) = c_r(H) \cdot c_o(H) \cdot v_b \tag{5.3}$$

This velocity depends on the roughness factor $c_r(H)$; orography factor $c_o(H)$, taken equal to 1 for flat terrain; and the basic wind velocity v_b. Terrain roughness is evaluated with a relationship based on the logarithm velocity profile, as Eq. (5.4):

$$\begin{cases} c_r(H) = k_r \cdot \ln\left(\dfrac{H}{z_0}\right) & \text{for } z_{\min} \le H \le z_{\max} \\ c_r(H) = c_r\left(z_{\min}\right) & \text{for H} \le z_{\min} \end{cases} \tag{5.4}$$

Where z_0 is the roughness length; z_{min} and z_{max} are the height limits; and k_r terrain factor. z_{max} is equal to $200\ m$, while z_{min} and z_{min} are defined from the Eurocode depending on the terrain category. In the case of coastal structures where there are not obstacles to the wind the terrain

category is the *'0'* with $z_0 = 0.003\ m$ and $z_{min} = 1\ m$. k_r depending on the roughness length z_0 calculated using Eq. (5.5):

$$k_r = 0.19 \cdot \left(\frac{z_0}{z_{0,II}} \right)^{0.07} \tag{5.5}$$

Where $z_{0,II}$ is the height corresponding to the *'II'* terrain category equal to $0.05\ m$. The basic wind velocity v_b characterizes the windiness of the area where is located the structure and depends on the direction of the wind and season of the year and is evaluated at $10\ m$ above ground of terrain category II. Such velocity can be evaluated by Eq.(5.6):

$$v_b = c_{dir} \cdot c_{season} \cdot v_{b,0} \tag{5.6}$$

the coefficient of direction of the wind, c_{dir}, and the coefficient that takes into account the season of the year, c_{season}, can be assumed equal to 1 in absence of the statistical investigations. $v_{b,0}$ is the mean wind velocity evaluated in an interval time of 10 minutes, at $10\ m$ of height above the ground. This parameter is given by National annex that in this case is the NTC18 and depends on the region where the structure is located. For the Sicily, $v_{b,0} = 28\ m/s$.

The turbulence factor $I_v(H)$ is evaluated with Eq.(5.7):

$$\begin{cases} I_v(H) = \dfrac{1}{c_o(H) \cdot \ln\left(\dfrac{H}{z_0} \right)} & \text{for } z_{\min} \le H \le z_{\max} \\ I_v(H) = I_v\left(z_{\min}\right) & \text{for } H \le z_{\min} \end{cases} \tag{5.7}$$

While, the external pressure coefficient c_{pe} for circular cylinders can be determined from Eq.(5.8):

$$c_{pe} = c_{p,0} \cdot \psi_{\lambda\alpha} \tag{5.8}$$

where $c_{p,0}$ is the external pressure coefficient assuming the cylinder with endless length; $\psi_{\lambda\alpha}$ is a coefficient that takes into account of the length of the tank considering the end-effect. The $c_{p,0}$ varies according to α, the

clockwise angle between x-axis and the application point on the circumference of the tank, measured from the direction of the wind. $c_{p,0}$ is given by Eq.(5.9):

$$\begin{cases} c_{p,0}(\alpha) = 1 - \left(1 - c_{p0,\min}\right) \cdot \sin^2\left(\dfrac{\pi \cdot \alpha}{2 \cdot \alpha_{\min}}\right) & \text{for } 0° \le \alpha \le \alpha_{\min} \\ c_{p,0}(\alpha) = c_{p0,h} - \left(c_{p0,h} - c_{p0,\min}\right) \cdot \cos^2\left(\dfrac{\pi}{2} \cdot \dfrac{\alpha - \alpha_{\min}}{\alpha_A - \alpha_{\min}}\right) & \text{for } \alpha_{\min} \le \alpha \le \alpha_A \\ c_{p,0}(\alpha) = c_{p0,h} & \text{for } \alpha_A \le \alpha \le 180 \end{cases} \tag{5.9}$$

In this expression, α is expressed in [°]. α_{min} [°] is the angle where the minimum pressure acts; α_A[°] is the angle where the separation of the flux happens; $c_{p0,min}$ is the minimum coefficient of pressure and $c_{p0,h}$ is the coefficient of the base pressure. Typical values of these parameters are reported in the EN1991-1-4, and shown herein in Table 5.1, referred to a given value of the Reynolds number (Re) and for an equivalent roughness $k/D \le 5 \cdot 10^{-4}$. Where k is the roughness height that for surfaces of galvanised steel is equal to $0.2\ mm$.

Table 5.1: Typical values for the pressure distribution for circular cylinders for different Reynolds numbers.

$\boldsymbol{Re}$	$\boldsymbol{c_{p0,min}}$	$\boldsymbol{c_{p0,h}}$	$\boldsymbol{\alpha_{min}}$[°]	$\boldsymbol{\alpha_A}$[°]
$5 \cdot 10^5$	-2.2	-0.4	85	135
$2 \cdot 10^6$	-1.9	-0.7	80	120
10^7	-1.5	-0.8	75	105

The configuration of the flux is governed by Reynolds number defined as Eq.(5.10):

$$\mathrm{Re} = \frac{D \cdot v(H)}{\nu} \tag{5.10}$$

Where $\nu = 15 \cdot 10^{-6}\, m^2/s$ is the kinematic viscosity of the air; $v(H)$ is the peak wind velocity at the height H of the tank and defined as Eq.(5.11):

$$v(H) = \sqrt{\frac{2 \cdot q_p(H)}{\rho}} \tag{5.11}$$

Regarding to the end-effect factor, $\psi_{\lambda\alpha}$, this is given by Eq.(5.12):

$$\begin{cases} \psi_{\lambda\alpha} = 1 & \text{for } 0° \le \alpha \le \alpha_{\min} \\ \psi_{\lambda\alpha} = \psi_\lambda + (1 - \psi_\lambda) \cdot \cos\left[\frac{\pi}{2} \cdot \left(\frac{\alpha - \alpha_{\min}}{\alpha_A - \alpha_{\min}}\right)\right] & \text{for } \alpha_{\min} \le \alpha \le \alpha_A \\ \psi_{\lambda\alpha} = \psi_\lambda & \text{for } \alpha_A \le \alpha \le 180° \end{cases} \tag{5.12}$$

Where $\psi_\lambda = 2/3$ for structures with ratio $H/D \le 5$.

5.1.2 Results

In this section, the results of the wind design are shown. In Table 5.2, the peak velocity pressure at the reference height corresponding to the height of the tanks is evaluated.

Table 5.2: Peak velocity for three archetype tanks.

Tank	H $[m]$	$c_r(H)$	v_b $[m/s]$	$v_m(H)$ $[m/s]$	$I_v(H)$	$q_p(H)$ $[kN/m^2]$
Slender	10	1.27	28	35.44	0.12	1.46
Intermediate	13	1.31		36.59	0.12	1.54
Squat	16	1.34		37.49	0.12	1.59

While Table 5.3 shows the equivalent roughness and the Reynolds number. The values of k/D in table are all less than $5 \cdot 10^{-4}$, thus, the values of Table 5.1 can be used to evaluate the external pressure coefficient. The Reynolds numbers obtained are greater than the 10^7, that is the greatest value of Table 5.1. For this reason, for simplicity, the

evaluation of the external pressure coefficient is derived considering the values of Table 5.3 corresponding to $Re = 10^7$.

Table 5.3: Reynolds number for three archetype tanks.

Tank	k/D	$v(H)$ $[m/s]$	Re
Slender	$0.20 \cdot 10^{-4}$	48.37	$3.23 \cdot 10^7$
Intermediate	$0.08 \cdot 10^{-4}$	49.53	$7.93 \cdot 10^7$
Squat	$0.04 \cdot 10^{-4}$	50.52	$1.85 \cdot 10^8$

Figure 5.1 shows the external pressure at varying of the angle α for three tanks. The difference between pressure for given α value is not meaningful.

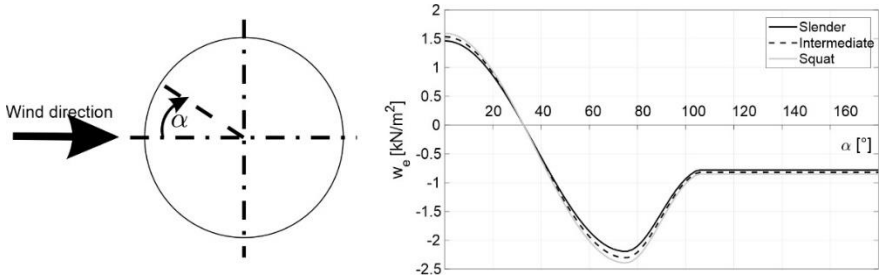

Figure 5.1: Wind pressure acting on the circumference of all tanks.

The distribution of the wind pressures along the shell of the tank is show in Figure 5.2.

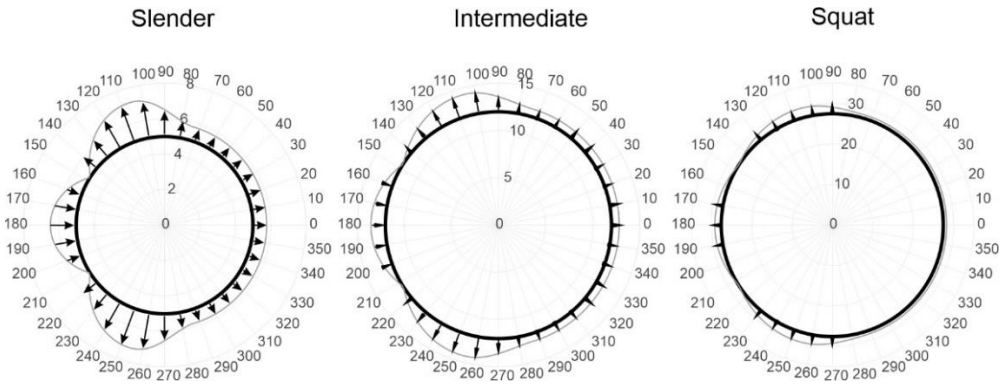

Figure 5.2: Wind pressure shape along the circumferences of three archetype tanks.

5.2 Seismic action

The design of seismic action is carried out following the prescription of Eurocode 8-4:2023 [117]. The seismic action derived from this Eurocode is compared with action evaluated with the previous version of the same Eurocode 8-4:2006 [68], that provides a simplified procedure for anchored tanks.

The behaviour of tank under seismic action depends mainly on the dynamic motion of the liquid content. In fact, for the effect of the lateral accelerations due to the earthquake, part of the liquid mass near the base of the tank moves rigidly with the shell wall, called impulsive mass, but at the same time, the upper part of the mass starts to move vertically giving rise to convective motions, and is called convective mass. The impulsive mass increases the inertial mass at the base of the tank, while the convective mass gives rise to sloshing phenomena that have oscillation period high, between 2 up to 6-10 seconds [118]. The portion of the impulsive and convective mass is determined from the ratio between height of the tank H and the radius R [119], in particular for slender tank (with $1 < H/R \leq 3$) the impulsive mass can reach also the 80% of the total liquid mass; contrary for squat tank (with $0.3 < H/R \leq 1$) is predominant the convective mass. For tanks with $0.3 < H/R < 3$ the first impulsive mode and the first convective mode move about the 85-98% of the total liquid mass of the entire tank [112]. The classical equivalent mechanic model used in literature is based on multi-degree of freedom with two masses attached to with springs and dampers at the shell wall of the tank that are supposed rigid [112]. The masses are referred to the impulsive and the convective mass associated with the first mode. The convective masses associated with higher modes contribute to no more than the 5% of the total action, thus can be neglected for the evaluation of the seismic action.

5.2.1 Evaluation of seismic action with EN1998-4:2006

For this analysis the tank is modelled as a two degrees of freedom system where the bottom mass is the impulsive mass, and the other is the

convective mass associated with the first mode. The response of the two masses is combined with the numerical sum.

The first step of the analysis is to determine the period of vibration of the structure due to the impulsive and convective mass, and are given by Eq.(5.13):

$$\begin{cases} T_{imp} = C_i \cdot \dfrac{\sqrt{\rho_f} \cdot H_{f,\max}}{\sqrt{\dfrac{t_w}{R}} \cdot \sqrt{E}} \\ T_{conv} = C_c \cdot \sqrt{R} \end{cases} \tag{5.13}$$

Where T_{imp} e T_{conv} are respectively the period of impulsive and convective mass; $H_{f,max}$ is the design liquid height corresponding to the maximum level of the liquid height; R is the radius of the tank; t_w is the wall thickness; ρ_f is the density of the liquid content; E is the Young's modulus of elasticity of the steel. The coefficient C_i and C_c are contained in Eurocode and shown in Table 5.4, for clarity, only the values referred to this case study:

Table 5.4: Parameters for the dynamic characterization of equivalent two degree of freedom system [68]**.**

	$\frac{H_{f,max}}{R}$	C_i [−]	C_c $[s/\sqrt{m}]$	$\frac{m_i}{m}$	$\frac{m_c}{m}$	$\frac{h_i}{h_{f,max}}$	$\frac{h_c}{h_{f,max}}$	$\frac{h_i'}{h_{f,max}}$	$\frac{h_c'}{h_{f,max}}$
Slender	2.0	6.21	1.48	0.763	0.237	0.448	0.751	0.500	0.764
Intermediate	1.0	6.36	1.52	0.548	0.452	0.419	0.616	0.721	0.785
Squat	0.5	7.74	1.74	0.300	0.700	0.400	0.543	1.460	1.517

In table, m_i, m_c, and m are the impulsive mass, the convective mass, and the total liquid mass. h_i and h_c are the heights of the centroid of the impulsive and convective hydrodynamic wall pressure; h_i' and h_c' are the height of centroid of the impulsive and convective hydrodynamic pressures on the wall and on the base plate. The values in table allow to evaluate the total base shear Q, the overturning moment above the base plate M and the overturning moment below the base plate M'. Eq.(5.14) shows the relationship:

$$\begin{cases} Q = \left(m_i + m_{wall} + m_{roof}\right) \cdot S_e\left(T_{imp}\right) + m_c \cdot S_e\left(T_{conv}\right) \\ M = \left(m_i \cdot h_i + m_{wall} \cdot h_{wall} + m_{roof} \cdot h_{roof}\right) \cdot S_e\left(T_{imp}\right) + m_c \cdot h_c \cdot S_e\left(T_{conv}\right) \\ M' = \left(m_i \cdot h_i' + m_{wall} \cdot h_{wall} + m_{roof} \cdot h_{roof}\right) \cdot S_e\left(T_{imp}\right) + m_c \cdot h_c' \cdot S_e\left(T_{conv}\right) \end{cases} \quad (5.14)$$

Where m_i and m_c can be derived from Table 5.4 as fraction of the total liquid mass; m_{water} is the mass of the tank shell wall, m_{roof} is the mass of the roof. $S_e(T_{imp})$ is the impulsive spectral acceleration obtained from elastic spectrum corresponding to the ultimate limit state, for a damping of $\xi = 5\%$, and $S_e(T_{conv})$ is the convective spectral acceleration obtained with $\xi = 0.5\%$ on elastic spectrum. h_i, h_c, h_i', h_c' are derived from the Table 5.4, also in this case, as a fraction of the maximum height of the liquid content; h_{wall} and h_{roof} are the height of the barycentre of the tank shell wall and roof. In Eq.(5.14), the moment M is used to design the thickness of the wall tank, while M' to design the anchors.

5.2.2 Evaluation of seismic action with EN1998-4:2023

The structural analysis is performed for steel tanks assumed with linear elastic behaviour. The excitation of the ground shaking can be treated following a force-based approach and the dynamic effects of the impulsive and convective masses can be described by equivalent static pressure distributions applied on the tank shell wall and the bottom plate. The seismic design actions at the base of the tank are evaluated distinguishing the case of rigid and flexible tank. The definition of the stiffness of the tank is done following a tabular approach (in Appendix A of the Eurocode 8-4:2023) in which the tank is classified rigid or flexible considering the ratio of the maximum height of the liquid content and the radius and the ratio between the radius and the thickness of the wall tank. For the scope of the present study, all examined tanks are considered rigid. Thus, the relationships for rigid tanks are taken into account, in particular the seismic design reactions at the base of the tank due to the impulsive mass are given by Eq.(5.15):

$$\begin{cases} F_{b,ir,h} = C_{F,ir,h} \cdot \Gamma_{ir,h} \cdot m \cdot S_r\left(T_{ir,h}\right) \\ M_{W,ir,h} = C_{MW,ir,h} \cdot \Gamma_{ir,h} \cdot m \cdot H_{f,\max} \cdot S_r\left(T_{ir,h}\right) \\ M_{G,ir,h} = C_{M,ir,h} \cdot \Gamma_{ir,h} \cdot \pi \cdot R^4 \cdot \rho_f \cdot S_r\left(T_{ir,h}\right) \end{cases} \quad (5.15)$$

Where $F_{b,ir,h}$ is the maximum impulsive rigid base shear; $M_{W,ir,h}$ and $M_{G,ir,h}$ are the maximum rigid impulsive moment just above and below the base plate, respectively. The difference between two moment is that in $M_{G,ir,h}$ are added the pressures on the base plate. $C_{F,ir,h}$, $C_{Mw,ir,h}$ and $C_{M,ir,h}$ are coefficients reported in Table 5.5; $\Gamma_{ir,h}$ is the participation factor of the impulsive rigid pressure mode, in Table 5.5; m is the total liquid mass; $H_{f,max}$ is the maximum height of the filling level; R is the radius of the tank; ρ_f is the desinsity of the liquid content. $T_{ir,h}$ is the first natural period of the impulsive rigid tank, taken equal to zero if the interaction soil-structure is neglected; and $S_r\left(T_{ir,h}\right)$ is the ordinate of the design spectrum evaluated at life safety limit (*SLV*) with behaviour factor taken equal to 1 and a damping of $\xi = 2\%$ for steel structures.

At the same way, the contributions of the base shear and the overturning moment due to the convective masse are given by Eq.(5.16):

$$\begin{cases} F_{b,c} = C_{F,c} \cdot \Gamma_c \cdot m \cdot S_e\left(T_{conv}\right) \\ M_{w,c} = C_{MW,c} \cdot \Gamma_c \cdot m \cdot H_{f,\max} \cdot S_e\left(T_{conv}\right) \\ M_{G,c} = C_{M,c} \cdot \Gamma_c \cdot \pi \cdot R^4 \cdot \rho_f \cdot S_e\left(T_{conv}\right) \end{cases} \quad (5.16)$$

Where $F_{b,c}$ is the convective base shear, $M_{W,c}$ is the convective moment just above the base plate and $M_{G,c}$ is the convective moment at the base including the base pressure component arising from the first sloshing mode. $C_{F,c}$, $C_{MW,c}$, $C_{M,c}$ are coefficients, reported in Table 5.5; Γ_c is the participation factor of the convective pressure component given by Table 5.5. T_{conv} is the first natural period of convective mode evaluated as Eq.(5.17) and $S_e(T_{conv})$ is the spectral acceleration of horizontal elastic spectrum at *SLV* with a damping ratio of the liquid $\xi = 0.5\%$. If $T_{conv} > 4s$ the elastic pseudo-acceleration spectrum can be derived from the elastic displacement spectrum (as indicated in Eurocode 8-1 [80]).

$$T_{conv} = \frac{2 \cdot \pi \cdot \sqrt{\frac{R}{g}}}{\sqrt{1.841 \cdot \tanh\left(\frac{1.841 \cdot h_{f,\max}}{R}\right)}} \tag{5.17}$$

Where g is the gravity acceleration. Also in this case, the total base reactions are the sum of impulsive and convective contribution.

Table 5.5: Dimensionless parameters and participation factors for impulsive and convective masses [117]**.**

	$\frac{H_{f,max}}{R}$	$C_{F,ir,h}$	$C_{MW,ir,h}$	$C_{M,ir,h}$	$\Gamma_{ir,h}$	$C_{F,c}$	$C_{MW,c}$	$C_{M,c}$	Γ_c
Slender	2.0	0.7630	0.3224	1.5273	1.0	0.2355	0.1762	0.7170	1.9173
Interm.	1.0	0.5478	0.2214	0.3950	1.0	0.4493	0.2758	0.3523	1.6954
Squat	0.5	0.2988	0.1193	0.1132	1.0	0.6950	0.3752	0.2651	1.5609

5.2.3 Height of convective wave

Seismic design requires a safety distance between the maximum level of the liquid content and the upper part of the tank. This freeboard prevents the over-topping or the spillage of the liquid content when a convective wave is triggered by the seismic action. The absolute maximum value of the vertical wave height, d_{max}, is due to the convective mass of the first mode of vibration and can be evaluated as Eq.(5.18).

$$d_{\max} = 0.84 \cdot R \cdot \frac{S_e\left(T_{conv}\right)}{g} \tag{5.18}$$

Where $S_e(T_{conv})$ is the pseudo-spectral acceleration on elastic spectrum for a vibration period of T_{conv} and a damping ratio of $\xi = 0.5\%$.

5.2.4 Pseudo-acceleration spectrum

The elastic pseudo-acceleration spectrum is determined for the site of Milazzo (Sicily, Italy) of $longitude = 15.27°$ and $latitude = 38.2028°$, for a return period of the seismic action of $Tr = 475yr$, for three damping ratio 0.5%, 2% and 5%. The spectrum is obtained using the relationship inside *NTC2018* [41] and the seismic parameters for the site of interest are taken from the Appendix B of the same code [120]. Under these assumptions, Table 5.6 shows the useful parameters to build the spectrum from the Italian Standard.

Table 5.6: Parameters that define the seismic action [120]**.**

$a_g\ [g]$	F_0	T_C^*	Soil Category	S	$T_B\ [s]$	$T_C\ [s]$	$T_D\ [s]$
0.1607	2.5260	0.369	C	1.4565	0.1795	0.5384	2.2427

Where a_g is the peak ground acceleration on rock; F_0 is the maximum amplification factor of the spectrum; T_C^* reference value for the determination of the period in correspondence of the horizontal branch; S is a coefficient that takes into account of the soil category and topography conditions. T_B is the lower limit of the period of the constant spectral acceleration branch; T_C is the upper limit of the period of the constant spectral acceleration branch; and T_D is the value defining the beginning of the constant displacement response range of the spectrum. Figure 5.3 shows the pseudo-acceleration spectra for the three damping factors.

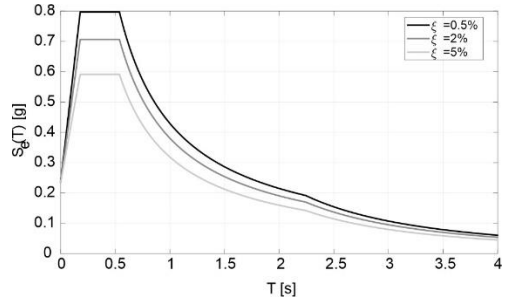

Figure 5.3: Elastic pseudo-acceleration spectra for the site of Milazzo (ME).

5.2.5 Results

Table 5.7 shows, for convenience, the geometrical properties of three examined tanks, anticipating the results of the design of the thickness shell wall that will be discussed in the next sections. The liquid inside the tanks has density $\rho_f = 0.81\, t/m^3$. For steel structures, the Young's elasticity modulus is $E = 210GPa$ and the density of the material is $7.85\ t/m^3$.

Table 5.7: Geometry of three archetype tanks.

	$H\ [m]$	$h_{f,max}\ [m]$	$R\ [m]$	$t_w\ [mm]$
Slender	11	10	5	20
Intermediate	13	12	12	25
Squat	15	14	28	30

The geometry allows to evaluate the terms of masses and the heights in Eq.(5.14) for approach of Eurocode 8-4:2006. The results are summarized in Table 5.8. The properties linked to the roof are neglected.

Table 5.8: Masses and heights of two degree of freedom system.

	m_{wall} $[t]$	m $[t]$	m_i $[t]$	m_c $[t]$	h_{wall} $[m]$	h_i $[m]$	h_c $[m]$	h_i' $[m]$	h_c' $[m]$
Slender	54	631	481	150	5.5	4.5	7.5	5	7.6
Intermediate	192	4379	2400	1979	6.5	5.0	7.4	8.6	9.4
Squat	621	27871	8361	19509	7.5	5.6	7.6	20.4	21.2

To the aim of qualitative comparisons, the evaluation of the pseudo-spectral acceleration for $T_{conv} > 4s$ is obtained, approximately, considering the relationship of *NTC18* of the last branch of the spectrum, going beyond the validity limit. Table 5.9 shows the values of shear and moments at the base of the tank, evaluated with Eq. (5.14).

Table 5.9: Evaluation of shear and moments at the base of the tank with Eurocode 8-4:2006.

	T_{imp} $[s]$	T_{conv} $[s]$	$S_e(T_{imp}, \xi = 5\%)$ $[g]$	$S_e(T_{conv}, \xi = 0.5\%)$ $[g]$	Q $[kN]$	M $[kN \cdot m]$	M' $[kN \cdot m]$
Slender	0.06	3.31	0.35	0.09	1996	9526	10416
Intermediate	0.10	5.27	0.44	0.03	11878	62537	101497
Squat	0.21	9.21	0.59	0.01	54262	315058	1064260

On the other hand, Table 5.10 and Table 5.11 briefly summarize the steps to obtain the shear and the moments at the base of the tank evaluated with Eurocode 8-4:2023.

Table 5.10: Evaluation of pseudo-spectral acceleration for impulsive and convective masses.

	$T_{ir,h}$ $[s]$	T_{conv} $[s]$	$S_r(T_{ir,h}, \xi = 2\%, q = 1)$ $[g]$	$S_e(T_{conv}, \xi = 0.5\%)$ $[g]$
Slender	0	3.31	0.23	0.09
Intermediate		5.25		0.03
Squat		9.18		0.01

Table 5.11: Evaluation of shear and moments at the base of the tank with Eurocode 8-4:2023.

	$F_{b,ir,h}$ $[kN]$	$F_{b,c}$ $[kN]$	$M_{W,ir,h}$ $[kN \cdot m]$	$M_{G,ir,h}$ $[kN \cdot m]$	$M_{W,c}$ $[kN \cdot m]$	$M_{G,c}$ $[kN \cdot m]$	Q $[kN]$	M $[kN \cdot m]$	M' $[kN \cdot m]$
Slender	1105	246	4671	5577	2024	1886	1351	6695	7463
Interm.	5507	1142	26709	47850	9111	10788	6649	35820	58639
Squat	19119	3387	106867	406483	27428	72506	22506	134295	478988

The differences between two versions of the Eurocodes show that the Eurocode 8-4:2023 version provides force at the base with values of about 40% less that the Eurocode 8-4:2006 version currently used.

Table 5.12 shows the maximum displacement of the convective wave. Considering the thickness of the floating roof, d_{max} values are increased all at 1 m, for sake of safety.

Table 5.12: Freeboard distance for three archetype tanks.

	$\boldsymbol{d_{max}}$ $[\boldsymbol{m}]$
Slender	0.37
Intermediate	0.35
Squat	0.37

5.3 Actions on the tanks and limit state verifications

The design of a tank should be developed taking into consideration characteristic values of the actions on the structure, applying partial safety factors to these characteristic values [66]. Here, the design is performed considering wind and seismic actions, evaluating the cases of empty and full tank. The actions should be combined to verify the tank under conditions of ultimate limit states (*ULS*) and serviceability limit states (*SLS*).

At *ULS*, the tank should be verified [66,68]:

-to ensure the global stability and static equilibrium.

-to control inelastic behaviour.

-to control buckling phenomena.

More in detail, for the overall stability, the tank should behave as a rigid body and should resist to sliding and overturning. Limited amount of displacement of the tank is tolerable by the pipe system to avoid the detachment or the loss of contents. The behaviour in plastic field is restricted to limited portions of the tank, and the ultimate deformations of the materials are not exceeded. Lastly, the nature and the extent of buckling phenomena in the shell should be controlled.

At *SLS*, deformations, deflections or vibrations should not cause damage to non-structural elements and should not adversely affect the effective use of the structure [66].

5.3.1 Load combinations.

The combinations of actions used for the design are contained inside Eurocode 0 [79]:

-fundamental combination (for *ULS*), for persistent or transient design situations:

$$\gamma_{G1} \cdot G_1 + \gamma_{Q_1} \cdot Q_{k_1} + \gamma_{Q_2} \cdot \psi_{02} \cdot Q_{k_2} \tag{5.19}$$

-combination of actions for seismic design situations:

$$E + G_1 + \psi_{21} \cdot Q_{k1} + \psi_{22} \cdot Q_{k2} \tag{5.20}$$

-quasi-permanent combination (for *SLS*):

$$G_1 + \psi_{21} \cdot Q_{k_1} + \psi_{22} \cdot Q_{k_2} \tag{5.21}$$

In which, G_1 is the self-weight of the tank; Q_{k_j} are the variable actions of different nature that can act contemporary and in this case are the wind action and hydrostatic pressure of the internal liquid. The subscript j can assume the value of 1 meaning the predominant action, while when $j = 2$ is the non-predominant action. E is the seismic action. ψ_{02}, ψ_{21}, ψ_{22} are combination coefficient and assume values as shown in Table 5.13. Also in this case, the second value of the subscript distinguishes the predominant from non-predominant action.

Table 5.13: Combination coefficient [79]

	wind	liquid content
ψ_{02}	0.6	1
ψ_{2j}	0	0.8

The values of ψ for hydrostatic pressure are taken for the [79] from the “Category E” corresponding to the industrial area. γ_{G_1} and γ_{Q_j} are partial safety factors, with values in Table 5.14, distinguishing the favourable and unfavourable cases.

Table 5.14: Partial safety factors [79]**.**

	Favourable	Unfavourable
γ_{G_1}	1	1.3
$\gamma_{Q_j,(wind)}$	0	1.5
$\gamma_{Q_j,(liquid)}$	0	1.35

The value of $\gamma_{Q_j,(liquid)}$ is taken from Eurocode 3-4-2 [66].

For the seismic combination, the combination of the effects of three components of the seismic action should be considered as described in Eurocode 8-1 [80]. More in detail, for the design, the vertical action is neglected and since the tank is axisymmetric, it is allowed to consider only one horizontal component [68]. Therefore, the Eq.(5.20) can be specified as Eq.(5.22):

$$E_x + 0.3 \cdot E_y + G_1 + \psi_{21} \cdot Q_{k_1} + \psi_{22} \cdot Q_{k_2} \tag{5.22}$$

Where E_x and E_y are the two horizontal components of seismic action.

Finally, the combinations for two limit states considered for the design are in total 10 and are shown, for sake of simplicity, in Table 5.15.

Table 5.15: Load combinations used for the design.

1) Quasi-permanent combination (*SLS*):	$G_1 + 0.8 \cdot Q_{k1(\text{liquid})}$
2)Fundamental combination (*ULS*):	$G_1 + 1.5 \cdot Q_{k1(\text{wind})}$
	$1.3 \cdot G_1 + 1.5 \cdot Q_{k1(\text{wind})}$
	$G_1 + 1.35 \cdot Q_{k1(\text{liquid})}$
	$1.3 \cdot G_1 + 1.35 \cdot Q_{k1(\text{liquid})}$
	$G_1 + 1.5 \cdot Q_{k1(\text{wind})} + 1.35 \cdot Q_{k_2(liquid)}$
	$1.3 \cdot G_1 + 1.5 \cdot Q_{k1(\text{wind})} + 1.35 \cdot Q_{k_2(liquid)}$
	$G_1 + 1.35 \cdot Q_{k_2(liquid)} + 1.5 \cdot 0.6 \cdot Q_{k1(\text{wind})}$
	$1.3 \cdot G_1 + 1.35 \cdot Q_{k_2(liquid)} + 1.5 \cdot 0.6 \cdot Q_{k1(\text{wind})}$
3)Seismic combination:	$E_x + 0.3 \cdot E_y + G_1 + 0.8 \cdot Q_{k_1(liquid)}$

5.3.2 Verifications

For steel tanks, the *ULS* verifications should be done to avoid the plastic collapse due to exceedance of the yield stress of the steel in the

shell wall; the inelastic buckling at the base of the shell wall for effect of seismic action [68]; but also, the elastic buckling of the shell wall due to excessive circumferential compression. In addition, anchoring systems should be designed to remain elastic in the seismic design situation. However, they should also provide with sufficient ductility, so as to avoid brittle failures [68].

For the verification, the resistances should be divided for partial safety factors. Table 5.16 shows the partial safety factors used for the resistance verifications.

Table 5.16: Partial factors for resistances [66]**.**

Resistance of shell wall to plastic limit state	γ_{M0}	1.0
Resistance of shell wall to stability	γ_{M1}	1.1
Resistance of bolted connection	γ_{M5}	1.25

To ensure the correct behaviour in operating conditions, a hydrostatic test is carried out, completely filling the tank of water to verify the tightness of the welds of the shell wall, and to avoid the loss of content. In this filling condition, the shell wall should be subjected in each its part to tensile radial stresses less than maximum allowable hydrostatic test stress, S_t, defined by API650 [77]. This verification is done with actions in *SLS* combination.

5.3.3 Buckling limit state

The buckling strength is evaluated as described in Eurocode 3-1-6 [67]. More specifically, the design buckling stresses can be obtained from Eq.(5.23):

$$\sigma_{x,Rd} = \frac{\alpha_x \cdot \sigma_{x,cr}}{\gamma_{M1}} \quad , \quad \sigma_{\theta,Rd} = \frac{\alpha_\theta \cdot \sigma_{\theta,cr}}{\gamma_{M1}} \tag{5.23}$$

Where $\sigma_{x,Rd}$ and $\sigma_{\theta,Rd}$ are the design values of meridional and circumferential stress, respectively; $\sigma_{x,cr}$ and $\sigma_{\theta,cr}$ are the critical

meridional and circumferential buckling stresses, respectively; and α_x and α_θ are the meridional and circumferential elastic imperfection reduction factors, respectively. The buckling strength can be evaluated as Eq.(5.23) only if the relative shell slenderness of the tank, $\bar{\lambda}$, is greater than the plastic limit relative slenderness, $\bar{\lambda}_p$, in fact, in this case, the shell wall has a behaviour entirely elastic. The value of relative shell slenderness can be determined as Eq.(5.24):

$$\bar{\lambda}_x = \sqrt{\frac{f_{yk}}{\sigma_{x,cr}}} \quad , \quad \bar{\lambda}_\theta = \sqrt{\frac{f_{yk}}{\sigma_{\theta,cr}}} \tag{5.24}$$

While the value of the plastic limit relative slenderness is defined from Eq.(5.25):

$$\bar{\lambda}_{p,x} = \sqrt{\frac{\alpha_x}{1-\beta}} \quad , \quad \bar{\lambda}_{p,\theta} = \sqrt{\frac{\alpha_\theta}{1-\beta}} \tag{5.25}$$

Where β is the plastic range factor equal to 0.6.

The meridional elastic imperfection reduction factor α_x can be evaluated as Eq.(5.26):

$$\alpha_x = \frac{0.62}{1+1.91\cdot\left(\frac{\Delta w_k}{t_w}\right)^{1.44}} \tag{5.26}$$

Where t_w is the thickness of the shell wall and Δw_k is the characteristic imperfection amplitude given by Eq.(5.27):

$$\Delta w_k = \frac{1}{Q}\cdot\sqrt{\frac{R}{t_w}}\cdot t_w \tag{5.27}$$

Where R is the radius of the tank and Q is the fabrication quality parameter, taken equal to 25, assuming a high-quality class.

The circumferential elastic imperfection reduction factor, α_θ is taken equal to 0.65, because is specified for a heigh fabrication quality class.

The critical stresses depend on the dimensionless length parameter, ω, defined as Eq.(5.28):

$$\omega = \frac{H}{\sqrt{R \cdot t_w}} \tag{5.28}$$

The meridional critical buckling stress σ_x can be evaluated by Eq.(5.29):

$$\sigma_{x,cr} = 0.605 \cdot E_s \cdot C_x \cdot \frac{t_w}{R} \tag{5.29}$$

Where E_s is the elastic modulus of the steel; C_x is a coefficient depending on the dimensionless length parameter, and is defined by Eq.(5.30):

$$\begin{cases} C_x = 1.0 & 1.7 \le \omega \le 0.5 \cdot \dfrac{R}{t_w} \\ C_x = 1.36 - \dfrac{1.83}{\omega} + \dfrac{2.07}{\omega^2} & \omega \le 1.7 \\ C_x = \max\left(1 + \dfrac{0.2}{C_{xb}} \cdot \left[1 - 2 \cdot \omega \cdot \dfrac{t_w}{R}\right]; 0.60\right) & \omega > 0.5 \cdot \dfrac{R}{t_w} \end{cases} \tag{5.30}$$

Where C_{xb} is a parameter depending on the boundary conditions, equal to 3 for anchored tanks with roof.

The critical circumferential buckling stress can be evaluated, by Eq.(5.31):

$$\begin{cases} \sigma_{\theta,cr} = 0.92 \cdot E_s \cdot \left(\dfrac{C_\theta}{\omega}\right) \cdot \left(\dfrac{t_w}{R}\right) & 20 \le \dfrac{\omega}{C_\theta} \le 1.63 \cdot \dfrac{R}{t_w} \\ \sigma_{\theta,cr} = 0.92 \cdot E_s \cdot \left(\dfrac{C_{\theta s}}{\omega}\right) \cdot \left(\dfrac{t_w}{R}\right) & \dfrac{\omega}{C_\theta} < 20 \\ \sigma_{\theta,cr} = E_s \cdot \left(\dfrac{t_w}{R}\right)^2 \cdot \left[0.275 + 2.03 \cdot \left(\dfrac{C_\theta}{\omega} \cdot \dfrac{R}{t_w}\right)\right] & \dfrac{\omega}{C_\theta} > 1.63 \cdot \dfrac{R}{t_w} \end{cases} \tag{5.31}$$

Where C_θ is a coefficient that depends on the boundary condition and is equal to 1.25 for anchored tank with roof; and $C_{\theta s}$ is external pressure

buckling factor for short cylinders equal to $1.25 + \frac{8}{\omega^2} - \frac{4}{\omega^3}$ for anchored tanks with roof.

5.4 Design of minimum shell wall and base plate thicknesses

This section discusses about the choices for the evaluation of the minimum thicknesses of the shell wall and base plate. The minimums are the starting point for the structural analyses that will confirm the validity of the thicknesses under the gravity and seismic loads. If the checks will not verify, the thicknesses should be increased. The design of the minimum thicknesses follows the indications of the American Standards Petroleum Institute (API650) [77], that are a useful guide, recognized worldwide. The American standards are based on the allowable stresses approach and many relationships inside the code are calibrated on experimental evidence. For this reason, in addition to these prescriptions, the Eurocode 3-4-2 [66] is adopted for evaluations about the capacity design that the American Standard does not take into consideration. The approach used by the Eurocode is performance-based approach, oriented to satisfy the basic design requirements of different limit states though structural analysis. The design of the minimum thicknesses is demanded to other standards that have as example the American standards. For this reason, the choice to use API650 [77] as reference standard for minimum thicknesses.

5.4.1 Base plate

The base plate should have a corroded thickness not less than $6\,mm$. The base plate should be extended for at least $50\,mm$ over the external weld at the base of the wall.

5.4.2 Shell design

The shell thickness should be taken as the greater between the thickness obtained from minimum standards, including an addition thickness for the resistance to the corrosion (uncorroded design shell thickness), and the thickness derived from hydrostatic test. Typically, the tanks are designed considering the condition of full filling level. Hydrostatic test consists in filling the tank of water for 24 hours and it is ensured that there are not leaks due to discontinuities from the welds, o pinholes.

Typically, the shell of the tank is divided in plates, called courses, with a thickness that decrease with the height. The API650 defines the nominal minimum thickness at varying of the diameter, in particular, for tanks with diameter less than $36\,m$, the shell thickness at the lowest course cannot be less than $6\,mm$, while for diameter between $36\,m$ and $60\,m$ the minimum nominal diameter is $8\,mm$. Each plate should be a width greater than $1800\,mm$. The American standard provides that for tanks with diameter less than $61\,m$ the thickness along the height can be constant, otherwise a variation with the height can be evaluated with a method called in the standard variable-design-point. In addition to these methods, under specific assumptions, a linear elastic analysis can be performed to verify that the circumferential stresses along the shell do not exceed the allowable stresses defined inside the standard. The tanks examined in this thesis have diameter less than $61\,m$, thus can be designed considering constant the thickness along the height. The calculation of the thickness is done following the 1-foot method proposed inside the standard. This method evaluates the shell thickness at $30\,cm$ above the bottom of each shell course. The required minimum thickness of shell plates, $t_{w,min}$, shall be the greater between the design shell thickness, t_d, and the hydrostatic test shell thickness, t_t. These thicknesses are given by Eq.(5.32):

$$\begin{cases} t_d = \dfrac{4.9 \cdot D \cdot \left(H_{f,\max} - 0.3\right) \cdot G}{S_d} + CA \\ t_t = \dfrac{4.9 \cdot D \cdot \left(H_{f,\max} - 0.3\right)}{S_t} \end{cases} \tag{5.32}$$

that are dimensional relationships. More specifically, t_d and t_t are expressed in $[mm]$; D is the diameter of the tank in $[m]$; $H_{f,max}$ maximum height of the internal liquid in $[m]$; $G = \rho_f / \rho_w$ is the design specific gravity of the liquid to be stored; where ρ_w is the water density; CA is the corrosion allowance, in $[mm]$; S_d is the allowable stress in design condition, in $[MPa]$; and S_t is the allowable stress for hydrostatic test condition, in $[MPa]$. S_d and S_t are defined as Eq.(5.33).

$$\begin{cases} S_d = \min\left(\frac{2}{3}\cdot f_y ; \frac{2}{5}\cdot f_t\right) \\ S_t = \min\left(\frac{3}{4}\cdot f_y ; \frac{3}{7}\cdot f_t\right) \end{cases} \quad (5.33)$$

Where f_y is the yield strength and f_t is the tensile strength of the steel.

5.4.3 Annular bottom plate

Typically, the bottom base plate could be equipped with a base ring, called annular plate, to reinforce the part of the plate under the shell wall and to satisfy strength requirements. A performance target provided by Eurocode 3-4-2 [66] is the formation of a plastic hinge in the annular bottom plate, avoiding alternating plasticity in the weld detail at the bottom of the shell wall. This requirement can be reached designing the thickness of the annular plate less than the thickness of the lowest course of the shell wall. The formation of the plastic hinge on the base plate allows the development of the membranal behaviour. However, the reduced thickness could lead to uplift of the outer edge of the annular plate, activating potential corrosion phenomena.

The thickness of the annular plate, t_a, can be evaluated using the values of Table 5.17. This table can be applied for tanks with $H_{f,max} \cdot G \leq 23m$. Beyond this height an elastic analysis should be made to determine the annular plate thickness.

Table 5.17: Annular bottom plate thickness [77]**.**

Plate thickness of first shell course [mm]	Stress in the first shell course [MPa]			
	≤ 190	≤ 210	≤ 220	≤ 250
$t_w \leq 19$	6	6	7	9
$19 < t_w \leq 25$	6	7	10	11
$25 < t_w \leq 32$	6	9	12	14

$32 < t_w \leq 40$	8	11	14	17
$40 < t_w \leq 45$	9	13	16	19

The use of this table can be summarized in the following steps. First column should be considered for two times, evaluated both considering design shell thickness and thickness for hydrostatic test design. For each wall thickness, the maximum stress in the first shell course is evaluated following Eq.(5.34) for two design cases:

$$\begin{cases} \text{Design stress} = \left(\dfrac{t_d - CA}{t_w} \right) \cdot S_d \\ \text{Hydrostatic test stress} = \left(\dfrac{t_t}{t_w} \right) \cdot S_t \end{cases} \tag{5.34}$$

The thickness of the annular plate is the greater between the thicknesses of the two design conditions, read from the table.

The width of the annular plate should be the greater between $600\ mm$ and a minimum width, L_a, defined by Eq.(5.35). L_a is measured from inside edge of the shell to the edge of the plate in the remainder of the bottom, in $[mm]$.

$$L_a = 2 \cdot t_a \cdot \sqrt{\frac{f_y}{2 \cdot \Upsilon \cdot G \cdot H_{f,\max}}} \tag{5.35}$$

In which, t_a in expressed in $[mm]$; f_y in $[MPa]$; $H_{f,max}$ in $[m]$; $\Upsilon = 9.81/1000$ is the density factor of the water in $[MPa/m]$.

According to Eurocode 3-4-2 [66], the minimum annular plate thickness for diameter greater than $12.5\ m$ should be taken as Eq.(5.36).

$$t_a = \max\left(\frac{t_w}{3} + 3mm; 6mm \right) \tag{5.36}$$

with t_w the thickness of the first shell course.

5.4.4 Design of anchor bolts

The strength and the stiffness of the anchors are designed following the Eurocode 3-1-8 [69]. According to this standard, the anchors that are required to act in shear should not have a nominal yield strength, f_{yb} greater than $640\ Mpa$. The distribution of anchors along the diameter of the base plate of the tank is determined following a requirement inside the API650[77] that provides that the anchor centre-to-centre spacing measured along the tank circumference at the shell outer diameter shall not exceed $3\ m$.

The design tension strength of the anchor bolts is the smaller of the design tension resistance of the anchor and the design bond resistance of the concrete on the anchor bolt Eurocode 2-1-1 [121]. But, when the anchor bolts are provided with a washer plate, the contribution of bond concrete-steel is negligible, because the tension force is transferred though the load distributing device. The tension strength of the individual anchor is given by Eq.(5.37):

$$F_{t,Rd} = \frac{0.9 \cdot f_{ub} \cdot A_s}{\gamma_{M2}} \tag{5.37}$$

Where f_{ub} is the ultimate tensile strength of the anchor; A_s is tensile stress area; γ_{M2} is a partial safety factor equal to 1.25. The shear strength of an anchor bolt $F_{vb,Rd}$, instead, is given by Eq.(5.38):

$$F_{vb,Rd} = \frac{0.6 \cdot f_{ub} \cdot A_s}{\gamma_{M2}} \tag{5.38}$$

Regarding to the stiffness, the axial stiffness of the anchors is evaluated as Eq.(5.39):

$$k_N = \frac{E_s \cdot A_s}{L_b} \tag{5.39}$$

Where E_s is the elastic modulus of the steel; L_b is the anchor bolt elongation length, taken equal to the sum of 8 times the diameter of the anchor, the grout layer, the plate thickness, the washer, and half of the height of the nut.

The EC3-1-8 does not provide anything information on the shear stiffness of the anchors. For this reason, a simplified approach is used to evaluate the shear stiffness, in particular the anchor is considered fixed at the bottom in the zone of embedded in the concrete foundation and free to translate but not to rotate at the top. This scheme simulates the behaviour of the anchors inside a bearing plate with chairs as shown in Figure 5.4. With this configuration, the anchor is subjected to deflection due to bending and shear. The total deflection (Δ_l) of the individual anchor to lateral loading (P) is expressed as the sum of the contribution due to bending and the shear and is given by Eq.(5.40) [122]:

$$\Delta_l = \frac{P \cdot h^3}{12 \cdot E_s \cdot I} + \frac{10 \cdot P \cdot h}{9 \cdot G \cdot A_s} \tag{5.40}$$

Where h is the stand-off distance that for simplicity is assumed equal to L_b; I is the anchor second moment of inertia; G is the shear modulus of the anchor.

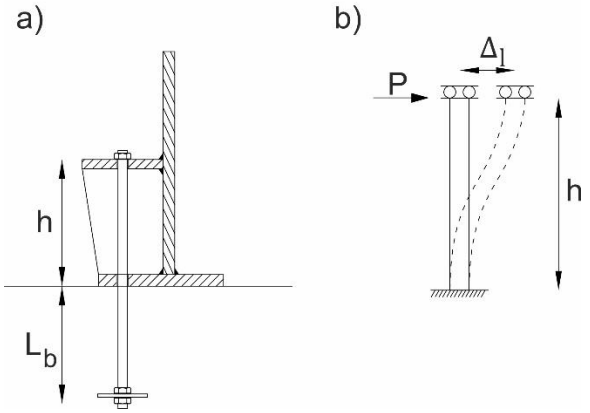

Figure 5.4:a) Anchorage system. b) Structural scheme.

The relative shear stiffness is obtained from the ratio between P/Δ_l and is given by Eq.(5.41):

$$k_V = \left(\frac{h^3}{12 \cdot E_s \cdot I} + \frac{10 \cdot h}{9 \cdot G \cdot A_s} \right)^{-1} \tag{5.41}$$

5.5 Static nonlinear elastic analysis with finite element model

5.5.1 Description of finite element model

Nonlinear models are generated with SAP2000 v.23.0.0 [81] software. Three archetypes of tanks with different aspect ratio are modelled using four-node shell elements. Each model consists in two parts, a shell wall and a base plate. Contact properties are assigned among springs under the base plate, in particular, the tank rests on a bed of springs reacting only on in compression with a coefficient of subgrade reaction of $50\ N/cm^3$, while at the boundary of the base plate, springs, uniformly distributed along the circumference, react only on in tension to simulate the behaviour of the anchor bolts. In this way, the uplift is allowed. The external lateral forces, instead, are absorbed from the anchorage system though the shear resistance. On the other hand, the friction resistance between base plate and foundation mat is not considered in the finite element model (*FEM*) but the consideration of possible failure mechanisms involving bolt shear was relegated to the post-processing of analysis results. The roof is modelled with a rigid diaphragm at the top of the tank at the maximum filling level. The structural analysis is performed considering material nonlinearities in the anchors implementing elastic-plastic hardening constitutive laws, while the shell wall and the base plate are considered with a behaviour infinitely elastic. In addition, also geometric nonlinearities of the deforming tank are considered through analysis with large displacements.

The quadrangular elements of the mesh have a different ratio height-base. Figure 5.5 shows the example of the mesh used for the shell wall, in panel a), and the base and annular plate, in panel b), of the intermediate tank. The elements have a length of the arc of $0.42\ m$, subtending an angle of 2°, with a height that varies with the height of the tank, for the shell wall, and the radius, for the base plate. The shell wall has a mesh denser close to the base plate for the first $0.5\ m$ with a ratio height-base of 0.3 than at the top with a ratio of 1.19, while from $0.5\ m$ to $2\ m$ the ratio is 0.60. The base plate, instead, has a fined mesh under the

shell wall, in particular, the annular plate is more discretized than the centre of the plate.

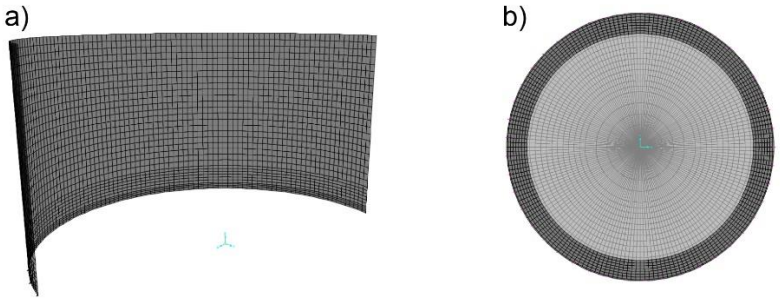

Figure 5.5: a) Mesh of shell wall. b) Mesh of annular and base plate.

The anchor bolts are modelled as in Figure 5.6, with two springs in series, where the lowest one has the function to react only in tension, opening its when is subject to compression; the other spring, instead, has properties in tension and in shear. In figure, tension and shear laws of the anchors are shown. In more detail, elastic-plastic hardening law is implemented in tension, in which, the yielding force is equal to $F_y = A_s \cdot f_{yb}$; the yielding displacement is $z_y = F_y/k_N$; the ultimate force is $F_T = A_s \cdot f_{ub}$; and the ultimate displacement is assumed equal to $z_u = 10 \cdot \delta_y$, with a plastic stiffness of $k_p = \left(F_T - F_y\right)/\left(z_u - z_y\right)$. On the other hand, the shear behaviour is assumed infinitely elastic with shear stiffness given by Eq.(5.41).

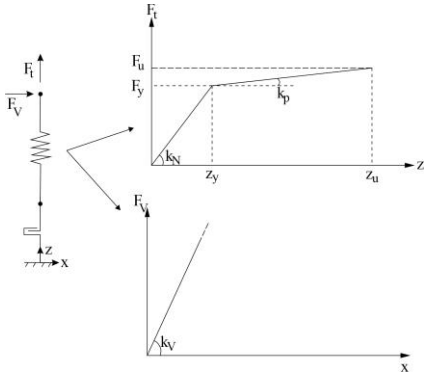

Figure 5.6: Springs in series that simulate the behaviour of the anchor bolt.

5.5.2 Static nonlinear elastic analysis

For the design of the tanks, the static nonlinear elastic analyses are carried out considering all load combinations of Table 5.15. The aim of these analyses is to design the thicknesses of the shell wall and the base plate, and diameter and number of anchor bolts. The structural analysis is iterative because, initially, is carried out with minimum thicknesses from Section 5.4, then, if at least one of the verifications is not satisfied, the analysis is repeated increasing the thicknesses or the diameter or the number of the anchors. The nonlinear analysis is performed following steps. Firstly, self-weight of the tank is applied increasing the contact pressure between the foundation mat and the base plate; then, in case of full tank, the self-weight and the hydrostatic pressure of the internal liquid is applied to the tank shell wall. Lastly, gradually external actions are applied at the tank. The wind action is applied so as described in Section 5.1 and this one could trigger buckling effects on the shell wall. Seismic action, instead, is modelled considering equivalent static forces of shear and the bending moment at the base, applied on the centre of the base plate, to verify the shear and tension resistance of the anchors. The demand parameters from the structural analysis should be compared with the relative design resistances.

5.5.3 Results

Tanks considered for the analysis, are built with steel grade *S355*, with minimum yield strength of $355\,MPa$, a specific weight of $76.97\ kN/m^3$. The liquid contained inside all tanks is assumed a flammable substance of specific weight of $7.94\ kN/m^3$. The anchor bolts have a strength class of *8.8* with $f_{yb} = 640\ MPa$ and $f_{ub} = 800\ MPa$.

Table 5.18 shows the final configuration of the designed tanks. Each tank has a uniform thickness of the shell wall, t_w, along all the height; the base plate, instead, is stiffened with an annular plate under the shell wall, with a thickness of value, t_{ap}, with a width defined from value of L_{ap}. In addition, the base plate has a thickness less than the annular plate, of value t_{bp}. In the last three rows, the configuration of the anchors is shown, and for each tank, the number of anchors, the diameter d_B and the spacing between anchors, i_B, are defined.

Table 5.18: Geometrical properties of the three archetype tanks.

Geometry		Slender	Intermediate	Squat
R	[m]	5	12	27.5
H	[m]	10	13	16
t_w	[mm]	20	25	30
t_{ap}	[mm]	10	20	25
t_{bp}	[mm]	8	15	20
L_{ap}	[m]	1	1.8	2
No. bolts		12	45	120
d_B		M27	M30	M39
i_B	[m]	2.62	1.68	1.44

Table 5.19 shows the design capacity parameters for three tanks.

Table 5.19: Capacity parameters.

	Slender	Intermediate	Squat
$\sigma_{\theta,Rd}\ [MPa]$	18.05	12.66	9.01
$\sigma_{x,Rd}\ [MPa]$	144.12	57.84	22.21
$F_{T,Rd}\ [kN]$	330.05	407.23	688.32
$F_{V,Rd}\ [kN]$	220.03	271.49	458.88

An example of results from the nonlinear elastic analysis is depicted in Figure 5.7, where the forces per unit of thickness acting on the mid-surface of the shell element are shown for a portion of the shell wall. Panel a) shows the shell element forces in circumferential direction, F_{11} and panel b) in meridional direction, F_{22}. These forces divided by the thickness of the shell wall are the circumferential and meridional stresses, respectively. The figure refers to the load combination: $1.3 \cdot G_1 + 1.5 \cdot Q_{k1(wind)} + 1.35 \cdot Q_{k2(liquid)}$. The maximum value of compressive

circumferential force is $F_{11} = -92.18\ kN/m$ that in terms of circumferential stress becomes $\sigma_{\theta,Ed} = -3.73\ MPa$. This value is less than the corresponding capacity parameters, therefore, the verification of the shell buckling is satisfied. At the same way, the maximum compression value of the meridional force is $F_{22} = -134.74$ that corresponds to $\sigma_{x,Ed} = -5.39\ MPa$, less than the $\sigma_{x,Rd}$. Thus, the verification of the elephant foot buckling is satisfied.

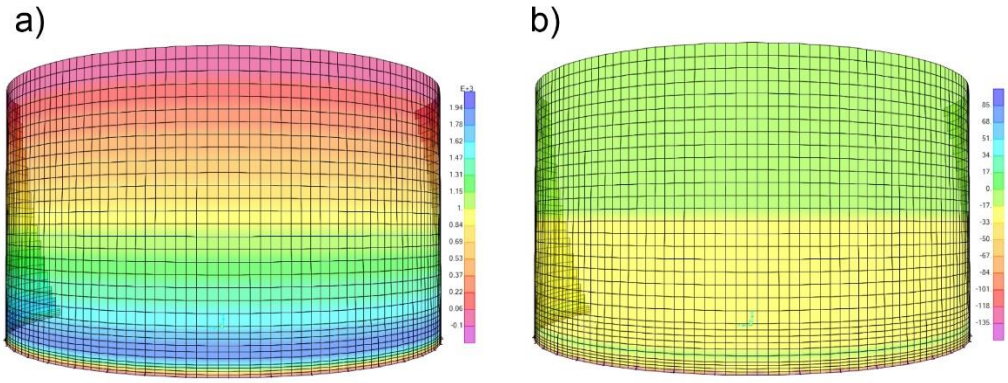

Figure 5.7: Shell element forces in a) circumferential direction and in b) meridional direction, for the load combination $1.3 \cdot G_1 + 1.5 \cdot Q_{k1(wind)} + 1.35 \cdot Q_{k2(liquid)}$.

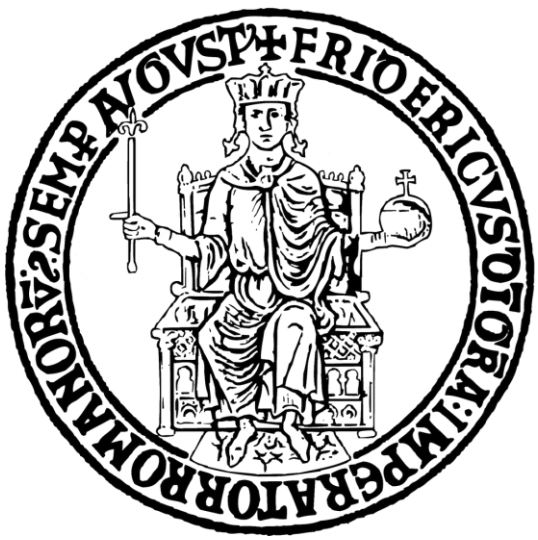
AVGVST FRIDERICVS DEI GRA IMPERATOR ROMANORVM SEMP

Bibliography

1. Goda, K.; De Risi, R. Future Perspectives of Earthquake-Tsunami Catastrophe Modelling: From Single-Hazards to Cascading and Compounding Multi-Hazards. *Front Built Environ* **2023**, *8*, doi:10.3389/fbuil.2022.1022736.

2. De Risi, R.; Goda, K. Probabilistic Earthquake–Tsunami Multi-Hazard Analysis: Application to the Tohoku Region, Japan. *Front Built Environ* **2016**, *2*, doi:10.3389/fbuil.2016.00025.

3. Maeda, T.; Furumura, T.; Noguchi, S.; Takemura, S.; Sakai, S.; Shinohara, M.; Iwai, K.; Lee, S.J. Seismic- and Tsunami-Wave Propagation of the 2011 Off the Pacific Coast of Tohoku Earthquake as Inferred from the Tsunami-Coupled Finite-Difference Simulation. *Bulletin of the Seismological Society of America* **2013**, *103*, 1456–1472, doi:10.1785/0120120118.

4. Kappes, M.; Keiler, M.; Glade, T. From Single- to Multi-Hazard Risk Analyses: A Concept Addressing Emerging Challenges. In Proceedings of the Proceedings of the international conference; CERG Editions, Ed.; Strasbourg, 2010; pp. 351–356.

5. Kappes, M.S.; Keiler, M.; von Elverfeldt, K.; Glade, T. Challenges of Analyzing Multi-Hazard Risk: A Review. *Natural Hazards* 2012, *64*, 1925–1958.

6. Kappes, M.S.; Papathoma-Köhle, M.; Keiler, M. Assessing Physical Vulnerability for Multi-Hazards Using an Indicator-Based Methodology. *Applied Geography* **2012**, *32*, 577–590, doi:10.1016/j.apgeog.2011.07.002.

7. Delmonaco, G.; Margottini, C.; Spizzichino, D. *New Methodology for Multi-Risk Assessment and the Harmonisation of Different Natural Risk Maps*; 2006;

8. Tarvainen, T.; Jarva, J.; Greiving, S. Spatial Pattern of Hazards and Hazard Interactions in Europe. **2006**, 83–91.

9. Hewitt, K.; Burton, I. *Hazardousness of a Place: A Regional Ecology of Damaging Events.*; University of Toronto Press: Toronto and Buffalo, 1971; ISBN 0-8020-3281-8.

10. Lorito, S.; Selva, J.; Basili, R.; Romano, F.; Tiberti, M.M.; Piatanesi, A. Probabilistic Hazard for Seismically Induced Tsunamis: Accuracy and Feasibility of Inundation Maps. *Geophys J Int* **2015**, *200*, 574–588, doi:10.1093/gji/ggu408.

11. Grezio, A.; Babeyko, A.; Baptista, M.A.; Behrens, J.; Costa, A.; Davies, G.; Geist, E.L.; Glimsdal, S.; González, F.I.; Griffin, J.; et al. Probabilistic Tsunami Hazard Analysis: Multiple Sources and Global Applications. *Reviews of Geophysics* 2017, *55*, 1158–1198.

12. NOAA National Geophysical Data Center / World Data. NCEI/WDS Global Historical Tsunami Database Available online: https://data.noaa.gov/metaview/page?xml=NOAA/NESDIS/NGDC/MGG/Hazards/iso/xml/G02151.xml&view=getDataView (accessed on 4 July 2023).

13. Cito, P.; Chioccarelli, E.; Iervolino, I. Conditional Hazard for Simplified Multi-Site Seismic Hazard and Risk Analyses. *Earthq Eng Struct Dyn* **2023**, *52*, 482–499, doi:10.1002/eqe.3769.

14. Iervolino, I.; Giorgio, M.; Galasso, C.; Manfredi, G. Conditional Hazard Maps for Secondary Intensity Measures. *Bulletin of the Seismological Society of America* **2010**, *100*, 3312–3319, doi:10.1785/0120090383.

15. Cornell, C.A. Engineering Seismic Risk Analysis. *Bulletin of the Seismological Society of America* **1968**, *58*, 1583–1606.

16. Geist, E.; Parsons, T. Probabilistic Analysis of Tsunami Hazards. *Natural Hazards* **2006**, *37*, 277–314, doi:10.1007/s11069-005-4646-z.

17. Sørensen, M.B.; Spada, M.; Babeyko, A.; Wiemer, S.; Grünthal, G. Probabilistic Tsunami Hazard in the Mediterranean Sea. *J Geophys Res Solid Earth* **2012**, *117*, doi:10.1029/2010JB008169.

18. Ward, S.N. Tsunamis. In *The Encyclopedia of Physical Science and Technology*; Meyers, R.A., Ed.; Academic Press Inc: Tarzana, California, U.S.A., 2002; Vol. 17, pp. 175–191.

19. Selva, J.; Tonini, R.; Molinari, I.; Tiberti, M.M.; Romano, F.; Grezio, A.; Melini, D.; Piatanesi, A.; Basili, R.; Lorito, S. Quantification of Source Uncertainties in Seismic Probabilistic Tsunami Hazard Analysis (SPTHA). *Geophys J Int* **2016**, *205*, 1780–1803, doi:10.1093/gji/ggw107.

20. Volpe, M.; Lorito, S.; Selva, J.; Tonini, R.; Romano, F.; Brizuela, B. From Regional to Local SPTHA: Efficient Computation of Probabilistic Tsunami Inundation Maps Addressing near-Field Sources. *Natural Hazards and Earth System Sciences* **2019**, *19*, 455–469, doi:10.5194/nhess-19-455-2019.

21. Asch, K. Geology without National Boundaries - The 1 : 5 Million International Geological Map of Europe and Adjacent Areas. *Episodes* **2006**, *29*, 39–42.

22. Laske, G.; Masters, G.; Ma, Z.; Pasyanos, M. Update on CRUST1.0 - A 1-Degree Global Model of Earth's Crust. In Proceedings of the EGU General Assembly Conference Abstracts; April 2013; pp. EGU2013-2658.

23. Molinari, I.; Morelli, A. EPcrust: A Reference Crustal Model for the European Plate. *Geophys J Int* **2011**, *185*, 352–364, doi:10.1111/j.1365-246X.2011.04940.x.

24. Grünthal, G.; Arvidsson, R.; Bosse, C. *Earthquake Model for the European-Mediterranean Region for the Purpose of GEM1*; 2010;

25. Grünthal, G.; Wahlström, R. The European-Mediterranean Earthquake Catalogue (EMEC) for the Last Millennium. *J Seismol* **2012**, *16*, 535–570, doi:10.1007/s10950-012-9302-y.

26. Basili, R.; Tiberti, M.M.; Kastelic, V.; Romano, F.; Piatanesi, A.; Selva, J.; Lorito, S. Integrating Geologic Fault Data into Tsunami Hazard Studies. *Natural Hazards and Earth System Science* **2013**, *13*, 1025–1050, doi:10.5194/nhess-13-1025-2013.

27. Basili, R.; Kastelic, V.; Demircioglu, M.B.; Garcia Moreno, D.; Nemser, E.S.; Petricca, P.; Sboras, S.P.; Besana-Ostman, G.M.; Cabral, J.; Camelbeeck, T.; et al. European Database of Seismogenic Faults (EDSF) [Data Set] Available online: https://doi.org/10.6092/INGV.IT-SHARE-EDSF (accessed on 8 September 2023).

28. Wells, D.L.; Coppersmith, K.J. *New Empirical Relationships among Magnitude, Rupture Length, Rupture Width, Rupture Area, and Surface Displacement*; 1994; Vol. 84;.

29. Petersen, M.D.; Frankel, A.D.; Harmsen, S.C.; Mueller, C.S.; Haller, K.M.; Wheeler, R.L.; Wesson, R.L.; Zeng, Y.; Boyd, O.S.; Perkins, D.M.; et al. *Documentation for the 2008 Update of the United States National Seismic Hazard Maps*; 2008;

30. Baker, J.; Bradley, B.; Stafford, P. *Seismic Hazard and Risk Analysis*; Cambridge University Press: Cambridge, 2021; ISBN 9781108425056.

31. Strasser, F.O.; Arango, M.C.; Bommer, J.J. Scaling of the Source Dimensions of Interface and Intraslab Subduction-Zone Earthquakes with Moment Magnitude. *Seismological Research Letters* **2010**, *81*, 941–950, doi:10.1785/gssrl.81.6.941.

32. Thingbaijam, K.K.S.; Mai, P.M.; Goda, K. New Empirical Earthquake Source-Scaling Laws. *Bulletin of the Seismological Society of America* **2017**, *107*, 2225–2246, doi:10.1785/0120170017.

33. Goda, K.; Yasuda, T.; Mori, N.; Maruyama, T. New Scaling Relationships of Earthquake Source Parameters for Stochastic Tsunami Simulation. *Coastal Engineering Journal* **2016**, *58*, doi:10.1142/S0578563416500108.

34. Abrahamson, N.; Eeri, M.; Gregor, N.; Addo, K. *BC Hydro Ground Motion Prediction Equations For Subduction Earthquakes*; 2016;

35. Beauval, C.; Cotton, F.; Theodoulidis, N.; Delavaud, E.; Rodriguez, L.; Scherbaum, F.; Haendel, A. Regional Differences in Subduction Ground Motions. **2012**.

36. Cornell, C.A. *Engineering Seismic Risk Analysis*; 1968; Vol. 58;.

37. Baker, J. *Probabilistic Seismic Hazard Analysis*; 2013;

38. Field, E.; Jordan, T.; Cornell, C. OpenSHA: A Developing Community-Modeling Environment for Seismic Hazard Analysis. *Seismological Research Letters* **2003**, *74*, 406–419, doi:10.1785/gssrl.74.4.406.

39. Akkar, S.; Bommer, J. Empirical Equations for the Prediction of PGA, PGV, and Spectral Accelerations in Europe, the Mediterranean Region, and the Middle East. *Seismological Research Letters - SEISMOL RES LETT* **2010**, *81*, 195–206, doi:10.1785/gssrl.81.2.195.

40. Bindi, D.; Pacor, F.; Luzi, L.; Puglia, R.; Massa, M.; Ameri, G.; Paolucci, R. Ground Motion Prediction Equations Derived from the Italian Strong Motion Database. *Bulletin of Earthquake Engineering* **2011**, *9*, 1899–1920, doi:10.1007/s10518-011-9313-z.

41. CS.LL.PP. Decreto Ministeriale: Norme Tecniche per Le Costruzioni. Gazzetta Ufficiale Della Repubblica Italiana, n.42, 20 Febbraio, Suppl. Ordinario n.8 Ist. Polig. e Zecca Dello Stato S.p.a., Rome (in Italian). **2018**.

42. Montaldo, V.; Faccioli, E.; Zonno, G.; Akinci, A.; Malagnini, L. Treatment of Ground-Motion Predictive Relationships for the Reference Seismic Hazard Map of Italy. *J Seismol* **2005**, *9*, 295–316, doi:10.1007/s10950-005-5966-x.

43. Chioccarelli, E.; Cito, P.; Iervolino, I.; Giorgio, M. REASSESS V2.0: Software for Single- and Multi-Site Probabilistic Seismic Hazard Analysis. *Bulletin of Earthquake Engineering* **2019**, *17*, 1769–1793, doi:10.1007/s10518-018-00531-x.

44. Pagani, M.; Monelli, D.; Weatherill, G.; Danciu, L.; Crowley, H.; Silva, V.; Henshaw, P.; Butler, L.; Nastasi, M.; Panzeri, L.; et al. Openquake Engine: An Open Hazard (and Risk) Software for the Global Earthquake Model. *Seismological Research Letters* **2014**, *85*, 692–702, doi:10.1785/0220130087.

45. Molinari, I.; Tonini, R.; Lorito, S.; Piatanesi, A.; Romano, F.; Melini, D.; Hoechner, A.; Vida, J.M.G.; Maciás, J.; Castro, M.J.; et al. Fast

Evaluation of Tsunami Scenarios: Uncertainty Assessment for a Mediterranean Sea Database. *Natural Hazards and Earth System Sciences* **2016**, *16*, 2593–2602, doi:10.5194/nhess-16-2593-2016.

46. ASCE7 *Minimum Design Loads and Associated Criteria for Buildings and Other Structures*; American Society of Civil Engineers (ASCE), 2017; ISBN 9780784479964.

47. Antonioni, G.; Spadoni, G.; Cozzani, V. A Methodology for the Quantitative Risk Assessment of Major Accidents Triggered by Seismic Events. *J Hazard Mater* **2007**, *147*, 48–59, doi:10.1016/j.jhazmat.2006.12.043.

48. Campedel, M. *Analysis of Major Industrial Accidents Triggered by Natural Events Reported in the Principal Available Chemical Accident Databases*; Bologna, 2008;

49. Krausmann, E.; Renni, E.; Campedel, M.; Cozzani, V. Industrial Accidents Triggered by Earthquakes, Floods and Lightning: Lessons Learned from a Database Analysis. *NATURAL HAZARDS* **2011**, *59*, 285–300, doi:10.1007/s11069-011-9754-3.

50. Cozzani, V.; Gubinelli, G.; Antonioni, G.; Spadoni, G.; Zanelli, S. The Assessment of Risk Caused by Domino Effect in Quantitative Area Risk Analysis. *J Hazard Mater* **2005**, *127*, 14–30, doi:https://doi.org/10.1016/j.jhazmat.2005.07.003.

51. Cozzani, V.; Campedel, M.; Renni, E.; Krausmann, E. Industrial Accidents Triggered by Flood Events: Analysis of Past Accidents. *J Hazard Mater* **2010**, *175*, 501–509, doi:https://doi.org/10.1016/j.jhazmat.2009.10.033.

52. Krausman, E. *Analysis of Natech Risk Reduction in EU Member States Using a Questionnaire Survey*; Publications Office, 2010;

53. Landucci, G.; Antonioni, G.; Tugnoli, A.; Cozzani, V. Release of Hazardous Substances in Flood Events: Damage Model for Atmospheric Storage Tanks. *Reliab Eng Syst Saf* **2012**, *106*, 200–216, doi:https://doi.org/10.1016/j.ress.2012.05.010.

54. Salzano, E.; Iervolino, I.; Fabbrocino, G. Seismic Risk of Atmospheric Storage Tanks in the Framework of Quantitative Risk

Analysis. *J Loss Prev Process Ind* **2003**, *16*, 403–409, doi:https://doi.org/10.1016/S0950-4230(03)00052-4.

55. Iervolino, I.; Fabbrocino, G.; Manfredi, G. Fragility of Standard Insutrial Structures by a Response Surface Based Method. *Journal of Earthquake Engineering* **2004**, *12*, 927–945, doi:10.1080/13632460409350515.

56. Basco, A.; Salzano, E. The Vulnerability of Industrial Equipment to Tsunami. *J Loss Prev Process Ind* **2016**, *50*, doi:10.1016/j.jlp.2016.11.009.

57. Bakalis, K.; Fragiadakis, M.; Vamvatsikos, D. Surrogate Modeling for the Seismic Performance Assessment of Liquid Storage Tanks. *Journal of Structural Engineering* **2017**, *143*, 04016199.1-04016199.13, doi:10.1061/(ASCE)ST.1943-541X.0001667.

58. Bakalis, K.; Vamvatsikos, D.; Fragiadakis, M. Seismic Risk Assessment of Liquid Storage Tanks via a Nonlinear Surrogate Model. *Earthq Eng Struct Dyn* **2017**, *46*, doi:10.1002/eqe.2939.

59. Petrone, C.; Rossetto, T.; Goda, K. Fragility Assessment of a RC Structure under Tsunami Actions via Nonlinear Static and Dynamic Analyses. *Eng Struct* **2017**, *136*, 36–53, doi:10.1016/j.engstruct.2017.01.013.

60. Baiguera, M.; Rossetto, T.; Robertson, I.; Petrone, C. A Procedure for Performing Nonlinear Pushover Analysis for Tsunami Loading to ASCE 7. *Journal of Structural Engineering* **2022**, *148*, 04021270, doi:10.1061/(ASCE)ST.1943-541X.0003256.

61. Baiguera, M.; Rossetto, T.; Robertson, I.; Petrone, C. A Nonlinear Static Procedure for the Tsunami Design of a Reinforced Concrete Building to the ASCE7 Standard. In Proceedings of the SECED 2019 Conference; Rossetto, T., Ed.; Society fro Earthquake and Civil Engineering Dynamics: London, September 10 2019.

62. Foster, A.S.J.; Rossetto, T.; Allsop, W. An Experimentally Validated Approach for Evaluating Tsunami Inundation Forces on Rectangular Buildings. *Coastal Engineering* **2017**, *128*, 44–57, doi:https://doi.org/10.1016/j.coastaleng.2017.07.006.

63. Macabuag, J.; Rossetto, T.; Lloyd, T. Sensitivity Analyses of a Framed Structure Under Several Tsunami Design-Guidance Loading Regimes. In Proceedings of the 2nd ECEES Conference; European Association for Earthquake Engineering: Instanbul, Turkey, 2014.

64. Attary, N.; Unnikrishnan, V.U.; van de Lindt, J.W.; Cox, D.T.; Barbosa, A.R. Performance-Based Tsunami Engineering Methodology for Risk Assessment of Structures. *Eng Struct* **2017**, *141*, 676–686, doi:https://doi.org/10.1016/j.engstruct.2017.03.071.

65. FEMA *Federal Emergency Management Agency, Guidelines for Designof Structures for Vertical Evacuationfrom Tsunami*; 2008;

66. UNI EN 1993-4-2 Eurocode 3, Design of Steel Structures - Parte 4-2: Tanks, UNI EN 1993-4-2:2017. **2017**.

67. UNI EN 1993-1-6 Eurocode 3, Design of Steel Structures - Parte 1-6: Strength and Stability of Shell Structures, UNI EN 1993-1-6:2017. **2017**.

68. UNI EN 1998-4 Eurocode 8 - Design of Structures for Earthquake Resistance - Part 4: Silos, Tanks and Pipelines. **2006**.

69. UNI EN 1993-1-8 Eurocode 3 - Design of Steel Structures - Part 1-8: Design of Joints. **2005**.

70. Araki, S.; Kunimatsu, W.; Nishiyama, S.; Furuse, T.; Aoki, S. ichi; Kotake, Y. Experimental Study on Tsunami Wave Load Acting on Storage Tank in Coastal Area. *J Loss Prev Process Ind* **2017**, *50*, 347–354, doi:10.1016/j.jlp.2016.10.004.

71. Timoshenko, S.P.; Gere, J.M. *Theory of Elastic Stability*; McGraw-Hill, Ed.; Secondo Edition.; New York, 1961;

72. Bakalis, K.; Karamanos, S.A. Uplift Mechanics of Unanchored Liquid Storage Tanks Subjected to Lateral Earthquake Loading. *Thin-Walled Structures* **2021**, *158*, doi:10.1016/j.tws.2020.107145.

73. Eligehausen, Rolf.; Mallée, Rainer.; Silva, J.F. Anchorage in Concrete Construction. **2006**.

74. Zeitler, R.; Wörner, J.-D. Tragverhalten von Dübelverankerungen in Hochfestem Beton. *Beton- und Stahlbetonbau* **1995**, *90*, 241–244, doi:10.1002/BEST.199500390.

75. Fuchs, W.; Eligehausen, R. *Tragverhalten Und Bemessung von Befestigungen Ohne Randeinfluß Unter Querzugbelastung (Load-Bearing Behaviour and Design of Fixing without Edge Influence under Shear Loading)*; German, 1986;

76. UNI EN 1991-1-4 Eurocode 1 - EN 1991-1-4-2004 - General Actions - Wind Actions. **2004**.

77. API 650 *American Petroleum Institue, Welded Tanks for Oil Storage*; 2018;

78. Calvi, G.M.; Nascimbene, R. Progettazione Sismica Dei Serbatoi. *Progettare i gusci* **2011**, 537–672.

79. UNI EN 1990 Eurocode 0: Basis of Structural Design. **2006**.

80. UNI EN 1998-1 Eurocode 8 - Design of Structures for Earthquake Resistence - Part 1: General Rules, Seismic Actions and Rules for Buildings. **2013**.

81. Computers and Structures Inc. SAP2000 Integrated Software for Structural Analysis and Design 2021.

82. Malhotra, P.K.; Veletsos, A.S. Uplifting Analysis of Base Plates in Cylindrical Tanks. *Journal of Structural Engineering* **1994**, *120*, 3489–3505.

83. Malhotra, P.K.; Veletsos, A.S. Beam Model for Base-Uplifting Analysis of Cylindrical Tanks. *Journal of Structural Engineering* **1994**, *120*, 3471–3488, doi:10.1061/(asce)0733-9445(1994)120:12(3471).

84. Mia, M.M.; Kameshwar, S. Fragility Assessment of Bottom Plates in above Ground Storage Tanks during Flood Events. *J Loss Prev Process Ind* **2023**, 104975, doi:10.1016/j.jlp.2023.104975.

85. Billington, D.P. Analysis of Shell Walls. In *Thin shell concrete structures*; McGraw-Hill, Ed.; United State of America, 1965; pp. 89–110.

86. Rehm, G.; Eligehausen, R.; Mallée, R. Befestigungstechnik (Fixing Technology). In *Betonkalender*; 1988; Vol. Part II, pp. 569–663.

87. Iervolino, I.; Fabbrocino, G.; Manfredi, G. *Fragility of Standard Industrial Structures by a Response Surface Based Method*; 2004; Vol. 12;.

88. Bakalis, K. Incorporating Modeling Uncertainties in the Collapse Assessment of Capacity-Designed Steel Moment Frames under Seismic Loading. *Journal of Structural Engineering* **2024**, *150*, doi:10.1061/jsendh.steng-12969.

89. Lees, F.; Lees, F.P. *Lees' Loss Prevention in the Process Industries : Hazard Identification, Assessment and Control*; Elsevier Science & Technology: Burlington, UNITED STATES, 2005; ISBN 9780080489339.

90. Lees, F. *Lees' Loss Prevention in the Process Industries : Hazard Identification, Assessment and Control*; Elsevier Science & Technology: San Diego, UNITED STATES, 2012; ISBN 9780123977823.

91. Center for Chemical Process Safety (CCPS) Chemical Process Quantitative Risk Analysis. In *Guidelines for Chemical Process Quantitative Risk Analysis*; 2010; pp. 1–55 ISBN 9780470935422.

92. Cozzani, V.; Antonioni, G.; Landucci, G.; Tugnoli, A.; Bonvicini, S.; Spadoni, G. Quantitative Assessment of Domino and NaTech Scenarios in Complex Industrial Areas. *J Loss Prev Process Ind* **2014**, *28*, 10–22, doi:10.1016/j.jlp.2013.07.009.

93. Antonioni, G.; Landucci, G.; Necci, A.; Gheorghiu, D.; Cozzani, V. Quantitative Assessment of Risk Due to NaTech Scenarios Caused by Floods. *Reliab Eng Syst Saf* **2015**, *142*, 334–345, doi:10.1016/j.ress.2015.05.020.

94. Fabbrocino, G.; Iervolino, I.; Orlando, F.; Salzano, E. Quantitative Risk Analysis of Oil Storage Facilities in Seismic Areas. *J Hazard Mater* **2005**, *123*, 61–69, doi:10.1016/j.jhazmat.2005.04.015.

95. Iervolino, I. Analisi Quantitativa Di Rischio Sismico Nell' Industria Di Processo, University of Naples Federico II: Naples, 2003.

96. Gallina, V.; Torresan, S.; Critto, A.; Sperotto, A.; Glade, T.; Marcomini, A. A Review of Multi-Risk Methodologies for Natural Hazards: Consequences and Challenges for a Climate Change Impact Assessment. *J Environ Manage* **2016**, *168*, 123–132, doi:https://doi.org/10.1016/j.jenvman.2015.11.011.

97. Schmidt, J.; Matcham, I.; Reese, S.; King, A.; Bell, R.; Henderson, R.; Smart, G.; Cousins, J.; Smith, W.; Heron, D. Quantitative Multi-Risk Analysis for Natural Hazards: A Framework for Multi-Risk Modelling. *Natural Hazards* **2011**, *58*, 1169–1192, doi:10.1007/s11069-011-9721-z.

98. Liu, Z.; Nadim, F.; Garcia-Aristizabal, A.; Mignan, A.; Fleming, K.; Luna, B.Q. A Three-Level Framework for Multi-Risk Assessment. *Georisk: Assessment and Management of Risk for Engineered Systems and Geohazards* **2015**, *9*, 59–74, doi:10.1080/17499518.2015.1041989.

99. Marzocchi, W.; Garcia-Aristizabal, A.; Gasparini, P.; Mastellone, M.L.; Di Ruocco, A. Basic Principles of Multi-Risk Assessment: A Case Study in Italy. *Natural Hazards* **2012**, *62*, 551–573, doi:10.1007/s11069-012-0092-x.

100. Ming, X.; Xu, W.; Li, Y.; Du, J.; Liu, B.; Shi, P. Quantitative Multi-Hazard Risk Assessment with Vulnerability Surface and Hazard Joint Return Period. *Stochastic Environmental Research and Risk Assessment* **2015**, *29*, 35–44, doi:10.1007/s00477-014-0935-y.

101. Selva, J. Long-Term Multi-Risk Assessment: Statistical Treatment of Interaction among Risks. *Natural Hazards* **2013**, *67*, 701–722, doi:10.1007/s11069-013-0599-9.

102. Goda, K.; De Risi, R. Multi-Hazard Loss Estimation for Shaking and Tsunami Using Stochastic Rupture Sources. *International Journal of Disaster Risk Reduction* **2018**, *28*, 539–554, doi:https://doi.org/10.1016/j.ijdrr.2018.01.002.

103. Attary, N.; Van De Lindt, J.W.; Barbosa, A.R.; Cox, D.T.; Unnikrishnan, V.U. Performance-Based Tsunami Engineering for Risk Assessment of Structures Subjected to Multi-Hazards:

Tsunami Following Earthquake. *Journal of Earthquake Engineering* **2021**, *25*, 2065–2084, doi:10.1080/13632469.2019.1616335.

104. Goda, K.; Rossetto, T.; Mori, N.; Tesfamariam, S. Editorial: Mega Quakes: Cascading Earthquake Hazards and Compounding Risks. *Front Built Environ* **2018**, *4*, doi:10.3389/fbuil.2018.00008.

105. Goda, K.; Mori, N.; Yasuda, T. Rapid Tsunami Loss Estimation Using Regional Inundation Hazard Metrics Derived from Stochastic Tsunami Simulation. *International Journal of Disaster Risk Reduction* **2019**, *40*, 101152, doi:https://doi.org/10.1016/j.ijdrr.2019.101152.

106. Goda, K.; De Risi, R. Probabilistic Tsunami Loss Estimation Methodology: Stochastic Earthquake Scenario Approach. *Earthquake Spectra* **2017**, *33*, 1301–1323, doi:10.1193/012617EQS019M.

107. Goda, K.; De Risi, R.; De Luca, F.; Muhammad, A.; Yasuda, T.; Mori, N. Multi-Hazard Earthquake-Tsunami Loss Estimation of Kuroshio Town, Kochi Prefecture, Japan Considering the Nankai-Tonankai Megathrust Rupture Scenarios. *International Journal of Disaster Risk Reduction* **2021**, *54*, 102050, doi:https://doi.org/10.1016/j.ijdrr.2021.102050.

108. European Marine Observation and Data Network (EMODnet) Available online: https://emodnet.ec.europa.eu/en/bathymetry (accessed on 27 August 2023).

109. Satake, K.; Kanamori, H. Abnormal Tsunamis Caused by the June 13, 1984, Torishima, Japan, Earthquake. *J Geophys Res* **1991**, *96*, 19933–19939, doi:10.1029/91jb01903.

110. Haroun, M.A. *Dynamic Analyses of Liquid Storage Tanks*; Pasadena, California, 1980;

111. Araki, S.; Kunimatsu, W.; Nishiyama, S.; Furuse, T.; Aoki, S. ichi; Kotake, Y. Experimental Study on Tsunami Wave Load Acting on Storage Tank in Coastal Area. *J Loss Prev Process Ind* **2017**, *50*, 347–354, doi:10.1016/j.jlp.2016.10.004.

112. Malhotra, P. Practical Nonlinear Seismic Analysis of Tanks. *Earthquake Spectra* **2000**, *16*, 473–492, doi:10.1193/1.1586122.

113. Cooper, T.W.; Daley, W.M.; Bachula, G.R.; Hebner, R.E. *A Study of the Performance of Petroleum Storage Tanks during Earthquakes, 1933-1995*; 1997;

114. Luco, N.; Cornell, A.; Eeri, M. Structure-Specific Scalar Intensity Measures for Near-Source and Ordinary Earthquake Ground Motions. *Earthquake Spectra* **2001**.

115. Erto, P. *Probabilità e Statistica per Le Scienze e l'ingegneria*; Third edition.; McGraw-Hill: Milan, 2008;

116. Consiglio Nazionale delle Ricerche *CNR-DT 207 R1/2018 Istruzioni per La Valutazione Delle Azioni e Degli Effetti Del Vento Sulle Costruzioni*;

117. UNI EN 1998-4 Eurocode 8 - Design of Structures for Earthquake Resistance - Part 4: Silos, Tanks and Pipelines. **2023**.

118. Malhotra, P.K. Sloshing Loads in Liquid-Storage Tanks with Insufficient Freeboard. *Earthquake Spectra* **2005**, *21*, 1185–1192, doi:10.1193/1.2085188.

119. Ibrahim, R.A. *Liquid Sloshing Dynamics. Theory and Applications*; Cambridge University Press, 2005;

120. CS.LL.PP. *Allegato B Alle Norme Tecniche per Le Costruzioni: Tabelle Dei Parametri Che Definiscono l'azione Sismica*; 2018;

121. UNI EN 1992-1-1 Eurocode 2: Design of Concrete Structures-Part 1-1: General Rules and Rules for Buildings. **2004**.

122. Hosch, I.E. *Evaluation of Anchor Bolt Clearance Discrepancies*; 2016;

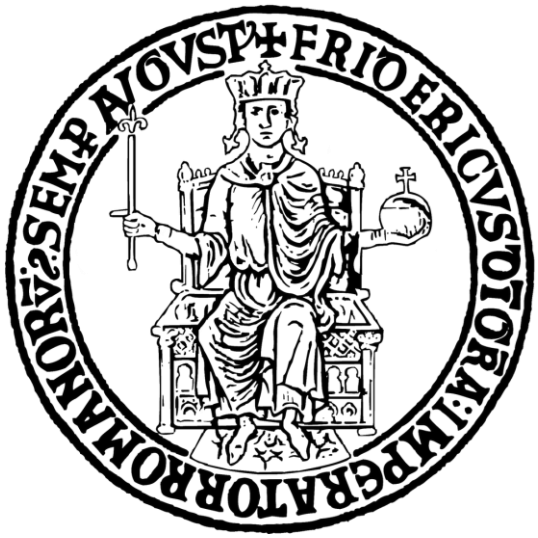
FRIDERICVS DEI GRA IMPERATOR ROMANORVM SEMPER AVGVST

Author’s publications

Vitale A., Baltzopoulos G., Iervolino I. *Earthquake and Tsunami multi-hazard NaTech risk assessment for petrochemical storage facilities. 18th World Conference on Earthquake Engineering (accepted).*

Cito P., Vitale A., Iervolino I. *Territorial exceedance of probabilistic seismic hazard from ShakeMap data*. Scientific Report 14, 4840 **(28 Feb 2024)**. https://doi.org/10.1038/s41598-024-55415-9

Iervolino I., Baltzopoulos G., Vitale A., Grella A., Bonini G., Iannaccone A., *Empirical distributions of traffic loads from one year of weigh-in-motion data*. Scientific Data 10, 289 **(18 May 2023)**. https://doi.org/10.1038/s41597-023-02212-0

Baltzopoulos G, Baraschino R, Chioccarelli E, Cito P, Vitale A, Iervolino I. *Near-source ground motion in the M7.8 Gaziantep (Turkey) earthquake*. Earthquake Engineering Structural Dynamic 1, 10 **(26 May 2023)**. https://doi.org/10.1002/eqe.3939

Cito P., Vitale A., Iervolino I. *Exceedance of design seismic actions during the 2016-2017 central Italy seismic sequence: sensitivity to two seismi hazard models*. Procedia Structural Integrity. XIX ANIDIS Conference, Seismic Engineering in Italy, 44, 3-10 **(9 Feb 2023)**. https://doi.org/10.1016/j.prostr.2023.01.002

Iervolino, I., Vitale, A., Cito, P. *Empirical assessment of seismic design hazard’s exceedance area*. *Scientific Reports* **11**, 18803 **(22 Sep 2021)**. https://doi.org/10.1038/s41598-021-98388-9

Iervolino I., Cito P., Felicetta C., Lanzano G., Vitale A. *Exceedance of design actions in epicentral areas: insights from the ShakeMap envelopes for the 2016-2017 central Italy sequence*. Bulletin of Earthquake Engineering 19, 5391-5414 **(3 Aug 2021)**. https://doi.org/10.1007/s10518-021-01192-z

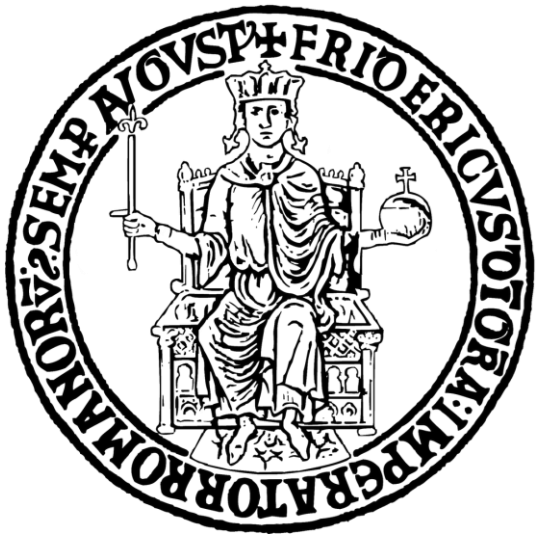
AVGVST FRIDERICVS DEI GRA IMPERATOR ROMANORVM SEMP